Local Unfolding of Helical Portal Region of Human Intestinal Fatty Acid Binding Protein Allows Ligand Entry for Binding

XIAO TIANSHU

(B.Sc., SJTU)

A THESIS SUBMITTED

FOR THE DEGREE OF DOCTOR OF PHILOSOPHY

DEPARTMENT OF BIOLOGICAL SCIENCES

NATIONAL UNIVERSITY OF SINGAPORE

2016

DECLARATION

I hereby declare that this thesis is my original work and it has been written by me in its entirety. I have duly acknowledged all the sources of information which have been used in the thesis.

This thesis has also not been submitted for any degree in any university previously.

_____

Xiao Tianshu

Date:

Acknowledgements

I would like to extend my gratitude to my supervisor, Professor Dr. Yang Daiwen, for his continuing guidance in five years. He helped me to solve many tough problems in this project, giving me a lot of brilliant advice. He is the person who introduces me to protein NMR and biophysics.

I would also like to thank Associate Professor Dr. Henry Mok Yu-Keung for the advice on my project for these years, which made me look at the project from different views. I would like to extend my thanks to Associate Professor Dr. Ganesh Srinivasan Anand. As my TAC member, his advice helps me inspect my project more carefully.

My sincere thanks would also go to Dr. Fan for his generous help in NMR experiments. I would like to thank Assistant Professor Dr. Lin Qingsong for providing stopped-flow fluorescence spectrometer. I would also like to thank Mr. Zhou Hu for his help in stopped-flow experiments.

Equally, I would like to thank Dr. Lin Zhi, Dr. Zhang Jingfeng, Dr. Lim Jack Wee, Dr. Wang Shujing, Dr. Gao Zhengwei, Dr. Hu Wentao and Dr. Liu Xiao for their advice on experiments and data analysis. I also want to thank all the members in Structure Biology Lab for their help and accompany.

I would also like to extent my thanks for NUS research scholarship, which provided me with the opportunity to study in DBS and the financial support.

Finally, I would like to extend my sincere gratitude to my families and friends for the unconditioned support and encouragement.

Table of Content

Summary

Fatty acid binding protein (FABP) is responsible for lipid transportation, carrying long chain fatty acids to their target sites. This process is essential for diverse biological activities, such as lipid metabolism, membrane constitution, transcription regulation and immune responses. As a carrier for lipids, FABP is capable of binding a range of lipids at a high affinity. There have been diverse structure and dynamics studies on the process of lipid entry, and 'helical portal' hypothesis was proposed mainly based on the comparisons between structures and dynamics of apo- and holo-FABP. However, this process remains puzzling. In this project, we conducted kinetics, structure and dynamics studies on a human intestinal FABP (hiFABP) variant K27C/D74C to clarify the mechanism underlying the process of ligand entry. For this mutant, the intra-molecule disulfide bond slowed down the ligand entry to a range reachable for NMR dynamics analysis. NMR relaxation dispersion analysis combined with stopped-flow fluorescence spectroscopy unveiled that the second helix of hiFABP undergoes a local unfolding process at a rate of ~10^4 s^{-1}, which 'opens' the helical portal region and allows ligand entry.

Besides the investigations on the helical portal region, other two mutants were generated and studied in a similar way. These studies further confirmed the conclusion mentioned above. Additionally, the results provided some clues for the relationship between the helical portal region and another two hot spots on FABP, the back portal and the gap between β strands D and E.

List of Figures

List of Tables

List of Abbreviations

3D	three dimension
4D	four dimension
ANS	1-anilinonaphthalene-8-sulfonic acid
CPMG	Car-Purcell-Meiboom-Gill
CRABP I	cellular retinoic acid binding protein I
CV	colume volume
dASA	difference in accessible surface area
DLS	dynamic light scattering
DTT	dithiothreitol
ESR	electron spin resonance
FABP	fatty acid binding protein
FPLC	fast protein liquid chromatography
hiFABP	human intestinal fatty acid binding protein
HSQC	heteronuclear single quantum coherence
iBABP	ileal bile acid binding protein
iLBP	intracellular lipid binding protein
ITC	isothermal titration calorimetry
k	rate constant
K_d	dissociation constant
MD	molecule dynamics
M_{XY}	magnetization in X-Y plane
M_Z	magnetization in Z axis
NMR	nuclear magnetic resonance
NOE	nuclear overhauser effect

NOESY	nuclear overhauser effect spectroscopy
NTA	nitrilotriacetic acid
PCR	polymerase chain reaction
PDB	protein data bank
PPAR	peroxisome proliferator-activated receptor
RMSD	root mean square deviation
SDS-PAGE	sodium dodecyl sulfate polyacrylamide gel electrophoresis
T1	longitude relaxation time
T2	transverse relaxation time
TOCSY	total correlation spectroscopy
DSS	4,4-dimethyl-4-silapentane-1-sulfonic acid
TMS	Tetramethylsilane

Local Unfolding of Helical Portal Region of Human Intestinal Fatty Acid Binding Protein Allows Ligand Entry for Binding

Abstract

Fatty acid binding protein (FABP) plays a significant role in lipid metabolism. These cellular proteins can incorporate fatty acids with high affinity, and transfer them to target sites. Although the structures of ligand-bound and ligand-free forms of FABP were determined by NMR and X-ray crystallography two decades ago, the mechanism of lipid binding is still unclear. In this study, we characterized the process of ligand association, protein dynamics, structure and ligand binding kinetics using three intestinal FABP variants. Mutations at different regions of the protein (the helical portal and the gap D-E) resulted in different impacts on the process of oleic acid association. The most important conclusion about the mechanism underlying oleic acid entry and exit is that local unfolding of the second α helix enables oleic acid entry, which is the rate-limiting step of oleic acid binding. In addition, it is found that the helical portal region is related to the gap D-E and the back portal, which have been reported to be involved in the processes of ligand delivery, internal water exchange and protein folding. It deserves further efforts to clarify how these events can be compatible and interconnected to each other.

Chapter 1. Introduction

1.1. Function of lipid and FABPs

Lipid metabolism is an important biological process. Many different biological processes involve fatty acids, such as signaling pathway, energy supply, cell membranes synthesis, cell apoptosis and metabolic response (1) (2). The insolubility of long chain fatty acids necessitates chaperones to assist intracellular and extracellular transportation. The intracellular lipid binding protein (iLBP) family serves as an assistant for lipid transportation. Members of this protein family are capable of binding long chain fatty acids, bile acids and retinoic acids and transport them to respective target sites.

FABP family is a subfamily of iLBP. FABP family contains different types of FABPs, specifically expressed in respective organs. They adopt similar structures despite of their different protein sequences. The organ where a specific FABP is expressed is closely related to the capability of the fatty acid metabolism (1). It has been suggested that the difference in the interactions of FABPs with fatty acids could be accounted by several specific residues of FABP and their intracellular environment.

Due to the crucial role of FABP in lipid transportation, this protein family is indispensable in metabolism regulation, immune responses and other biological activities (1, 3-5). Long chain fatty acids can bind and activate all the subclasses of PPAR, regulating the transcription of proteins that are important in metabolism (6, 7). It has been found that adipocyte FABP can transport long chain fatty acids to their target sites, peroxisome proliferator-activated receptors (PPARs) (1, 4, 8). Recent genetic studies and animal experiments have demonstrated the central role of fatty acid binding protein (FABP) in the pathways mediated by lipids and inflammatory responses (1).

The interactions between FABPs and various cytokines are critical for the inflammatory processes (4).

1.2. Intestinal fatty acid binding protein (iFABP)

Human intestinal fatty acid binding protein (hiFABP) is a member of fatty acid binding protein (FABP) family (3). It is expressed in the epithelium of small intestine (1). Previous studies have reported the crucial role of iFABP in lipid metabolism. The iFABP-deficient mice showed increased plasma insulin level for both gender (1, 9). The male iFABP deficient mice exhibited larger liver, higher level of triglyceride and heavier body weight, while for the female mice, the deficiency of iFABP resulted in decreased body weight, smaller liver and unaffected level of triglyceride (1, 9). This observation pointed out the special role of iFABP in metabolism regulation, which seems to be intrinsically related to gender. Later studies reported the relation between iFABP and insulin resistance, which should be correlated with the naturally occurred amino acid substitution in codon 54 of iFABP (9, 10). The substitution of Ala with Thr increases the affinity with fatty acids significantly, correlated with the high incidence of insulin resistance and type2 diabetes in Pima Indians (9). These observations highlighted the importance of iFABP in metabolism and suggested that iFABP might be a potential target of drug design for metabolic diseases.

Human iFABP has been studied for a long time in terms of structure and dynamics. The structure of hiFABP was first determined in 1990s by X-ray crystallography and NMR. (11). The hiFABP retains the general structure of iLBP, consisting of 10 β strands and 2 α helices to form a barrel structure with a helical lid on top, capable of binding fatty acids with a dissociation constant

(K_D) of ~0.2 μM (12). The helices cover the binding cavity, making the binding site inaccessible to the ligand, which necessitates an open form of hiFABP to enable ligand entry before binding. However, the mechanism how the ligand enters and exits remains obscure up to now. NMR dynamics, MD simulations and mutagenesis studies have suggested several possible ligand entry routes, including the gap region between β D-E, the back portal at the N terminal, and the helical portal region (13-19). Later studies further highlighted the potential of the helical portal region to be the entrance for ligand (20). The two strands D and E consist of most the hydrophobic residues, thus the gap between these two strands are full of hydrophobic side chains, which was proposed to be the hydrophobic core for protein folding (19, 21). It was reported that the internal water should be released through the gap D-E, which was thus proposed to be another possible portal for ligand (19). Besides the gap, the back portal, consisting of the turn F-G, H-I and the N terminus, has also been proposed to be a possible site for the release of the internal water (15, 17, 19). MD simulations suggested that the back portal might be the entrance for ligand (13, 15).

1.3. Helical portal region and ligand entry

The 'helical portal' hypothesis was proposed in 1989 by Sacchettini *et al.* - the oleic acid enters the binding pocket through the helical portal region comprised of the second α helix, turn E-F and turn C-D (Figure 1.1A) (11). Mutagenesis studies have pointed out the importance of the two helices in the process of ligand incorporation. Deletion of the two helices of intestinal FABP altered the ligand binding model from a two-step to a one-step reaction (12). The deletion in rabbit ileal bile acid binding protein (iBABP) also resulted in

the similar change in the model of ligand binding (22). These observations have suggested that the helical portal region was the most possible entry site of ligand.

X-ray crystal structures and more recent NMR studies have shown that the portal region has nearly identical structure no matter in the absence or presence of ligands (23). It is difficult to tell whether and how ligand enters through the helical portal region. By comparing the NMR dynamics of apo- and holo-iFABPs, the helical portal region was found to experience a regional conformational exchange which was not observed in the other residues of apo-iFABP (20). Thus this portal was proposed to be the entrance for ligand, and the conformational exchange in this region should be relevant to ligand binding (20, 24). The study of the cellular retinoic acid binding protein I (CRABP I), in which residues A35 and T57 were mutated to cysteines, again supported the possibility of the helical portal region to be the ligand entrance (25). This disulfide bond inhibited the release of the ligand from the protein but had little impact on the ligand association (25). A recent study on human liver FABP has demonstrated the violation between the millisecond dynamics of the protein and the rate limit of ligand entry, estimating that the process of the entrance opening should occur at a microsecond to sub-microsecond timescale (26). Despite of the intensive efforts, the mechanism underlying ligand binding to FABP is still unclear.

To verify whether the helical portal region is the entrance for ligand and address the question how the ligand enters and exits, the double point mutant K27C/D74C of hiFABP was utilized here for structure, dynamics, and kinetics analyses, which successfully formed intra-molecule disulfide bond. The

impact of this disulfide bond on ligand binding and protein dynamics would help us understand the process of ligand entry to FABP.

Another double point mutant with the HxxxH motif in the second helix was used for further investigation on the role of the second helix. The HxxxH motif in the helix has been reported to be able to bind Ni^{2+} with the assistance of nitrilotriacetic acid (NTA) (27). The metal ion binding should stabilize the helix. Therefore the role of the helix flexibility in ligand entry and exit could be examined.

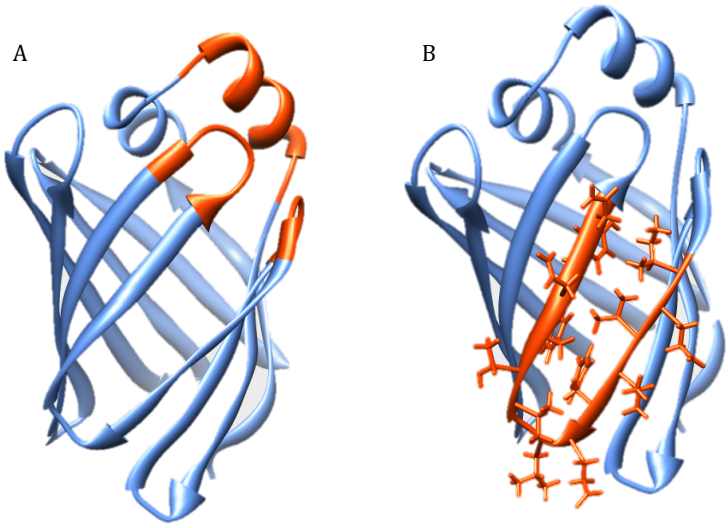

Figure 1.1. *The ribbon representation of the structure of the human intestinal fatty acid binding protein (PDB ID: 3IFB) (28).* ***A.*** *The helical portal region is colored in orange-red.* ***B.*** *The gap D-E is highlighted in orange-red.*

1.4. The gap between strand D and E

The β barrel structure is common in the iLBP family. The binding pocket is located inside the barrel connected by the β strands. The anti-parallel β sheet is featured with hydrogen bonds. However, complete missing of hydrogen bonds between strands D and E makes these two strands unique. The distance between these strands is too large to form hydrogen bonds, but the gap is not open to the external solvent. Instead, the gap D-E is filled with hydrophobic side chains, separating the internal and external solvent (Fig

1.1B). An MD simulation study has reported the involvement of the gap in the exchange between external and internal water molecules, which is essential for ligand binding (16, 19). The gap, helical portal region, and back portal are considered to be the possible water portals (16, 17). The later MD simulations indicated the gap D-E to be another possible portal of ligand entry and exit except for the helical portal (16, 17, 29).

Moreover, the gap region is special in protein folding (30). It is proposed that the β barrel might fold from two pieces of the β sheets like a clam, which closes at the gap D-E (31, 32). The hydrophobic residues in the strand D and E close the clam like a zipper (31, 32). In the fluorescence correlation study, a mutant with the fluorescence probe in the residue C60 (V60 in the wild type protein) was utilized to detect the structure fluctuation during the unfolding process, which occurred in a microsecond timescale (33, 34). The mutation V60N of iFABP resulted in a decrease in the protein stability and a faster folding and unfolding rate (35). The studies on the all-β truncation variant of iFABP, Δ78Δ (K29-R106), indicated that the strands D and E might be prone to aggregation (27, 36). Recent studies on CRABP also demonstrated the significance of the interactions among the aromatic side chains in the gap region for protein stability (21). These observations highlighted the significant role of the gap D-E in protein folding and stability.

The gap D-E plays an important role in ligand binding and protein folding. However, it is largely unknown how this gap is involved in these processes. In this thesis, a double-cysteine mutant V60C/Y70C of hiFABP was generated to investigate how the intra-molecule disulfide bond in gap D-E affected protein folding and ligand binding.

1.5. Lipid delivery and the interaction with membrane

The main function of FABPs is to deliver long chain fatty acids to the target sites. Cellular processes, such as membrane constitution, transcription regulation and immune responses, depend on the interaction of FABP with the membrane. Although the detailed mechanism is still unclear, there have been a few hypotheses based on the experiment observation and MD simulation (29, 37, 38). The two helices have been proved to be critical for lipid transfer by comparing the processes of ligand delivery of liver FABP and intestinal FABP, which indicated the different helical region determined the mechanism of ligand delivery (38). It was reported that iFABP should adopt the 'collision transfer' mechanism initialized by the collision between the helices and the membrane (38, 39). The process of ligand delivery of liver FABP should occur by diffusion (38). The two helices have been proposed to be responsible for sensing the difference in membrane composition and interacting with the membrane, followed by a conformational exchange to 'open' the protein and release the lipid (40). The interaction with membrane should be dependent on the charged residues of the second helix (39-41). Compared with liver FABP, iFABP contains more charged residues in the second helix. MD simulation analysis has suggested three possible pathways for the lipid release from liver FABP, however, for iFABP the helical portal should be the only option for lipid release (14). These studies suggested an indispensable role of the two helices of iFABP in the lipid ligand exit, especially for the second helix. In spite of these impressive findings, the process of lipid delivery by FABP still requires further investigation.

1.6. Basic concepts of NMR

1.6.1. Active nuclei in NMR and free induction decay signal

For protein NMR, the signal comes from the spin of the active nucleus, in which ^{1}H, ^{13}C and ^{15}N are widely used. These nuclei have odd mass and half integral spin quantum number (I = 1/2), which are more suitable for NMR study compared with the nuclei with even mass (I = 0 or 1). In the presence of a magnetic field B, the active nucleus will precess at a specific frequency, namely Larmor frequency ω_0.

$$\omega 0 = -\Upsilon \times B$$

Υ is the gyromagnetic ratio of the magnetic dipole moment to the angular momentum. B is the magnitude of the applied magnetic field. The radiofrequency used to excite the $I_{1/2}$ nuclei transition between Zeeman states is the same as the Larmor frequency in the presence of the external field. In NMR experiment, a radiofrequency pulse will be applied to perturb the bulk magnetization of nuclei to make it rotate away from the alignment with the static magnetic field. Once the pulse is removed, the bulk magnetization will precess about the axis of the static magnetic field, which will be detected by the receiving coil. The process that the spin restores the thermal equilibrium state from the disturbed state will release energy, resulting in NMR signal. The NMR signal will decay along time, which can be described as two types of relaxations, spin-lattice relaxation R_1 and spin-spin relaxation R_2. So the signal detected is called free induction decaying (FID) signal.

1.6.2. Chemical shift

For a macromolecule like protein, the Larmor frequency of each nucleus is varied due to the electron shielding effect due to the electrons nearby,

which is originated from ‘superconducting’ effect. The neighboring electron generates a local magnetic field opposite to the static field. The extent of the shielding effect is dependent on various structural factors. So for the nuclei, like ^{1}H, ^{13}C and ^{15}N, of a protein, each nucleus has a unique resonant frequency. By comparing the resonant frequency with the standard reference like TMS or DSS, the chemical shift (δ) can be defined as follows,

$$\delta = \frac{\omega(\mathrm{H}) - \omega(\mathrm{TMS})}{\omega(\mathrm{TMS}) in\ MHz}$$

Chemical shift is useful in indicating the change of chemical environment. It is widely used in protein structural study, dynamics study, protein-ligand interaction and drug screening (42, 43). Chemical shift index (CSI) plot is widely used to predict the secondary structure pattern of protein. Chemical shift perturbation is suitable for studying ligand-protein interaction.

1.6.3. Chemical exchange

When a nucleus experiences the exchange between two or more different chemical environments, namely chemical exchange, NMR parameters will be affected. The chemical shift observed is affected by the chemical exchange, which can be described by the following parameters: the exchange rate (kex), the chemical shift difference between state A and B and the populations of state A and B.

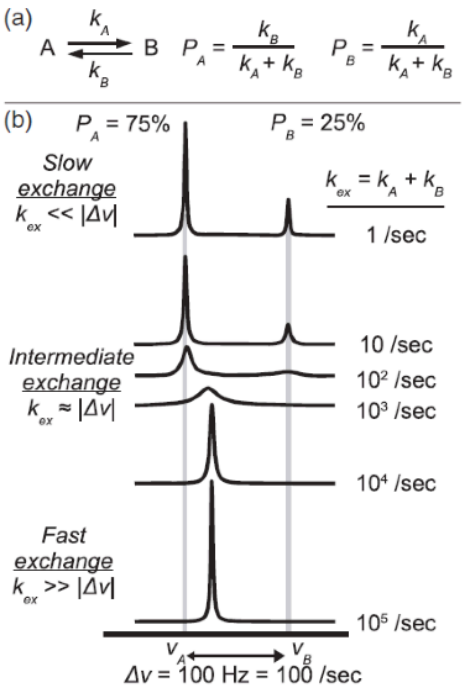

***Figure 1.2**. The resonance peak and its chemical shift are affected by the rate of chemical exchange. The slow chemical exchange results in two separate peaks corresponding to state A and state B. The intermediate exchange results in the broadened peak. The fast exchange results in the single peak. In the figure, v_A and v_B refer to the resonance frequencies of state A and B.*

As shown in Figure 1.2, in the case of fast exchange, the resonance frequency $\omega = p_A \omega_A + p_B \omega_B$ (v_A and v_B in Figure 1.2). For slow exchange, the resonance peaks of state A and B are well separated. In this way, chemical shift can be used as an important probe of protein dynamics relevant to the biological functions, such as ligand binding, protein polymerization and structure adjustment.

1.6.4. J-coupling

Magnetic interaction between two spins can be classified to two types: the direct interaction (dipole coupling) and the indirect interaction (J-coupling). J-coupling, or scalar coupling, is a magnetic interaction through bond. For example, the presence of proton Ha leads to the non-equivalent shielding field to the neighboring spin Hb, resulting in two splitting peaks of Hb. The

shielding field caused by Ha may be aligned with the external field B_0 or opposite to it. The number of splitting peaks increases with the number of the nuclei nearby. J-coupling contains information on bond distances and angles. Vicinal proton-proton coupling constant ($^3J_{HH}$) depends on dihedral angle, following Karplus equation. Therefore, J-coupling has been widely used in the determination of protein secondary structure.

1.6.5. Relaxation

Relaxation refers to the process of an excited magnetic moment returning to the equilibrium state. The magnetization in x-y plane returns to the z-axis, aligning with the external static field. Relaxation can be classified into two classes: spin-lattice relaxation or longitude relaxation (relaxation time T1) and spin-spin relaxation or transverse relaxation (relaxation time T2). For relaxation time T1, the relaxation rate R1= 1/T1, and

$$M_Z = M_{\bowtie} \times (1 - 2e^{-t/T1}).$$

For relaxation time T2, the relaxation rate R2= 1/ T2, and

$$M_{xy} = M_0 \times e^{-t/T2}.$$

T1 relaxation is due to the energy exchange between the spin and the lattice. The energy from radio frequency pulse is released to the surrounding lattice. T2 relaxation is the result of spins getting out of phase. This relaxation is caused by the transient magnetic field at any frequency. T2 relaxation is related to T1 relaxation. Usually, T2 relaxation is faster than T1 relaxation. In solutions, T2 is similar to T1, while in solid T2 is much smaller. For a protein molecule, the relaxation rate is affected by its size, protein motion and the interaction with ligands. Therefore relaxation is an important probe for protein dynamics and functions.

1.6.6. NOE and structure calculation

Nuclear Overhauser Effect (NOE) refers to the magnetization transfer from one proton to another that is spatially nearby through cross-relaxation. NOE is important for protein structure study because it depends on the spatial proximity between protons instead of through-bond J couplings. In this way, NOE can provide the information of the distance between two protons. The strength of NOE is inversely proportional to the sixth power of the distance between the two protons. For proteins, the NOE can be observed between two protons that are no more than 5 Å away from each other.

Nuclear Overhauser Effect Spectroscopy (NOESY) is a widely used technique in structure determination. NOE between two protons is depicted by a correlation peak in a typical NOESY spectrum. For a macromolecule like protein, high-dimension NMR experiment is required due to the crowed peaks in 1D spectra. To determine the structure of a protein, 3D or 4D ^{15}N, ^{13}C-edited NOESY together with ^{15}N-edited HSQC and ^{13}C-edited TOCSY will be needed to assign the NOE peaks, which enables the determination of distances between certain two protons. For structure calculation, the intensities of NOE peaks will be converted to distance based on the relation between the strength of NOE and the distance between two protons.

1.7. Significance

FABP belongs to a classic family of carrier proteins with a β barrel structure. As a carrier protein, FABP is responsible for long chain fatty acids delivery. The function of FABP is closely related to the diverse biological processes. It has been reported that the naturally occurred mutation of FABP is related to insulin resistance and diabetes (44, 45). The roles of FABP in metabolism, signaling pathway, transcription regulation and immune

responses make it a potential target for drug development (4, 6). The importance of FABP's biological function demands immediate attention to understand the molecular mechanism underlying ligand delivery. In the last two decades, intensive efforts have been made to study the mechanism of ligand entry and exit. Although some hypotheses have been proposed, there is no accurate description where and how the ligand enters and exits. This study combined dynamics, structure, and kinetics data of hiFABP variants. The results clarified the mechanism underlying oleic acid incorporation for the first time, successfully characterizing the functionally relevant conformational exchange by NMR relaxation analysis. The mechanism of ligand entry would help to understand the process of ligand releasing of hiFABP. Moreover, the conclusion drawn from the studies on hiFABP would contribute to understanding the mechanism of ligand entry and exit adopted by the other members in iLBP family.

Chapter 2. Materials and Methods

2.1. Mutants of hiFABP

2.1.1. Generation of the Mutants by Polymerase Chain Reaction

The constructs of the hiFABP variants were generated by the one-step or two-step polymerase chain reaction (PCR), using wild type hiFABP (pET45b) construct as the template. PCR reaction mix was prepared in 50 μl mix containing 1 X KOD buffer (20 mM Tris-HCl, pH 7.5 at 25°C, 8 mM $MgCl_2$, 0.5 mM DTT, 50 mg/ml BSA), 1 μM of the forward and reverse primers, 200 μM of each dATP, dCTP, dGTP and dCTP, and 1 μl of 1 U KOD Hot Start Pfu DNA Polymerase (Novagen).

PCR was carried out for 30 cycles, following the subsequent protocol: 95°C of denaturation for 20 sec, 52°C of primer annealing for 20 sec (usually this temperature is adjustable according to the melting temperature of the primer), 70°C of extension for 160 sec, which is dependent on the length of the plasmid. The PCR product was purified with the QIAGEN gel purification kit. The purified product was digested with DpnI to remove the template. The 20ul purified product was mixed with 2ul FastDigest 10 X buffer and 1μl DpnI Fast Digest™, incubate in 37°C for 1 hour. The digested product was strored in -20°C for 30 min to inactivate the enzyme before transformation into the competent cell.

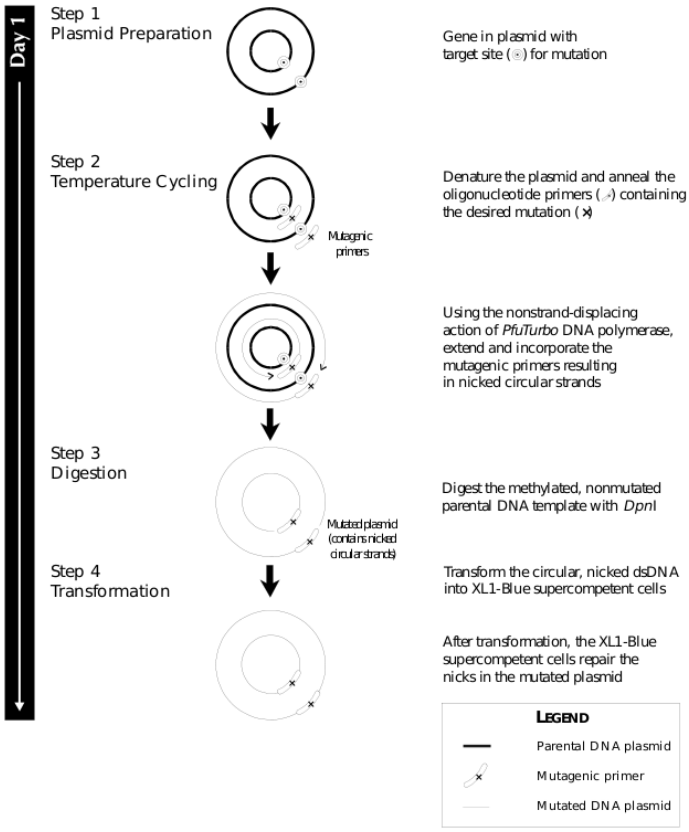

Figure 2.1. *Generation of site-directed mutants. The high fidelity Hot Start KOD DNA Polymerase enabled the amplification of the DNA insert together with the vector. DpnI restriction enzyme was used to remove the methylated wild-type parental DNA template. Finally, the nicked double strand DNA was repaired in the BL21 (DE3) competent cells.*

Primer	Sequence (from 5' to 3')
V26HL30H F	GGAAAAAATGGGCGTGAACATTCATAAACGCAAACATGCGGCGCATGATAACCTG
V26HL30H R	CAGGTTATCATGCGCCGCATGTTTGCGTTTATGAATGTTCACGCCCATTTTTTCC
D74C F	CTATAACCTGGCGTGTGGCACCGAACTGC
D74C R	GCAGTTCGGTGCCACACGCCAGGTTATAG
K27C F	GTGAACATTGTG TGT CGCAAACTGGCGG
K27C R	CCGCCAGTTTGCGACACACAATGTTCAC
V60C F	GTTTCGCAACATTGAA TGT GTGTTTGAACTGG
V60C R	CCAGTTCAAACAC ACA TTCAATGTTGCGAAAC
Y70C F	GTGACCTTTAAC TGT AACCTGGCGGATGG
Y70C R	CCATCCGCCAGGTT ACA GTTAAAGGTCAC
hiFABPNdeI	GGGAATTC CATATGGCGTTTGATAGCACCTGG
hiFABPBamHI	CGC GGATCCTCAATCTTTTTTAAAAATGCG

Table 2.1. *List of primers used to generate the mutants of hiFABP. F: forward primer; R: reverse primer.*

2.1.2. Preparation of competent cells

Frozen glycerol stock of DH5α or BL21 (DE3) was streaked onto plain LB agar plate and incubated overnight at 37°C. A single colony was inoculated into 8 ml of LB broth and incubated in a shaker overnight at 37°C. 1 ml of overnight culture was transferred into 100 ml of LB broth and incubated in a shaker at 37°C with shaking speed of 190 rpm. Cells were grown until $O.D_{600}$ reached 0.2 and then transferred into 50 ml tubes and spun at 3,500 rpm for 10 minutes at 4°C. Supernatant was discarded and cell pellets were resuspended gently with 20 ml of cold glycerol buffer (0.1 M $CaCl_2$, 15% glycerol) and then incubated on ice for 30 minutes. Cells were spun at 3,500 rpm for another 10 minutes at 4°C and the supernatant were removed. The pellet was resuspended carefully in 4 ml of cold glycerol buffer and incubated on ice for 2 hours before aliquoted at 50 µl per tube. The aliquots were quickly frozen in liquid nitrogen before transferring to storage at -80°C.

2.1.3. Subcloning

For the mutant V26H/L30H, the cDNA was subcloned into pET-M, a modified vector from pET-32a with S-tag and thioredoxin tag removed. Due to the ability of this mutant to bind with Ni-NTA, the N terminal His tag was removed using the restriction site NdeI. The cDNA was amplified by PCR. The PCR product was digested using 4 µl of NdeI Fast Digest ™ and BamHI Fast Digest ™ (both from Fermentes) in a total reaction volume of 40 µl. 2 µl expression vector (about 60 ng/µl) was digested in a separate tube with another 10 U of the similar restriction enzyme in total reaction volume of 20

µl. Concentrated 10 X Fast Digest ™ buffer was added accordingly. Both tubes were incubated in 37°C water bath for at least 1 hour.

The vector and DNA insert digestion products were purified, respectively, using the spin column (QIAGEN) with a final elution volume of 20 µl. The vector and the insert were then mixed at the molar ratio 1:7, of which the total volume is 8 µl. The mixture was added 1µl 10 X T4 ligase buffer and 1 µl of T4 ligase enzyme (Fermentes). The ligation was carried out for at least 1.5 hour at room temperature before transformation into DH5 α competent cell.

2.1.4. Transformation into DH5α competent cell

The ligation mixture was added into a tube containing 100 µl of DH5α competent cell and kept on ice for 20 minutes. Heat shock was carried out by incubating the cells at 42 °C for exactly 60 seconds, followed by 3 minutes incubation on ice. 900 µl of LB broth was added into the tube, followed by incubation at 37 °C with shaking for 1 hour to revive the cells. Cells were spined down at 6,000 rpm for 2 minutes and 900 µl of the supernatant were removed. Cell pellet was resuspended with the remaining medium and plated on LB agar plated supplemented with 0.1 mg/ml ampicillin. Plates were incubated overnight in a 37 °C incubator.

2.1.5. Taq PCR screening

The presence of DNA insert inside target plasmid was verified by Taq-PCR screening of colonies grown on LB-ampicillin agar plate prior to DNA sequencing. At least 8 colonies from each plate were selected for screening.

Half of a colony was applied to a sterile pipette tip and inoculated into 2 µl sterile water in a PCR tube. The suspension was mixed with the Taq PCR cocktail, containing 1 X Taq reaction buffer (50 mM KCl, 10 mM Tris-Cl pH 9.0, 1% Triton X-100), 0.75 mM $MgCl_2$, 140 µM of each dATP, dCTP, dGTP and dCTP, 0.5 µM each of forward and reverse primer, and 1.5 U of Taq DNA Polymerase (Promega). The PCR cycle was as follow: melting at 95 °C for 30 sec, annealling at 52 °C for 30 sec and elongation at 72 °C for 30 sec, repeating for 30 cycles. The PCR products were analyzed on a 1% agarose gel for the detection whether the target DNA was inserted.

2.1.6. Extraction and purification of DNA plasmid

Colonies that showed positive PCR screening results were inoculated into LB broth (containing 100 µg/ml ampicillin) and cultured overnight at 37 °C with shaking. The cells from 5 ml of overnight culture were spined down by centrifugation at 13,000 rpm for 1 minutes. DNA plasmid was extracted from pelleted cells using Axygen Miniprep Kit and eluted with 60 µl of elution buffer.

2.1.7. DNA sequencing

5 µl of plasmid DNA (~200 ng of DNA) was added into the reaction mixture containing 9.4 µl of water, 1.6 µl of T7-promoter sequencing primer (10 µM), 2 µl of 5X Big Dye Buffer and 2 µl of Big Dye Terminator V3.1 (Applied Biosystems). Thirty cycles of sequencing PCR reaction were carried out with denaturation step at 96 °C for 30 sec, annealing at 50 °C for 5 sec and extension at 60 °C for 4 min. After the sequencing cycle, a mixture of 3 µl of 3M sodium acetate, pH 4.6, 62.5 µl of 95 % ethanol and 24.5 µl of sterile

water was added into each PCR product for precipitation. After 1 hour (room temperature) incubation at room temperature, the mixture was centrifuged at 15,000 rpm for 25 minutes at room temperature. Supernatant was removed, and the pellet was washed with 800 µl of 70% ethanol and centrifuged for another 5 minutes, repeating for two times. Supernatant was carefully removed and the DNA pellet was dried in a vacuum centrifuge (Speed-Vac) before sequencing analysis on an automated sequencer, ABI PRISM 3100 (Applied Biosystems).

2.2. Protein expression and purification

2.2.1. Transformation of plasmid into BL21 (DE3) competent cell

Plasmid containing DNA insert of wild type hiFABP or the mutants was transformed into *E. coli* BL21 (DE3) cells for the overxpression of recombinant protein.

2.2.2. Protein expression

A single colony of *E. coli* BL21 cells containing the desired plasmid was inoculated into 10 ml of LB broth (containing 0.1 mg/ml ampicillin) and cultured at 37°C overnight with shaking. Ten milliliter of overnight culture was inoculated into 1 liter of autoclaved LB broth (containing 0.1 mg/ml ampicillin) or M9 medium. The cell cultures were grown at 37°C, shaking at a speed of 200 rpm till the $O.D_{600}$ reached approximately 0.6. Subsequently, IPTG was added at a final concentration of 0.5 mM to induce at 20°C at 200 rpm, growing for overnight. The cells were harvested by centrifugation at 5,000 rpm for 20 minutes at 4 °C. The cell pellets can be kept at -20 °C until purification.

Expression of ^{15}N or ^{13}C-labeled protein was carried out with similar conditions as mentioned above, except that the cells were grown in M9 minimal medium supplemented with ^{15}N-labeled ammonium chloride and/or ^{13}C-labeled D-glucose. To obtain a single labelled sample (either ^{15}N-labeled or ^{13}C-labeled sample), cells were grown in 1 X M9 minimal medium in the presence of ^{15}N-ammonium chloride (Cambridge Isotope Laboratories) or with ^{13}C-glucose (Cambridge Isotope Laboratories) as the sole nitrogen or carbon source. For double labeled ^{15}N and ^{13}C-sample, 1 X M9 minimal medium with ^{15}N-ammonium chloride and ^{13}C-glucose (Cambridge Isotope Laboratories) was used as the sole nitrogen and carbon source respectively.

For the cells growing in the deuterated M9 medium, there were some variations in the protein expression. The single colony was first inoculated to the 10 ml LB broth (containing 0.1 mg/ml ampicillin), growing overnight in 37 °C. Then 1ml LB cell culture was diluted to the 100% H_2O M9 medium (100ml) to grow in 37 °C till the OD_{600} was 0.6. The 10 ml M9 culture was diluted to 100 ml M9 medium with 50% D_2O, growing in 37 °C till the OD_{600} was 0.4-0.5. Then the 10 ml M9 culture with 50% D_2O was again diluted to the 100 ml M9 medium containing 100% D_2O, growing till OD_{600} was 0.4-0.5. The 100 ml M9 cell culture was diluted to the 500 ml M9 medium containing 100% D_2O. When the OD_{600} arrived 0.4, the IPTG was added, the final concentration of which is 0.5 mM. The inducing temperature was 20 °C.

2.2.3. Protein purification via Ni-NTA affinity chromatography

The cell pellet was resuspended in 30 ml of Nickel binding buffer (20 mM Tris-Cl pH 8.0, 0.3 M NaCl). The suspension was sonicated for 5 minute each

time at 30% sonication amplitude for 3 times. The lysate was centrifuged at 4°C for 45 minutes at 12,000 rpm to separate the soluble and insoluble components. The supernatant was shifted to the new 50 ml eppendof tube for purification. Around 5 ml of Ni-NTA beads (QIAGEN) were charged with 15 ml of Nickel-charge buffer (0.2 M $NiSO_4$), washed with 4 colume volume (CV) of water and equilibrated with 4 CV Nickel binding buffer. All supernatant was slowly loaded into the column, mixed well. The slurry was transferred to the 50 ml falcon tube to incubate for 1 hour in the cold room. The flow-through was collected after the incubation. The Ni-NTA beads were then washed with the the wash buffer (20 mM Tris-Cl pH 8, 0.5 M NaCl, gradually increased imidazole concentration 5-20 mM) to remove the unspecifically bound proteins. The target protein was eluted out using 20 ml of nickel elution buffer, eluting for 3 times (20 mM Tris-Cl pH 8, 0.5 M NaCl and 50-300 mM imidazole). The eluted protein was analyzed by SDS-PAGE, and then the pure fractions were dialyzed overnight against the phophate buffer (20 mM sodium phosphate, 20 mM NaCl, pH 7.1) to remove the imidazole and for the next purfication.

2.2.4. Gel filtration by Fast Protein Liquid Chromatography (FPLC) (Fast Protein Liquid Chromatography)

Gel filtration was conducted using a HiLoad 16/60 Superdex 75, pg size exclusion chromatography column on AKTA FPLC System (Amersham Biosciences). The buffer for gel filtration was the phosphate buffer, containing 20 mM sodium phosphate, 20 mM NaCl, pH7.1. The gel filtration column was first equilibrated with ~1.2 CV (150 ml) of the phosphate buffer before

injecting protein. The protein sample was concentrated to around 5 ml prior to loading. The protein sample was centrifuged to remove any precipitants before loading and injecting. After injection to the column, the protein was eluted and separated with the impurities in a flow rate of 1 ml/min. The elution length was 150 ml, making sure that all the components of the sample came out. Eluted protein peaks were detected by measuring UV absorbance at 280 nm and the respective fractions were analyzed by SDS-PAGE.

2.2.5. Delipidation

Due to the capability of FABP to bind with fatty acids and other similar ligands, the purification of the mutants and the wild type hiFABP requires the additional step to remove the bound ligand by extracting with diisopropyl ether and butanol (46). The fractions of the gel filtration were collected and diluted to 25 ml with the same phosphate buffer. The organic phase used for extracting the lipids and the lipid-similar ligands was the mixure of the diisopropylether and the 1-butanol (3:2 v/v). The protein solution was mixed with the organic mixure (2:1 v/v), shaking gently (17 rad/s) in the room temperature for 30 min. Then the extracting mixture was left on the table to let the two phases separate. the organic phase was removed and discarded. The protein solution was shifted to a new tube, mixed with the organic mixture again and shaking for another 30 min. The extracting was repeated for 6 times. The extraction contained some butanol, so the protein solution needed to be buffer exchanged by diluting the protein sample with the phosphate buffer followed by concentration. The final protein sample should contain mostly the apo form, only ~5% holo form remained.

2.2.6. Activated thiol 4B sephorase beads (GE Health)

For the mutant V60C/Y70C, the two Cysteines could not form the disulfide bond completely, and the protein sample was a mixture of the two forms. To obtain the pure form of the mutant with the intra-molecule disulfide bond, the factions after gel filtration were collected and unfolded with 8M urea. The pH of the unfolded protein sample was adjusted to 8.0. The 4ml activated thiol 4B beads were packed into the column and equillbriated with the buffer containing 8M urea. The unfolded protein was then loaded to the column and mixed with the beads thoroughly. The slurry was incubated for 1 hour in room temperature to make sure protein with the free thiol group bind fully to the beads. After incubation, the flow-through was collected, which contained only the form with the intra-molecule disulfide bond. The bound protein was then eluted with 20ml buffer containing 20 mM DTT.

2.3. Dynamic light scattering (DLS)

Using DynaPro Dynamic Light Scattering (ProteinSolutions) machine linked to a temperature controlled MicroSampler (ProteinSolutions), dynamic light scattering was utilized to make sure no aggregation in oleic acid before performing stopped-flow experiment. Twenty microliter of oleic acid solution (100 μM, pH 9.4) was loaded into a quartz cuvette with a path length of 15 mm (ProteinSolutions). Data were recorded and analyzed using the Instrument Control Software for Molecular Research (ProteinSolutions).

2.4. Fluorescence spectroscopy

The protein sample (150 µl) was loaded in PerkinElmer luminescences cell and fluorescence spectra were recorded via Shimadzu RF-5301 fluorescence spectrometer. For ANS titration experiment, ANS concentration was fixed to 1 µM final concentration with protein concentration changed from 0 µM to 500 µM. The excitation wavelength was 375 nm, and emission wavelength was 480 nm. The peak area was calculated. The area of the binding enhanced peak (F) was normalized by comparing with the peak of ANS ($F_{ANS,0}$) only and the peak of buffer only ($F_{0,0}$):

$$F_{Normalized} = (F-F_{ANS,0})/(F_{ANS,0} - F_{0,0}).$$

The dissociation constant (K_D) was calculated by least square fitting to the following equation:

$$F_{Normalized} = (\emptyset - 1)\times(A + x + K_D - \sqrt{(A + x + K_d)^2 - 4\times A\times x}) \,/\, 2A$$

A refers to the concentration of ANS, which was fixed in fitting. x refers to the protein concentration. ϕ refers to the enhancement coefficient upon protein binding.

2.5. Stopped-flow fluorescence experiment

The stopped-flow fluorescence experiment is widely used in the kinetics study on protein-ligand interaction, protein unfolding and enzyme activity assay. This technique detectes the real-time change of the emission fluorescence before it arrives the steady state. In the case of our study, the stopped-flow fluorescence experiment monitored the increase of the intrinsic fluorescence signal of Trp. The buffer for the reaction of oleic acid binding to

FABP was pyrophosphate buffer (50 mM sodium pyrophosphate, 50 mM NaCl, pH 9.4). The protein was redueced by adding 5 mM DTT and incubating for overnight in the fridge. The final protein concentration used for the stopped-flow experiment was 1~3 μM. The final ligand concentration was varied between 5~100 μM. The experiments were performed on Applied Photophysics stopped-flow spectrophotometer. For each mixing, it took 1 ml protein sample and 1 ml oleic acid solution. The dead time was 1 ms. For each oleic acid concentration, the experiment was repeated for 10 times to minimize the noise, which were averaged before fitting. The stopped-flow traces were first subtracted by the trace of the control experiment (mixing the protein with the buffer), then fitted to double exponential function:

$$F(t) = -A1 \times Exp(-k_{obs1} \times t) - A2 \times Exp(-k_{obs2} \times t) + F_{max}$$

A1 and A2 were the amplitudes of the two exponential components, depending on the reaction. The two apparent rates k_{obs1} and k_{obs2} were the apparent rates of the two components. F_{max} was the fluorescence signal of the equilibrium state.

Besides the least squared fitting, the stopped-flow traces were also analyzed by another software Dynafit to extract the kinetics parameters (47). In the model used for the fitting of the stopped-flow traces, there were 5 molecular species: $FABP_{cl}$, $FABP_{op}$, $FABP_{op}L$, $FABP_{cl}L$ (different conformations of hiFABP) and L (oleic acid).

$$FABP_{cl} \leftrightarrow FABP_{op} \ (step\ 1)$$

$$FABP_{op} + L \leftrightarrow FABP_{op}L \ (step\ 2)$$

$$FABP_{op}L \leftrightarrow FABP_{cl}L \ (step\ 3)$$

Model I

The first order differential equations are as follows:

$$\frac{d[P1]}{dt} = -k1[P1] + k_{-1}[P2]$$

$$\frac{d[P2]}{dt} = k1[P1] - k_{-1}[P2] - k2[P2][L] + k_{-2}[P2L]$$

$$\frac{d[L]}{dt} = -k2[P2][L] + k_{-2}[P2L]$$

$$\frac{d[P2L]}{dt} = k2[P2][L] - k_{-2}[P2L] - k3[P2L] + k_{-3}[P1L]$$

$$\frac{d[P1L]}{dt} = k3[P2L] - k_{-3}[P1L]$$

[P1] refers to the concentration of $FABP_{cl}$. [P2] refers to the concentration of $FABP_{op}$. [P2L] refers to the concentration of $FABP_{op}L$. [P1L] refers to the concentration of $FABP_{cl}L$. [L] refers to the concentration of oleic acid. k1, k-1, k2, k-2, k3 and k-3 are reaction rates.

The solution to the first order differential equations was obtained by numerical integration. The stopped-flow traces of various oleic acid concentrations were loaded for fitting. The parameters used for fitting were the forward rates k1, k2 and k3 and the reverse rate k-2, the fluorescence response for 1 μM $FABP_{op}L$ and $FABP_{cl}L$. The ratio k-1/k1 and k-3/k3 were fixed to 50 and 0.01 respectively.

2.6. The measurement of amide proton exchange rates using radiation damping effect

This method utilized radiation damping effect to select the magnetization of water proton. The pulse sequence and the data analysis were as described in the previous study (48). There were two interleaved data sets acquired in the presence and absence of the gradients G2 and G0, which suppressed the water magnetization recovery. When the magnetization of water proton recovered but the one of amide proton inverted, the magnetization of the water poton was transferred to the amide proton through the proton exchange process. Along with the increase of the mixing time, there was more magnetization transferred. The first spectrum with the long inter-scan delay (2 s) was recorded as the reference. For extracting the proton exchange rate, 16 spectra with varied mixing time were recorded: 20, 30, 40, 50, 60, 70, 80, 90, 100, 120, 140, 160, 190, 220, 260 and 300 ms. For each data set, there were 100×640 complex points in the ^{15}N and ^{1}H dimensions. To measure the longitudinal relaxation rate of the water (R_{1W}), it was measured by the saturation recovery method.

For data processing, the peak intensities of each exchanging spectrum were divided by the intensities of the reference spectrum. The Iex/Iref was again divided by 2 since each spectrum contained two interleaved data sets. The Iex/Iref was plotted along the mixing time. The curve was fit with the euqation:

$$\frac{Iex}{Iref} = \frac{f \times kex}{R1 + kex - \mathrm{R1W}} \times \left[Exp\left(-\mathrm{R1W} \times (\mathrm{t} - \mathrm{t0})\right) - Exp\left(-(\mathrm{R1} + \mathrm{kex}) \times (t - t0)\right) \right].$$

Least-square fitting was done using Matlab.

Amide proton exchange rates of the unstructured protein (k_{rc}) were predicted by the online software ClntX (49). The ratio k_{rc}/k_{ex} was the protection factor, in which k_{ex} refers to the proton exchange rate of the native protein measured in the experiment.

2.7. H/D exchange and ^{15}N-HSQC spectra

The H/D exchange experiment is suitable for the measurement of the slow proton exchange rate in minute timescale. Before the experiment, protein sample was lyophilized. During the experiment, the lyophilized sample was first desolved in the D_2O buffer immediately before recording the ^{15}N-HSQC spectrum. A series of the HSQC spectra were recorded along the time. The relative peak intensity of each reasonance peak was plotted on the time. By fitting the curve to the equation:

$$I(t) = I_0 \times Exp(-t \times kex) + I_{\bowtie}.$$

The parameter k_{ex} was amide proton exchange rate. I_0 was the relative peak intensity when the time was zero. I_∞ was the relative peak intensity of when the time was ∞.

2.8. Urea denaturation experiments detected by fluorescence spectroscopy

In urea denaturation experiment, protein stock was diluted with the different denaturation buffers, containing urea in varied aconcentration (0~8 M). The final protein concentration was 4 μM, in pH 7.1.

Protein samples were loaded into the fluorescence cuvette with a path length of 10 mm (Perkin Elmer Instruments), and fluorescence spectra were recorded using Shimadzu RF-5301 fluorescence spectrometer. the excitation wavelenght was 280 nm, and the emission wavelength was 335 nm. The peak area (290 nm-450 nm) was calculated for data analysis. The peak areas of different urea concentration were normalized by first subtracting the lowest value and then dividing by the highest value. Curve fitting was done with proFit 6.2.9. The equation used for fitting was as follow (50) (51):

$$F = Y1 + m1\times x + (Y2 + m2\times x)\times Exp(m\times(x - Cm)/RT)/(1 + Exp(m\times(x - Cm)/RT))$$

The F is the fraction of denatured protein.Cm is the mid-point of chemical denaturation. m refers to the slope of ΔG^0 depending on urea concentration. Y1 and Y2 refer to the intercepts of folded and unfolded states. m1 and m2 refer to the slopes of pre- and post-transition states. T is Kelvin temperature, and R is gas constant (50, 51).

2.9. Isothermal titration calorimetry (ITC)

ITC experiment was conducted on a Micro VP-ITC mechaine at 25 °C. The concentration of protein sample was 60 μM, and the concentration of Cu-NTA solution was 6 mM. The cell volume was 1.8 ml and the syringe volume was 300 µl. The buffer was Tris-HCl buffer, pH 7.0 (20mM Tris-HCl, 20mM NaCl). Cu-NTA solution was titrated gradually, in total 30 drops. For the protein sample and the Cu-NTA solution, they were centrifuged at 13500 rpm for 30 min to make sure no precipitant, followed by degasing. Data analysis was done by Origin 5 package, using one-site model to fit.

2.10. Relaxation dispersion analysis

CPMG experiments were done in 13 °C for variant K27C/D74C (with the disulfide bond). The buffer used in this experiment was phosphate buffer (20mM sodium phosphate, 20 mM NaCl, pH 7.1). The protein was expressed in *E. coli* growing in 100% D_2O M9 medium as mentioned above. The protein concentration was 1mM.

In the CPMG experiment, spin-echo pulse elements with varied inter-pulse delays (CPMG frequency v_{CPMG}) was used to refocus the exchange broadening of magnetizations (52). In the presence of the conformational exchange, the effective R2 ($R2_{eff}$) was varied on the CPMG frequency. For each spin, the exchange rate (k_{ex}), the populations of the different forms and the chemical shift difference were determined by non-linear least fitting to the two-state model or three state model. All the ^{15}N dispersion profiles and most of the ^{1}H profiles were globally fitted to the two-state model. Some of the ^{1}H dispersion profiles were fitted to the three-state model due to the insufficiency of the two-state model.

2.11. Nuclear magnetic resonance (NMR) and structure calculation

2.11.1. 2D ^{1}H-^{15}N HSQC spectrum

2D ^{1}H-^{15}N HSQC spectrum was used as a reference for backbone chemical shifts assignments of 3D or 4D experiments. The spectrum was acquired with 1280 complex points over a spectral width of 11160.714 Hz on ^{1}H dimension. In the ^{15}N dimension, 256 points were collected over 2108.370 Hz. Carrier frequencies for ^{1}H and ^{15}N were at 4.782 ppm and 119.079 ppm respectively.

2.11.2. ^{15}N-edited NOESY and ^{15}N HSQC for the backbone assignment of the three mutants

The distance restraints between amide protons and the protons nearby were derived from 3D ^{15}N-edited Nuclear Overhauser Effect spectroscopy (NOESY). The mixing time was 100 ms. 2D ^{15}N-HSQC spectra and 3D ^{15}N-edited-NOESY spectra were utilized to assign the resonance peaks in the ^{15}N-HSQC spectra of the three mutants. Based on the knowledge of the assignments of wild type hiFABP done before, the backbone assignment was done based the comparison between the NOE pattern and the structure of wild type hiFABP.

All NMR spectra were recorded on a Bruker AVANCE 800 MHz spectrometer equipped with a cryoprobe. Samples were contained in a 5 mm NMR tube. The NMR data were processed using NMRPipe (53) and NMRDraw (53). The data analysis and the assignment were done using SPARKY (Goddard and Kneller) and NMRSpy (Zheng, Yu; Yang, Daiwen. NMRspy, National University of Singapore).

2.11.3. 4D ^{13}C, ^{15}N-edited NOESY of hiFABP variant K27C/D74C

For the mutant K27C/D74C (the form with the disulfide bond), the structure calculation was done using the ^{15}N-HSQC, ^{13}C-HSQC, HNCA, HN(CO)CA, 4D ^{15}N, ^{13}C-edited-NEOSY and ^{13}C-edited-HCCH-TOCSY (54). These experiments were done in 303K.

When assigning the peaks in ^{15}N-HSQC, ^{13}C-HSQC, 4D NEOSY and HCCH-TOCSY, clusters were identified by matching the HC-HN NOESY and HNCA spectrum with the same NH chemical shifts. Spin systems were sorted out, differentiating the intra-residue and sequential HC-HN NOE correlation

peaks from the inter-residue NOEs in the 4D ^{13}C-^{15}N-edtited NOESY spectrum combining with HNCA, HN(CO)CA and HCCH-TOCSY. Clusters of the corresponding residues were linked based on sequential NOE peaks and the NOE patterns. The linkage generated several fragments of the residues, together of which were then fitted to the protein sequence (54). In this way, the backbone assignment and the side chain assignments were done. The assignment of the NOE peaks were done based on the chemical shifts in the atom list.

The HN-HN, HC-HN and HC-HC NOEs were submitted for structure calculation, using the software CNS solve 1.3. Besides NOE distance restraints, dihedral angel restraints (generated by TALOS) and hydrogen bonds were used for the structure calculation.

Chapter 3. The Double Cysteine Mutant K27C/D74C

3.1. Result

3.1.1. Double point mutant and the intra-molecule disulfide bond

The helical portal region has been proposed to be the site of oleic acid entry for twenty years (11, 20, 24). However, this hypothesis is based on the comparison of the dynamics and the structures between apo and holo protein. The process of fatty acid entry is still vague. To inspect the 'helical portal region' hypothesis and clarify the process of fatty acid entry, we introduced an intra-molecule disulfide bond in the helical portal region by double point mutation to stabilize the helical portal region and examine the impact on the process of ligand entry.

Figure 3.1. *The ribbon representation of the wild type hiFABP (PDB ID:3IFB). The residues K27 and D74 are mutated to Cysteine, highlighted in red.*

Residue K27 and D74, located in the second α-Helix and the turn E-F respectively, were mutated to cysteines (Figure 3.1). By comparing the ^{15}N-HSQC spectra of the reduced form and non-reduced form of this mutant, as shown in Figure 3.2, we found the two cysteines could form a disulfide bond completely. In the absence of the reducing agent DTT, no visible dimer was

found by gel filtration or non-reducing SDS-PAGE. After incubation with DTT overnight, the changes of chemical shifts in the HSQC spectrum were observed. The peaks of the residues in the second α-Helix, I25-D34, and the residues in the turn E-F (G75 and T76) showed significant changes in their chemical shifts after the DTT treatment, supporting the existence of the disulfide bond. Besides these residues, the peaks of the residues in the first helix and β-turn C-D, like M21 and R56 also exhibited different chemical shifts. These residues were proximal to the mutation points. The difference in the chemical shifts should be caused by the change of local chemical environments when there was a disulfide bond.

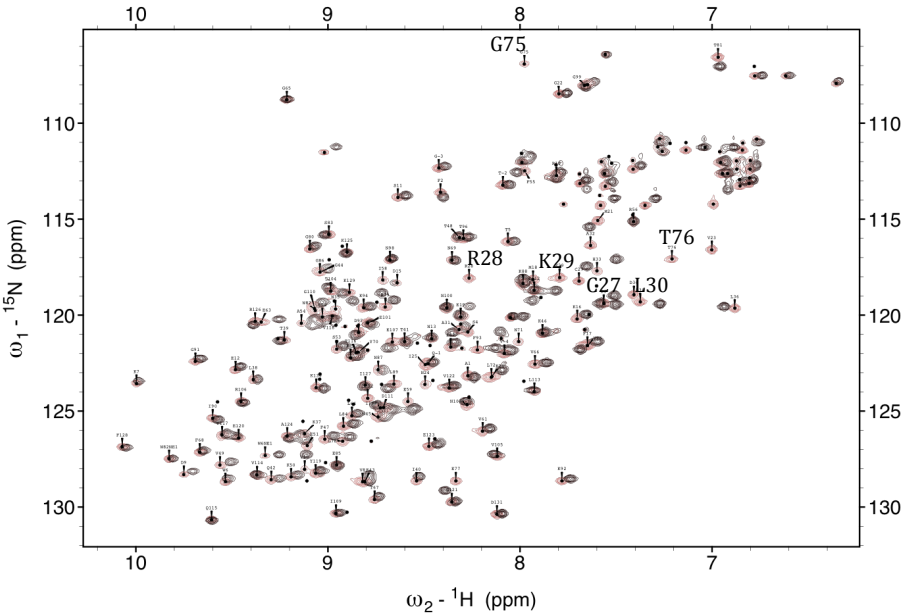

Figure 3.2. *The ^{15}N-HSQC spectra of the mutant K27C/D74C with and without DTT treatment. The spectrum of the mutant without the DTT treatment is shown in red; the spectrum of the mutant with 5mM DTT treatment is shown in black. Both of the spectra were recoded at 30 ^{0}C, pH 7.1, 20mM sodium phosphate and 20mM NaCl.*

3.1.2. The effect of the disulfide bond on global stability

To investigate the effect of the intra-molecule disulfide bond on global stability against urea denaturation, steady state fluorescence spectra were recorded in the presence of urea at varied concentrations. Fitting of the

denaturation curves was based on a two-state conversion model as mentioned in Chapter 2. The denaturation curves are illustrated in Figure 3.3. The mid-point of the mutant with the intra-molecule disulfide bond was 4.12±0.07 M, while the mid-point of the reduced mutant was 3.32±0.07 M. The shift of the mid-point suggested that the intra-molecule disulfide bond increased the stability against chemical denaturation significantly. The ΔG^0 of the mutant with the intra-molecule disulfide bond was higher than the reduced form by 5.5 kJ/mol, also indicating a more stable structure in the presence of the disulfide bond. The m-value of the reduced mutant was slightly smaller than that of the mutant with the disulfide bond or wild type hiFABP, suggesting that the difference in accessible surface area (dASA) between the folded and the unfolded forms deceased to some extent in the absence of the intra-molecule disulfide bond.

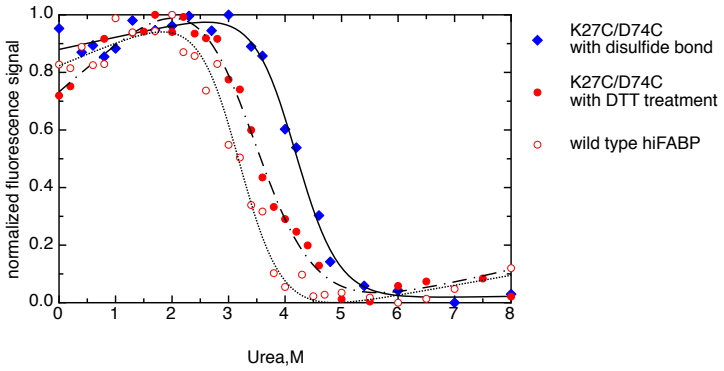

Figure 3.3. *Chemical denaturation of the mutant K27C/D74C with the intra-disulfide bond, treated with 5mM DTT and wild type hiFABP. The protein was denatured with urea in the concentration varied between 0~8M, in room temperature, pH 7.1. The protein concentration was 4 μM.*

	m-value (kJ/mol/M)	mid point (M)	ΔG^0 (kJ/mol)
wild type hiFABP	5.50±0.815	3.11±0.088	17.11±0.151
K27C/D74C with DTT treatment	4.75±0.523	3.32±0.070	15.76±0.112
K27C/D74C with disulfide bond	5.15±0.636	4.12±0.073	21.23±0.125

Table 3.1. *The parameters extracted from the urea denaturation curves. The experiment was conducted in room temperature. The pH of the buffer is 7.1. The protein concentration was 4 μM.*

3.1.3. The effect of the disulfide bond on the flexibility of the helical portal region

Hydrogen bond plays a significant role in protein stability. The rate of the exchange between amide proton and solvent proton is determined by a number of factors including solvent accessibility, pH, temperature, and local flexibility (48) (55). The exchange between amide proton and solvent proton happens after the transition between the 'closed' and the 'opened' forms of a protein (56). In this way, the exchange rate of amide proton can reflect the flexibility of the residue that the amide proton attached to.

To investigate whether the intra-molecule disulfide bond limited the mobility of the helical portal region, we measured the amide proton exchange rates via a special NMR experiment utilizing radiation damping effect (48). Different from the traditional method in which the protein is deuterated, this method is easier and suitable to measure the exchange rates between 0.5~100 s^{-1}, which is too fast to be measured by the conventional H/D exchange NMR method. Figure 3.4 shows the amide proton exchange rates of wild type hiFABP, the mutant K27C/D74C in the presence (blue bar) and the absence (red bar) of the disulfide bond at pH 7.1. As shown in the upper plot of Figure 3.4, the reduced form of the mutant (red bar) had a similar pattern to wild type hiFABP (red empty circle), except for residues N57, G75 and T76 due to the lack of peak intensity in the HSQC spectra, thus measurement of the exchange rate was impossible.

For the reduced mutant, the residues with the exchange rate faster than 5 s^{-1} were I25, C27, R28, K29, A32, H33, D34, N35 (the second α-Helix), D15 (the first α-Helix) and G44, N45, A54, E59, T67, L72, G86, N87 and G110 (loops), which are mapped in the 3D structure (Figure 3.5A). For with type hiFABP, the residues exhibiting the fastest amide proton exchange rates were

also distributed in the region highlighted in Figure 3.5A, but the exchange rates of these residues were faster than those of the reduced mutant. This global decrease in proton exchange rate should be caused by the point mutations at K27 and D74.

When the two cysteines formed intra-molecule disulfide bond, the amide proton exchange rates of the most residues followed a similar pattern to the reduced form without the disulfide bond and wild type hiFABP, except for those located in the second α helix. The bottom panel in Figure 3.4 shows the amide proton exchange rates of residue I25-N35 (the second α-Helix). The exchange rates of the residues in the second α helix decreased significantly in the presence of the intra-molecule disulfide bond between Cys27 and Cys74. In particular, residues C27, R28 and K29 exhibited decreased exchange rates between 0.9 s^{-1} ~ 2.7 s^{-1}, around 10% of the rates of the reduced form. This decrease suggested that the second α-Helix became less flexible due to the limitation of the intra-molecule disulfide bond. Besides the residues in the second helix, the two forms of the mutant K27C/D74C also exhibited difference in the turn between β strands E and F (72-76). In the reduced form of the mutant, the correlation peaks for residues 73-76 were not visible in the ^{15}N-HSQC spectrum, and thus their exchange rates could not be measured. However, the peaks for residue G75 and T76 became visible in the HSQC spectrum after the intra-molecule disulfide bond forming, suggesting the less flexibility of these two residues in the presence of the disulfide bond. The residue L72, which was visible in the HSQC spectra of both forms of the mutant, became more stable when the disulfide bond formed, and the exchange rates were 0.3 and 9 s^{-1} respectively in the presence and absence of disulfide bond. This result suggested that the intra-

molecule disulfide bond stabilized the second α-Helix and the turn E-F effectively.

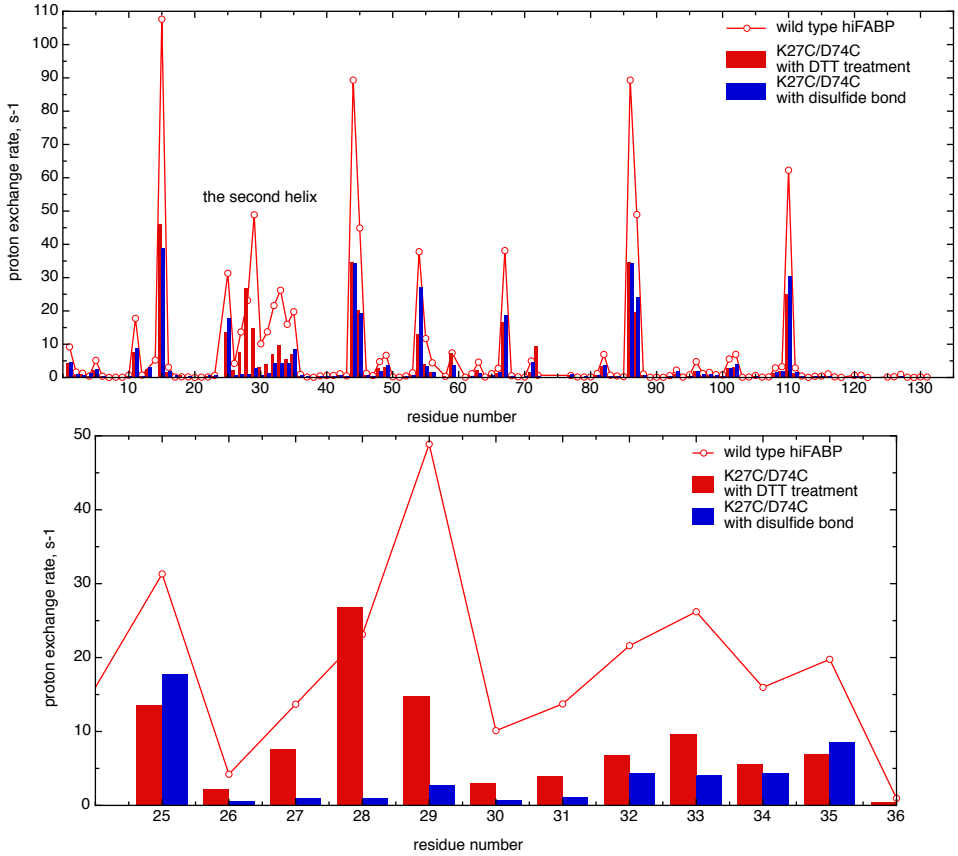

Figure 3.4. *The exchange rates of the amide protons exchanging with water of the mutant K27C/D74C in the presence (blue) and the absence (red) of the disulfide bond as well as the wild type hiFABP. The upper figure shows the exchange rates of all the residues (A1-D131). The residues N24, N57, G75 and T76 are invisible in the HSQC spectrum in the reduced form of the mutant, and the residues N57 and V60 are invisible in the HSQC spectrum of the mutant with the disulfide bond. So the comparison of the exchange rates between these residues were not included in the figure though the exchange rates of them were available in the presence of the disulfide bond. The bottom figure shows the exchange rates of the residues in the second α-Helix (I25-N35).*

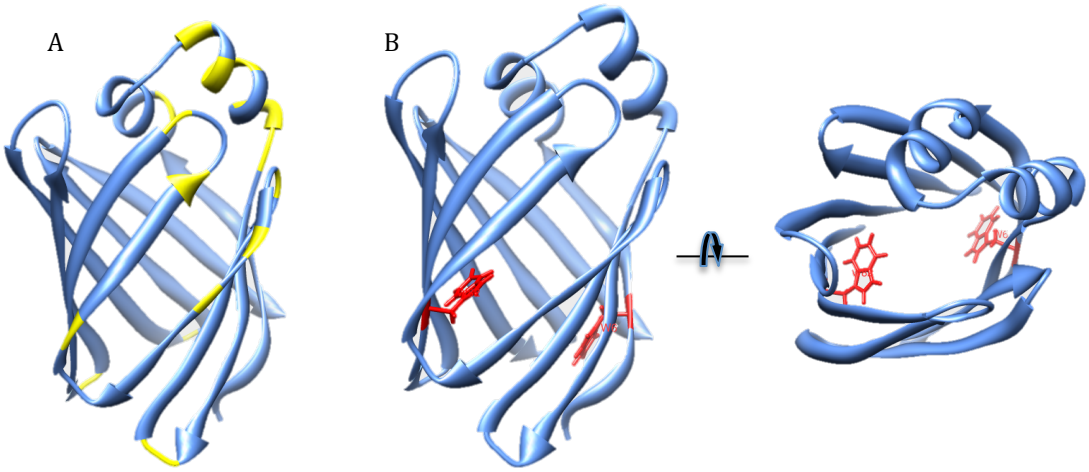

Figure 3.5. *The ribbon representation of the structure of the human intestinal fatty acid binding protein (PDB ID: 3IFB). A. The residues with the fast exchange rates with the solvent protons are highlighted in yellow. B. The two Trps are highlighted in red (28).*

3.1.4. Kinetics of oleic acid binding measured by stopped-flow

To investigate the effect of the intra-molecule disulfide bond on oleic acid binding to hiFABP and the mechanism underlying this process, stopped-flow fluorescence spectroscopy was utilized to measure the rates of oleic acid association at the various concentrations of oleic acid. In the stopped-flow experiments, the increase of the intrinsic Trp fluorescence signal was measured on the reaction time. hiFABP contains two Trp, Trp6 and Trp82, at the bottom of the β-barrel in the oleic acid binding pocket (Figure 3.5B). The traces are shown in Figure 3.6. For each oleic acid concentration, the background of stopped-flow traces was removed by subtracting the trace of the control experiment, in which the protein was mixed with buffer without any oleic acid.

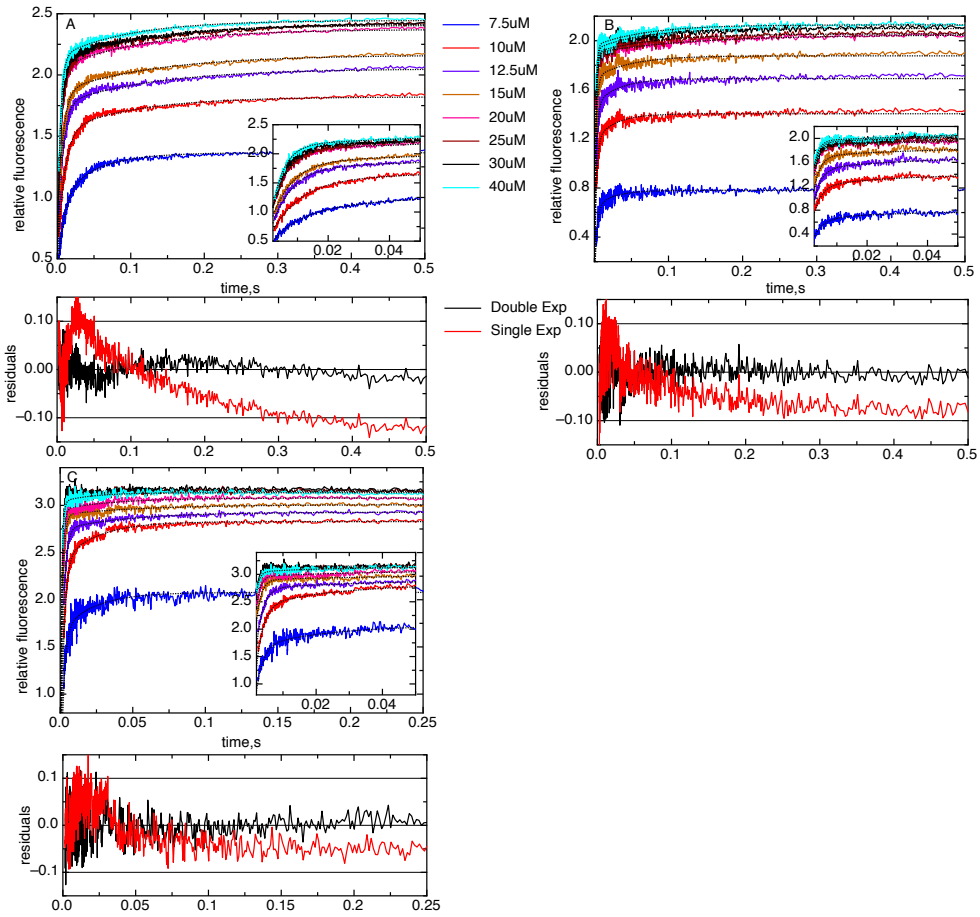

Figure 3.6. *The stopped-flow traces of the oleic acid binding to the mutant K27C/D74C with the disulfide bond (A), K27C/D74C treated with 5mM DTT (B) and the wild type hiFABP (C) in 20 °C. The final protein concentration was 3uM (K27C/D74C with disulfide bond) ~ 4uM (K27C/D74C with DTT treatment and wild type hiFABP). The temperature was 19 °C, in 50mM pyrophosphate buffer, pH 9.4. The final concentration of the oleic acid was between 7.5~100uM. Not all of the traces of the reactions with the oleic acid in different concentrations were included. The final concentrations of the oleic acid included in graphs are 7.5uM, 10uM, 12.5uM, 15uM, 20uM, 25uM, 30uM, 40uM. The inset graphs show the fitted curves and the stopped-flow traces. The graphs below the stopped-flow traces show the comparison between the residuals of the fitting with the single exponential function and the one with the double exponential function.*

In stopped-flow experiment, the apparent reaction rates are usually extracted by fitting the traces to a single or multiple exponential function as described in Methods and Material. In the case of the reaction between the hiFABP and oleic acid, the relative fluorescence could be fitted well to a double exponential function but not a single exponential function, and the triple exponential function could not improve the fitting quality further. In Figure 3.6, the fitting residuals for the single and the double exponential

functions are compared. The single exponential function was obviously not enough to fit the traces properly. This indicated that the binding reaction should not be a simple one-step reaction (57, 58). By fitting the stopped-flow traces to the double exponential function, we found one fast step, which showed a dependence on the ligand concentration, and one slow step, which had little dependence on the ligand concentration. The two apparent reaction rates extracted from the fitting are shown in Figure 3.7. Both of the two steps had positive amplitudes. As shown in Figure 3.7A, the apparent rate (k_{obs}) of the fast step became slower after the two cysteines forming the intra-molecule disulfide bond. The mutant K27C/D74C with the disulfide bond had a k_{obs} slower than the reduced form by 50% for the fast step. The fast step k_{obs} of the reduced mutant K27C/D74C was also slower than that of wild type hiFABP by 40%. The apparent rates of the slow step are shown in Figure 3.7B. The apparent rate of the slow step of the reduced mutant was slightly faster than the mutant with the disulfide bond. Combined with the result of the amide proton exchange experiment, the decrease in both of the fast and slow apparent binding rates should be caused by the reduced flexibility of the helical portal region, suggesting a crucial role played by the helical portal region.

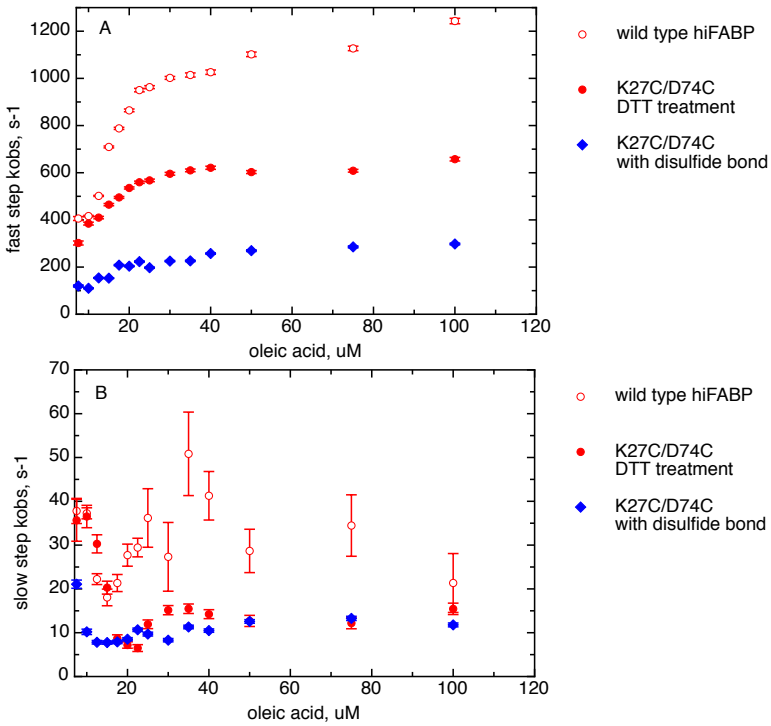

Figure 3.7. *The apparent reaction rates of the two phases extracted from the stopped-flow traces. The oleic acid in varied concentration reacted with the mutant with the disulfide bond, the mutant treated with 5mM DTT and wild type hiFABP. The temperature was 19 °C.* ***A****. The apparent reaction rate of the fast step of the oleic acid binding with the mutant, K27C/D74C with the intra-molecule disulfide bond (blue) and with 5mM DTT treatment (red) as well as wild type hiFABP (red empty circle).* ***B.*** *The apparent reaction rate of the slow step of the oleic acid binding with the mutant, K27C/D74C with the intra-molecule disulfide bond (blue) and with 5mM DTT treatment (red) as well as wild type hiFABP (red empty circle).*

In addition, we tried to measure oleic acid dissociation rate by mixing the oleic acid bound protein with buffer. The stopped-flow traces of the non-reduced form of the variant K27C/D74C are displayed in Figure 3.8. The trace of mixing apo form of the variant was used as the control. However, we failed to observe the decaying of the fluorescence signal with the amplitude corresponding to the one of oleic acid association experiment. The same result was observed in the case of wild type hiFABP and the reduced form of the variant. This observation suggested that oleic acid dissociation should also be limited by a slow reaction happening prior to the dissociation, otherwise a decaying should be observed when mixing the ligand-bound protein with the buffer. The early studies reported the dissociation happening

in the presence of the modeled membrane (37, 39). It is possible that the membrane alters the equilibrium of the reaction, triggering the process of oleic acid release.

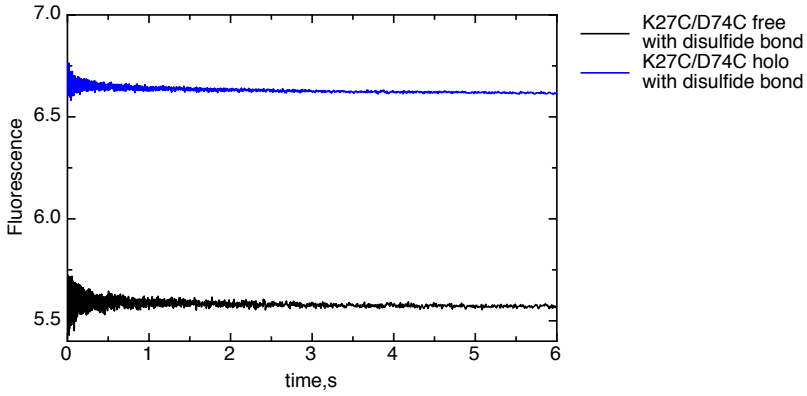

Figure 3.8. *The measurement of k_{off} by stopped-flow experiment. The mutant K27C/D74C (6μM) with the intra-molecule disulfide bond was first saturated with 50μM oleic acid. The saturated protein was then mixed with the buffer in equal volume (blue trace). The experiment was repeated 10 times. As a control, the apo mutant was also mixed with the buffer (black trace).*

3.1.5. Multistep reaction model of oleic acid binding to iFABP

The insufficiency of the single exponential function for describing the binding reaction indicated that the binding of the oleic acid to IFABP should not be a simple one step reaction. The dependence of the apparent rate on the ligand concentration is shown in Figure 3.7, which also indicated a multistep process. For all of the three samples used here, the apparent rates of the fast step increased non-linearly with the oleic acid concentration and reached a plateau. The fast step should be the oleic acid binding step, which was treated as a pseudo first order reaction characterized by the increase of the apparent rate on the ligand concentration. The plateau suggested a rate-limiting step before the fast step. So the fast step should be corresponding to the binding step with a rate-limiting step before it (12). In terms of the slow step, the apparent rate exhibited no significant dependence on the oleic acid concentration, suggesting a uni-molecule reaction. In a previous kinetics study on the ligand binding to human ileal bile acid binding protein, the slow

step whose apparent rate had little dependence on the ligand concentration was considered to be the last conformation exchange step (57). In the study of the dynamics of the human liver FABP, a multi-step model was also proposed: the ligand binding happens after the first conformational change step, followed by the last step of the conformational exchange (26). Based on the knowledge, the stopped-flow traces were globally fitted to the following model by software Dynafit to extract the forward and reverse rates of each step:

$$FABP_{cl} \leftrightarrow FABP_{op} \ (Step\ 1)$$

$$FABP_{op} + L \leftrightarrow FABP_{op}L \ (Step\ 2)$$

$$FABP_{op}L \leftrightarrow FABP_{cl}L \ (Step\ 3)$$

(Model I)

$FABP_{cl}$ refers to the major form of hiFABP inaccessible to the ligand, which exchange with the minor form $FABP_{op}$. The form $FABP_{op}$ is a ligand accessible form, so the transition in Step 1 is a process of 'opening' the portal. This process should be the rate-limiting step. Step 2 should be corresponding to the fast step extracted by the double exponential fitting. Step 3 is an allosteric step, of which the reaction rate should be not dependent on the oleic acid concentration. The parameters fitted by Dynafit are listed in Table 3.2. The residuals are shown in Figure 3.9. The forward rate of Step 1, k_1, should be the rate limit of the ligand binding (plateau). As listed in Table 3.2, the k_1 of the wild type hiFABP was ~1000 s^{-1}, similar to the measurement done by Cistola's group (12). The k_1 of the mutant with the intra-molecule disulfide bond was ~300 s^{-1}, while for the reduced form of the mutant k_1 was ~600 s^{-1}.

	k1 (s^{-1})	k-1/k1	k2 ($uM^{-1}s^{-1}$)	k-2 (s^{-1})	k3 (s^{-1})	k-3/k3	Δ F1	Δ F2	Δ F3
wt hiFABP	1055.6±6.3	50	4576.8±71.9	37.5±1.3	25.8±0.83	0.01	0	0.63±0.006	0.64±0.006
K27C/D74C	238.6±0.78	50	2768.2±39.84	42.6±1.30	8.1±0.11	0.01	0	0.55±0.001	0.63±0.001

disulfide bond									
K27C/D74C	589.3±4.00	50	3816.7±52.64	7.5±1.41	12.3±0.21	0.01	0	0.26±0.002	0.30±0.002
Reduced									

Table 3.2. *The parameters fitted by Dynafit. The unit of k1, k-2, k3 is s^{-1}, and the unit of k2 is $\mu M^{-1}s^{-1}$. k1/k-1 and k3/k-3 refer to the ratio of k1 to k-1 and k3 to k-3 respectively. The parameters, ΔF1, ΔF2 and ΔF3, refer to the fluorescence response of 1μM protein.*

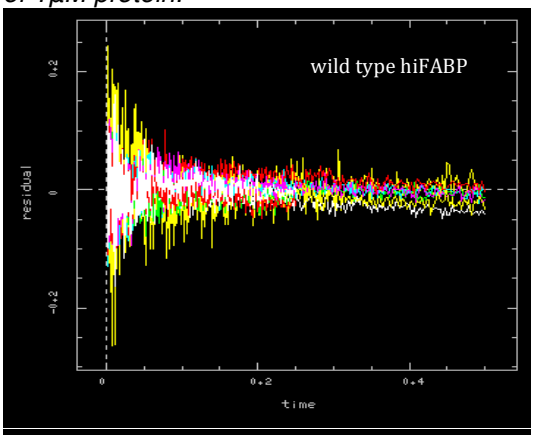

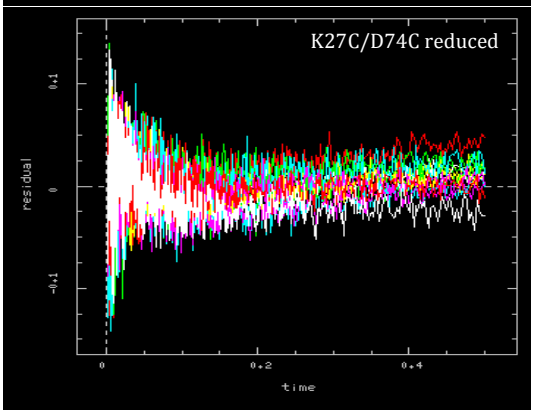

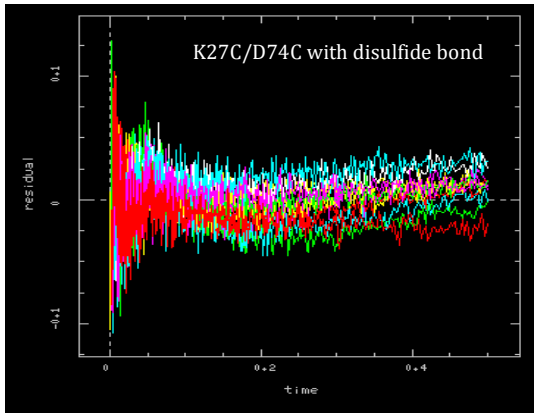

Figure 3.9. *The fitting residuals generated by Dynafit. The stopped-flow traces were loaded fitting, assuming that the association reaction follows Model I. The residues of all the traced are included.*

The deletion of the first allosteric step or the last allosteric step failed to fit the stopped-flow traces, verifying that the two allosteric steps were essential. The results of fitting to the models without the first step or the last step are demonstrated in Figure 3.10.

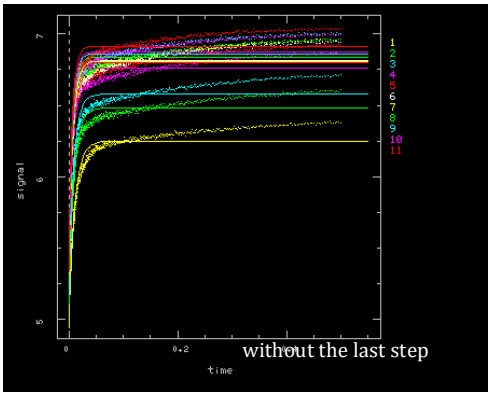

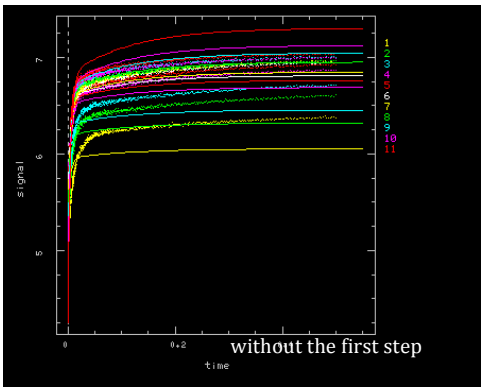

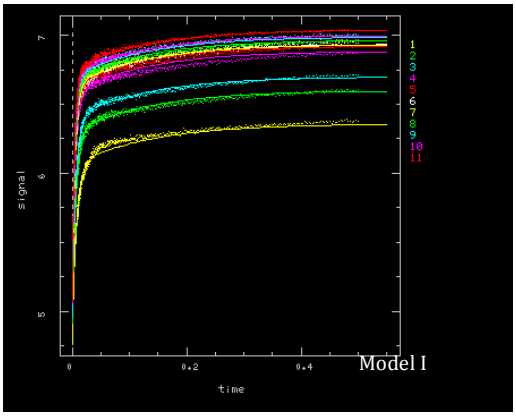

Figure 3.10. *Results of fitting by Dynafit using the model without the first step (right) and the last step (left). The bottom graph displays the fitting result using Model I. For all these three figures, the fitting is based on the stopped-flow traces of the variant K27C/D74C with disulfide bond.*

The k1, the forward reaction rate of the first step, determined by Dynafit was close to the plateau of the fast apparent rate obtained by least square fitting to the double exponential function. The ratios k_{-1}/k_1 and k_{-3}/k_3 were fixed by estimation based on the previous relaxation dispersion analysis when analyzed by Dynafit (26, 59). Early studies on liver and intestinal FABPs also indicated that the 'opening process' or step 1 should be faster than 10^4 s^{-1}, namely the reverse rate k_{-1} should be more than 10 times of k_1 (26). According to the k_1 values, the total exchange rate of the first step (k_1+k_{-1}) was ~50000 $s^{-1}$for wild type hiFABP, while the one of the mutant with the disulfide bond was much slower, only ~12500 s^{-1}.

In terms of Step 2, this ligand-binding step occurred at a rate close to the diffusion control limit which is ~10^{10} $M^{-1}s^{-1}$ for all the three groups, indicating a very small energy barrier. There was a difference in the forward rate of Step 2, k_2, among the three groups. The k_2 value for wild type hiFABP was the fastest, ~4.5×10^9 $M^{-1}s^{-1}$, while the k_2 of the reduced mutant was ~3.8×10^9 $M^{-1}s^{-1}$ and the one of the mutant with the disulfide bond was even slower (Table 3.2). This result suggested that the limitation of the disulfide bond also impaired the rate of step 2.

The rate of the last allosteric step of the variant with disulfide bond was still the slowest in these three groups, suggesting that the helical portal region should also play a significant role in the last conformational exchange. As shown in the Table 3.2, the values of the reverse rate k_{-3} were slower than 0.3 s^{-1} for all the three groups. Although this rate was not accurate because the ratio k_{-3}/k_3 was estimated, it provided us with a rough idea about the timescale of the last step. Figure 3.8 displays the trace of mixing of the ligand-bound variant with buffer, in which there was no significant decaying with the corresponding amplitude observed. This result demonstrated that the dissociation of bound oleic acid should be limited by one extremely slow process, confirming the existence of the last allosteric step.

3.1.6. Structure of the mutant K27C/D74C with the intra-molecule disulfide bond

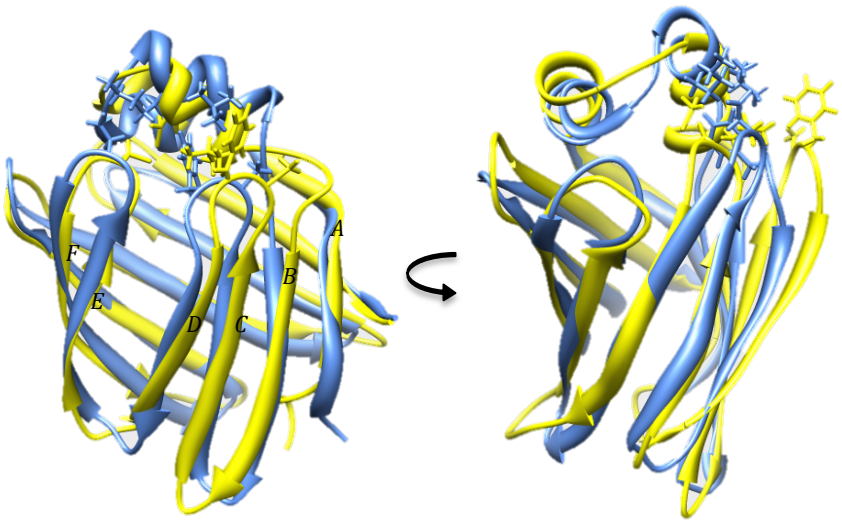

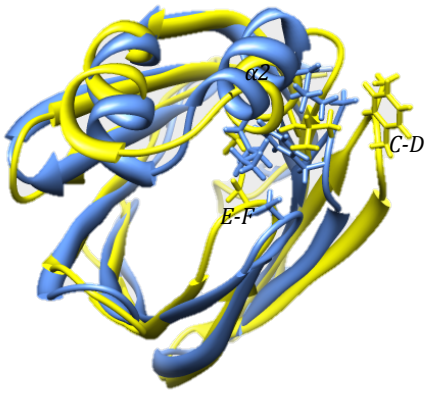

Figure 3.11. *Superimpose of the structures of wild type hiFABP (light blue) and the form with the intra-molecule disulfide bond of K27C/D74C (yellow). The side chains of the residues in the portal region are shown, including residue 27, 30, 54, 55 and 74. The bottom figure shows the view on the portal region from the top.*

The structure of the mutant with the intra-molecule disulfide bond was determined based on 4D ^{15}N,^{13}C-edited NOESY, 3D HNCA, HNCOCA, and TOCSY, 2D ^{15}N-HSQC and ^{13}C-HSQC. The comparison with wild type hiFABP (PDB ID: 3IFB) is shown in Figure 3.11. The mutant retained the basic structure as expected, with some difference in the two helices and strands A-D. The structure alignment with the wild type hiFABP shows a RMSD of 1.12 Å, covering 90 amino acids, excluding the two helices and the strand C and D. Due to the intra-molecule disulfide bond, the second α helix was pulled closer to the barrel, and the turn E-F bended towards the inside of the barrel. The strands A-D were forced to bend out. The side chains of F55 and A54 in the turn C-D were oriented more outside as shown in Figure 3.11. Nevertheless, the interactions between the second helix and turn C-D were still retained. The distance between the Cβ of F55 and L30 was closer than the wild type hiFABP by 1.3 Å, while the distance between the Cβ of A54 and L30 became longer by 1.2 Å. The turn E-F was oriented towards inside, and became closer to the second helix. The Cβ of A73 in the turn E-F was 6 Å away from the Cβ of L30, closer than the wild type hiFABP by ~4 Å. In spite of

these difference caused by the intra-molecule disulfide bond, the overall structure was similar to wild type hiFABP.

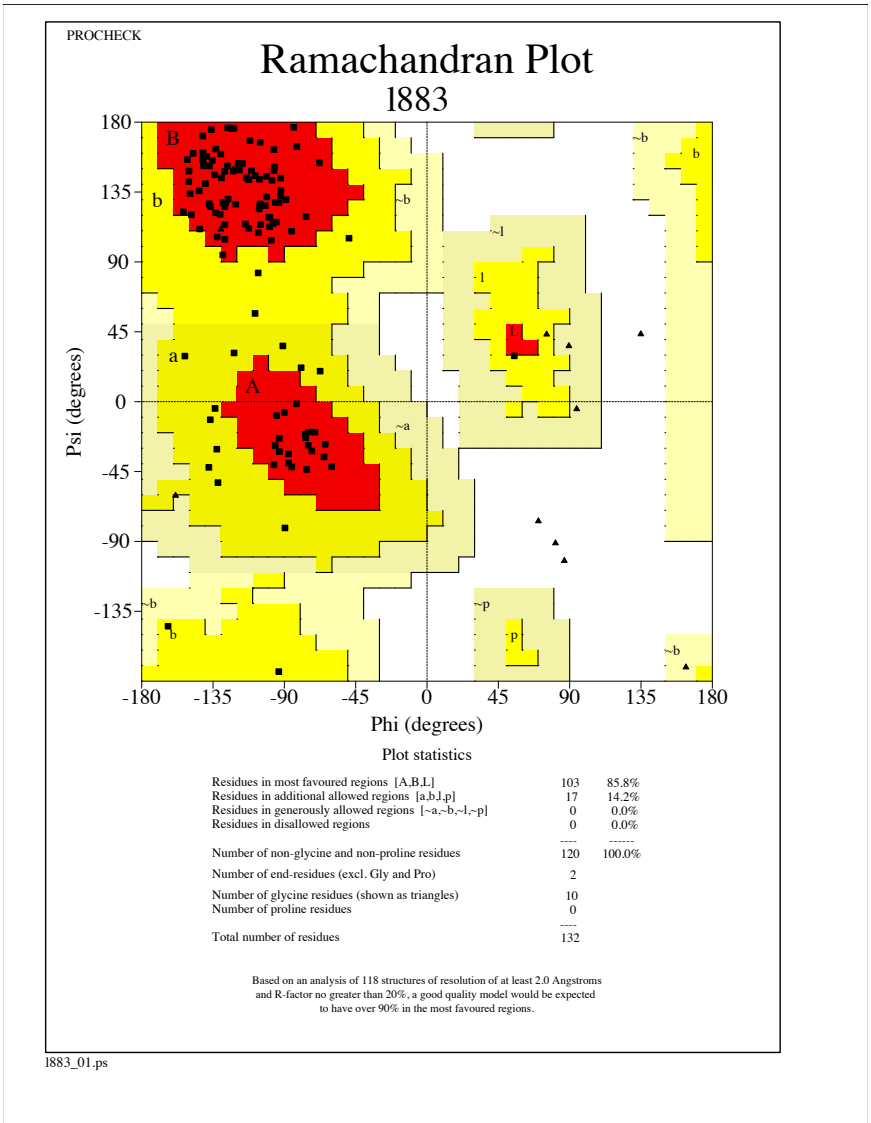

Figure 3.12 *Ramachandran Plot of the structure of the variant K27C/D74C (with disulfide bond) generated by CNS solve 1.3. The plot was created by online server, PDBsum.*
*(*https://www.ebi.ac.uk/thornton-srv/databases/pdb*sum/Generate.html)*

3.1.7. Local unfolding of helical portal region and oleic acid entry

NMR relaxation dispersion has been commonly used for the studies of functionally relevant dynamics of proteins. CPMG relaxation dispersion analysis is suitable to measure the conformational exchange with a rate of ~10^3 s^{-1} (60). Unfortunately, for wild type hiFABP the conformational

exchange between the closed and the opened forms was too fast to be detected by CPMG relaxation dispersion. According to the estimation based on the stopped-flow experiment, the forward rate k_1 of the conformational exchange (Step 1) should be around 1000 s^{-1}, and the total k_{ex} should be ~10^5 s^{-1}. The mutant K27C/D74C with the intra-molecule disulfide bond exhibited much slower k_1 and k_{ex}. This made it possible to capture this conformational exchange by CPMG relaxation dispersion. The protein was expressed in the M9 medium containing 100% D_2O, so that the side chains were labeled with deuterium, which guaranteed the motion of amide protons detectable. To further slow down the exchange rate to a feasible range, the CPMG experiment was conducted at 13 °C.

Representative ^1H and ^{15}N relaxation dispersion profiles are shown in Figure 3.13. In total, 98 and 97 residues displayed obvious ^1H and ^{15}N relaxation dispersion, respectively. The ^{15}N dispersion profile for each available residue could be fitted nicely to a two-state exchange model (Scheme 1, one major state corresponding to the observed native state N, and one minor state I_1 which is invisible in NMR spectra like HSQC). The ^1H dispersion profiles for most residues could also be fitted to the two-state model, but 21 residues could not be fitted. Since the residues displayed obvious ^{15}N relaxation dispersion are distributed over all the β strands and helices, a global two-state exchange process should exist for iFABP in solution. Combining the ^{15}N dispersion data with the ^1H dispersion profiles that could be fitted to the two-state model, we determined the exchange rate, populations of the two states and the difference in the chemical shifts of ^1H and ^{15}N spins between the minor state and the major state. The exchange rate ($k_{ex} = k_1 + k_{-1}$) was 1072 ± 22 s^{-1}, and the population of the minor state (I)

was 3.53 ± 0.02 %. The derived chemical shift differences between the minor state and the major state are listed in Table 3.3 ($\Delta\delta_1$). This conformational exchange process is similar to what we observed for liver FABP, which has been demonstrated to be irrelevant to the process of ligand entry (26).

^{1}H Relaxation Dispersion

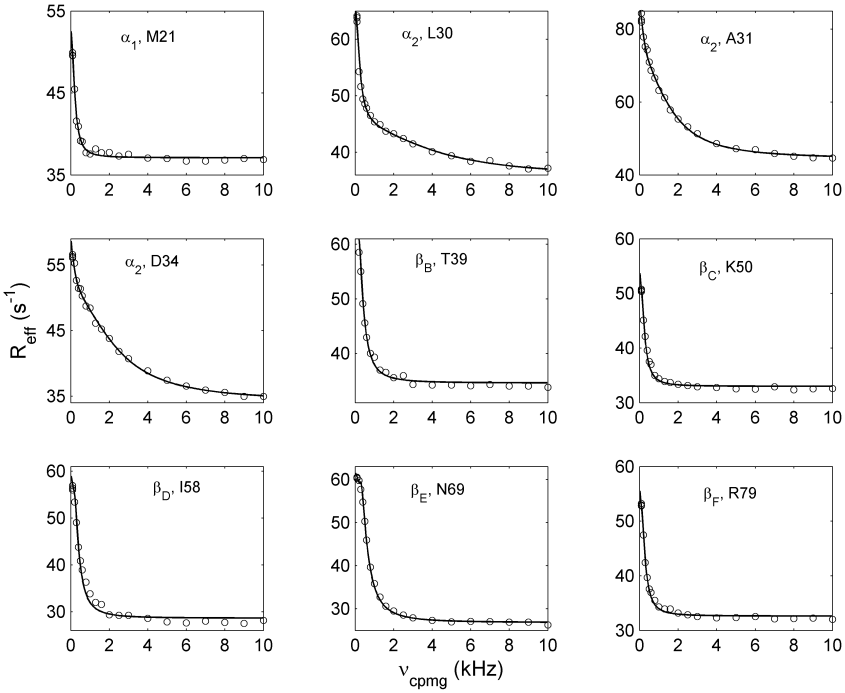

^{15}N Relaxation Dispersion

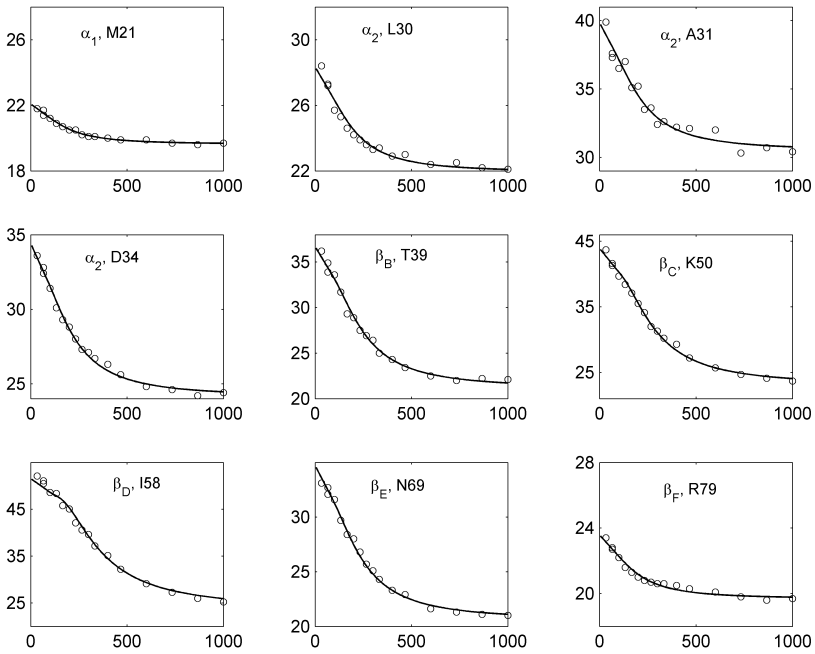

Figure 3.13. *The ^{1}H and ^{15}N relaxation dispersion profiles of K27C/D74C with the disulfide bond. The experiment was done in 13 ^{o}C, pH 7.1. The ^{1}H profiles of the residues in the second helix, like L30, A31 and D34, are fitted with three-state model. The rest of the ^{1}H and all the ^{15}N profiles shown in this figure are fitted to the two-state model.*

	H chemical shift				N chemical shift		
Residue	δ_H	$\Delta\delta_1$	$\Delta\delta_2$	δ_N-δ_U	δ_N	$\Delta\delta_1$	δ_N-δ_U
A1	8.356	0.093		-0.094	122.88	0.87	-2.685
F2	8.423	0.092		0.093	113.25	0.88	-6.56
D3	7.544	0.068		-0.806	119.22	0.78	-3.335
S4	8.264	0.137		-0.234	120.88	1.15	3.446
T5	8.096	0.1		-0.343	115.94	1.29	0.544
W6	9.567	0.116		1.496	128.62	0.91	5.119
K7	10.011	0.202		1.808	123.38	1.64	-1.086
V8	8.889	0.21	0.48	0.663	128.71	1.79	6.927
D9	9.797	0.276		1.219	128.09	1.65	3.377
R10	7.83	0.143		-0.688	112.61	1.06	-10.092
S11	8.704	0.518		0.089	113.63	2.1	-3.969
E12	9.534	0.243		0.929	122.7	1.78	0.041
N13	8.466	0.792		-0.029	120.96	2.47	1.405
Y14	8.639	0.22	0.93	0.361	118.16	1.64	-3.31
K16	7.726	0.237		-0.52	119.68	2.17	-2.074
F17	7.655	0.161		-0.749	121.57	0.72	0.734
M18	7.957	0.19	0.22	-0.247	118.11	1.17	-3.673
E19	8.378	0.33	0.45	-0.072	119.88	0.61	-2.902
K20	8.158	0.096		-0.393			
M21	7.596	0.184		-0.98	114.82	0.57	-7.011

G22					108.01	0.83	-2.488
V23	7.025	0.12	0.59	-1.112	116.8	1.56	-2.034
N24	8.568	0.153		-0.126	123.61	1.84	0.889
I25					122.4	0.66	0.91*
V26	7.655	0.161		-0.789	121.57	0.72	-3.402
C27	7.73	0.08	0.24	-1.075*	118.46	1.13	-5.38*
R28	8.295	0.25	0.38	-0.35*	117.78	1.03	-7.01*
K29	7.794	0.2	0.97	-0.771*	117.92	0.88	-5.27*
L30	7.36	0.23	0.6	-1.025*	119.38	0.97	-4.13*
A31	8.408	0.22	1.05	0.023*	120.73	1.23	-4.34*
A32	7.557	0.42	1.01	-0.892	115.95	1.92	-7.766
D34	7.396	0.12	0.84	-0.986	118.74	1.3	-2.87
L36	6.881	0.24	0.57	-1.47	119.47	2.85	-2.851
K37	9.144	0.36	0.77	0.701	125.93	2.64	3.451
L38	9.4	0.133		0.953	122.9	3.64	-1.12
T39	9.263	0.432		0.773	120.99	1.77	4.339
I40	8.554	0.09		0.092	128.49	1.73	4.49
T41	8.614	0.123		0.159*	121	1.12	2.53*
Q42	9.323	0.145		0.691	128.3	1.41	5.257
E43	8.849	0.097		0.206	128.57	0.62	6.111
N45					125.22	0.49	6.198
F47	9.045	0.097		0.615	126.28	1	5.435
T48	8.326	0.111		0.028	115.72	0.93	-1.13
V49	9.595	0.255		1.18	127.6	1.07	4.156
K50	9.21	0.241		0.585	128.31	2.32	2.327
E51	9.147	0.315		0.464	126.79	1.76	3.655
S52	9.079	0.104		0.475	120.01	2.88	2.715
S53	8.978	0.26	1.03	0.411	121.62	2.6	3.349
A54	9.183	0.19	0.43	0.808	120.18	1.6	-5.523
R56					114.99	4.4	-7.876
I58	8.734	0.431		0.43	117.94	3.43	-3.355
E59	8.668	0.582		0.081	124.32	4.9	-0.823
V60	9.117	0.088		0.791	128.05	0.42	5.563
V61	8.234	0.16		-0.083	125.76	4.27	0.897
F62	8.372	0.329		-0.201	121.53	0.68	-3.662
L64	8.908	0.092		0.473*	125.03	0.65	1.6*
G65	9.236	0.095		0.641			
V66	7.956	0.16		-0.086	122.55	0.59	3.492
T67					129.66	0.64	12.22
F68	9.709	0.17		1.244*			
N69	8.401	0.7		-0.124*	116.81	1.63	-4.04*
Y70	8.834	0.245		0.529*	121.41	1.96	0.37*
N71	8.045	0.499		-0.526			
L72	8.226	0.27	0.64	0.116	122.72	2.05	0.435
G75	7.943	0.31	1.45	-0.639	106.2	1.29	-6.453
T76	7.344	0.36	0.95	-0.91	117.59	1.87	4.033

E77	8.404	0.12	0.9	-0.333	128.54	0.91	4.771
L78	8.958	0.09	0.34	0.452	126.62	0.83	2.344
R79	8.686	0.271		0.026	119.17	0.73	-3.706
G80	9.141	0.092		0.592	116.48	0.66	6.271
T81	6.969	0.086		-1.25			
W82	9.103	0.097		0.778	119.49	0.96	-4.018
L84	9.018	0.082		0.593			
E85					127.56	0.56	6.519
K88					118.41	0.62	-3.539
L89	8.679	0.162		0.314*	123.26	0.81	-0.09*
G91	9.683	0.102		1.115			
K92	7.84	0.099		-0.454	128.76	0.47	7.465
K94	8.799	0.093		0.255			
T96	8.276	0.221		-0.336	116.14	1.47	0.593
D97	8.937	0.169		0.367	121.13	0.92	-1.556
N98	8.751	0.147		0.124	117.11	0.53	-2.264
G99	7.667	0.116		-0.98	107.49	0.53	-1.862
E101					120.02	0.57	-1.469
T104	9.022	0.114		0.783	118.7	0.51	3.902
V105	8.13	0.16		-0.216			
E107	8.661	0.186		0.006*	120.94	1.19	-1.9*
I108	8.767	0.12		0.24	124.47	0.64	0.605
I109	8.99	0.099		0.407	130.21	0.43	3.321
G110					119.54	0.6	5.854
D111	8.744	0.132		0.338			
E112					118.69	0.41	-2.533
L113	7.906	0.182		-0.547	123.76	0.52	0.316
V114	9.388	0.114		1.065	128.04	0.58	5.641
Q115	9.643	0.128		0.99	130.51	0.69	5.508
T116	8.879	0.139		0.524	121.77	0.91	5.287
Y117	9.581	0.191		1.141	125.99	1.33	2.537
V118	8.98	0.127		0.731	119.72	0.89	-3.879
E120	9.515	0.082		0.924			
V122	8.371	0.078		0.221			
E123	8.562	0.162		-0.13			
A124	9.223	0.159		0.792	125.99	1.26	0.128
K125	8.91	0.234		0.488	116.44	1.55	-4.711
R126	9.399	0.195		0.832	120.11	1.01	-3.433
I127	8.822	0.219		0.427	123.3	0.76	0.115
F128	10.108	0.13		1.472	126.55	0.48	0.576
K129	8.845	0.324		0.298	118.48	0.81	-6.398
K130					123.46	1.01	-1.409

Table 3.3. *The chemical shifts of the major and minor states of all the residues extracted from the relaxation dispersion and the chemical shift difference of the native protein and the unfolded protein. *The chemical shifts of the unfolded protein are obtained based on the assignment of the protein in 8M urea and the prediction by the online software (http://nmr.chem.rug.nl/ncIDP/).*

In order to determine if the minor state is a folded or unfolded or intermediate form, the chemical shift differences between states N and I were compared with the difference between state N and the unfolded variant K27C/D74C. We determined the chemical shifts of ^{1}HN and ^{15}N spins in the presence of 8 M urea under which the protein was denatured. The chemical shift differences are listed in Table 3.3 (δ_N-δ_U). The residues around C27 (C27-A31) were not observable in the 1H-15N HSQC in 8 M urea at 13 °C due to conformational exchanges for those residues on ms-μs timescales, indicating the disulfide bond also slowed down the conformational exchanges of unfolded forms. The chemical shifts obtained from the sample in 8 M urea exhibited a good correlation with the predicted ones (Figure 3.14) after corrections by adding 0.33 ppm and 0.175 ppm to the predicted ^{15}N and ^{1}H chemical shifts, respectively. So for the residues without experimental data, the predicted shifts were used in the analysis of the structure of minor states. Comparing the chemical shift differences of the minor state and denatured state, we found that the minor state was totally different from an unfolded state. In fact, the minor and major states had similar chemical shifts for most residues. Therefore, the minor state should be a native-like intermediate state, which is denoted as I_1 (Scheme 1).

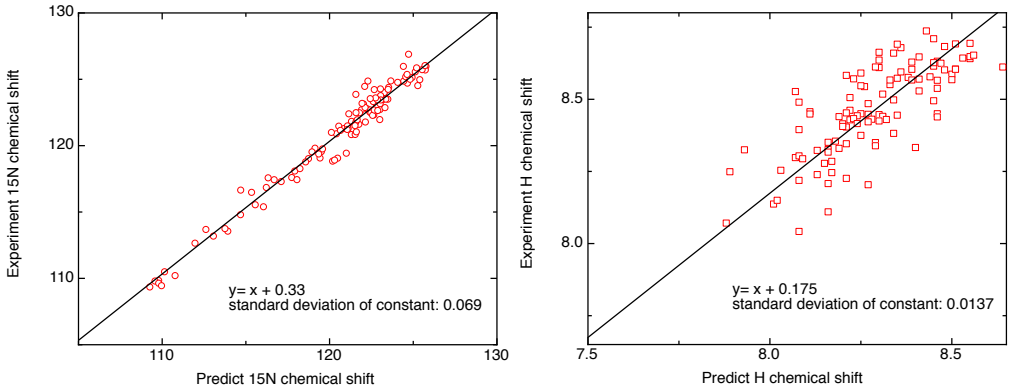

Figure 3.14. *The correlation between the predicted chemical shifts of the denatured protein and the experimental chemical shifts determined by the assignment of the variant K27C/D74C with the disulfide bond denatured by 8M urea.*

As mentioned above, a number of residues displayed quite different ^1H dispersion profiles from other residues. These residues were located in the second helix or proximal to it (Table 3.3, Figure 3.15A). The proximal residues include Y14, M18 and E19 located in the first helix, V23 in the loop between the first and the second helix, L36 and K37 in the loop between the second helix and β stand B, S53 and A54 in β turn C-D, and L72, and G75-L78 in β-turn E-F. For these residues, the ^1H relaxation rates were dependent on the CPMG field strength even when the field strength was larger than 4000 Hz, indicating the presence of another conformational exchange process which is much faster than ~1000 s^{-1}. Therefore, a three-state model (scheme 2) was assumed for the residues of which the ^1H dispersion profiles could not be fitted by a two-state model. In the three-state model, the slower exchange process was considered to be the same as the process derived from the two-state model (Scheme I). Fitting the dispersion profiles to the three-state model, we obtained the exchange rate (k_{ex2}) between the third state (I_2) and major state, the population of state I_2, and the chemical shift differences of ^1H spins between state I_2 and major state N. The exchange rate ($k_{ex2}=k_2 + k_{-2}$) was 13382 ± 512 s^{-1}, while the population of I_2 (p_2) was 1.45 ± 0.06 %. According to this result, the rate from the major native state with a closed conformation to state I_2 should be 194 s^{-1} ($k_{ex2}*p_2$).

$$N \Leftrightarrow I$$

Scheme 1

$$I_1 \Leftrightarrow N \Leftrightarrow I_2$$

Scheme 2

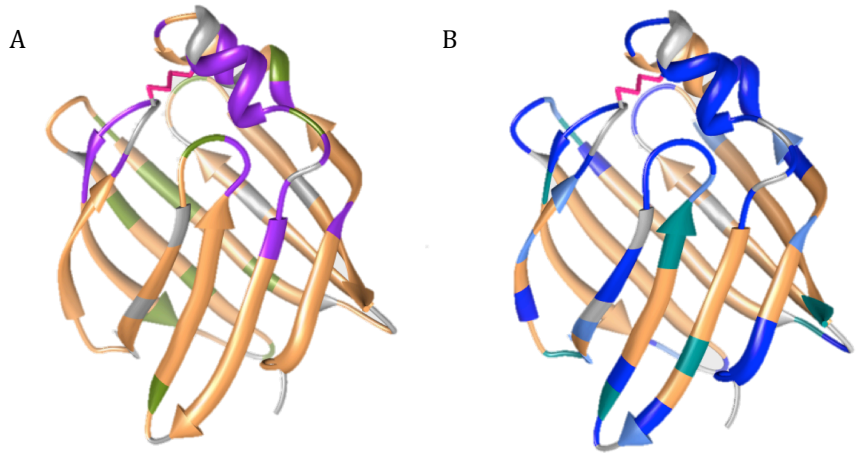

Figure 3.15. A. *The residues with three-state exchange are colored in purple. The residue in green are those without observable chemical exchange. The rest residues experience the two-state exchange.* ***B.*** *The protection factor of the mutant K27C/D74C in the presence of the intra-molecule disulfide bond. The different colors are corresponding to the different protection factor: yellow, cannot observe obvious exchange between the proton and deuterium; gray, the residues whose resonance peaks are very weak or missing; blue, protection factor < 100; light blue, 100< protection factor < 1000; cyan, 1000< protection factor < 10000; sandy brown, protection factor >10000.*

To verify whether the exchange process that these 21 residues experienced was the one between the closed and the opened forms, stopped-flow experiment was conducted in 13 °C. The apparent rates of oleic acid association in 13 °C are shown in the Figure 3.16. Similar to the experiment in 20 °C, there was a plateau of the fast apparent rate. The value of the plateau should be equal to the forward rate of the conformational exchange (Step 1), or the rate from the closed form to the opened form. At 13 °C, this rate was estimated to be ~180 s^{-1}. The rate constants determined by Dynafit are listed in Table 3.4. This rate was comparable to the forward rate from N to I_2, which was 194 s^{-1}. Thus, it is reasonable to postulate that the conformational exchange between N and I_2 states should correspond to the rate-limiting step (Step 1) in model I.

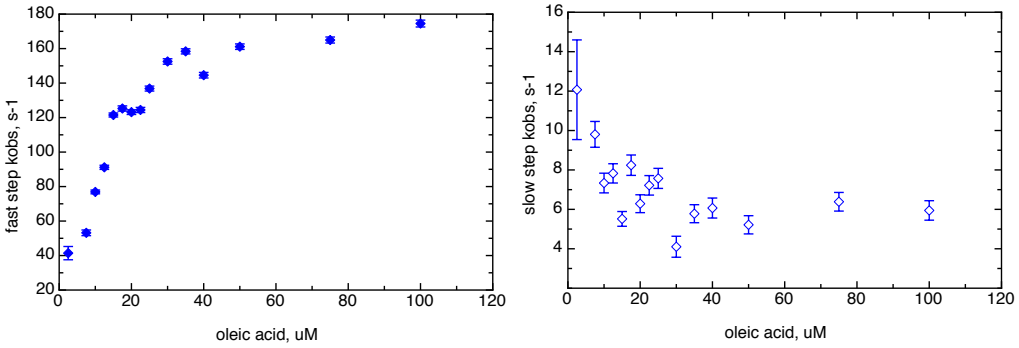

Figure 3.16. *The apparent reaction rates of the two phases extracted from the stopped-flow traces in 13 °C. The oleic acid in varied concentration reacted with the mutant with the disulfide bond (3uM). The left graph shows the apparent reaction rate of the fast step of the oleic acid binding with the mutant, K27C/D74C with the intra-molecule disulfide. The right graph shows the apparent reaction rate of the slow step of the oleic acid binding with the mutant, K27C/D74C with the intra-molecule disulfide bond.*

	k1 (s^{-1})	k-1/k1	k2 ($uM^{-1}s^{-1}$)	k-2 (s^{-1})	k3 (s^{-1})	k-3/k3	ΔF1	ΔF2	ΔF3
K27C/D74C with S-S	187.5± 0.73	80	1336.8 ±13.90	13.5± 0.44	6.3± 0.15	0.01	0	0.40± 0.001	0.45± 0.001

Table 3.4. *The parameters of the stopped-flow experiment done in 13 °C fitted by Dynafit. The unit of k1, k-2, k3 is s^{-1}, and the unit of k2 is $\mu M^{-1}s^{-1}$. k1/k-1 and k3/k-3 refer to the ratio of k1 to k-1 and k3 to k-3 respectively. The parameters, ΔF1, ΔF2 and ΔF3, refer to the fluorescence response of 1μM protein.*

To further characterize the structure of state I_2, the chemical shift differences between states N and I_2 ($\Delta\delta_2$) were compared with those between state N and the unfolded protein at 8 M urea (δ_N-δ_U) (Table 3.3). Although the sign of $\Delta\delta_2$ was undetermined, the $\Delta\delta_2$ values were quite close to the absolute δ_N-δ_U values for most residues in the second helix such as R28, K29, L30, A32 and D34, implying that this helix should be mainly unfolded in state I_2. On the other hand, most residues in the first helix and nearly all the residues in all β-strands did not exhibit the third state I_2. Therefore, state I_2 very likely adopts a locally unfolded conformation in which only the second helix is mainly unfolded. Due to the unfolding of the second helix, the residues close to this helix in space could be altered in chemical environments, and thus their chemical shifts in state I_2 are different from those in the native state (N). This explains why the residues proximal to the second helix displayed the three-state dispersion profiles.

To further study the structure of intermediate states, we measured amide hydrogen exchange rates and calculated the protection factors, as mentioned in the Materials and Methods, for the mutant with the disulfide bond. The data revealed that the residues in the second helix was very different from the first helix (Figure 3.15B, Page 58) although the solvent accessible area (SAS) and the pattern of the hydrogen bonds in the second helix were very similar to those in the first helix. The residues in the second helix had much smaller protection factors than the first helix and the strands. The protection factors of the amide protons in the second helix were below 100, some of which were even smaller than 10. The amide protons in the first helix and the β strands did not exhibit observable proton exchange, of which the protection factors were estimated larger than 10000. Figure 3.15B demonstrates that the residues with the similar protection factors to the second helix are mostly located in the turns. The result supports that only the second helix experiences the local unfolding in state I_2 while state I_1 is structured.

3.1.8. Effect of single point mutation

The relaxation dispersion studies on the mutant with a disulfide bond as mentioned above clarified the close relation between the ligand entry process and the local opening of the second helix. Interestingly, the reduced form of the double point mutant K27C/D74C admitted the oleic acid at a significantly slower rate than wild type hiFABP, and the amide proton exchange rates of the reduced mutant also became slower than wild type hiFABP. To further investigate which residue contributed to the decrease in the rate of oleic acid association and the backbone flexibility, two single point mutants, K27C and D74C, were generated.

As shown in Figure 3.17B, there was a subtle difference between D74C and K27C in terms of the stability against urea denaturation. By fitting the denaturation curves, it was found that the variant D74C had a higher mid point (Cm) value than wild type hiFABP and the variant K27C (Table 3.5), suggesting the decreased flexibility of the double point mutant should be due to the mutation in D74. The double point mutant K27C/D74C had a similar mid-point (Cm) and m-value to the mutant K27C. The residue K27 is located in the second helix, so the mutation in this residue should exert more impact on the global stability of the double point mutant. The residue D74 is located in the turn between strand E and F, the mutation in this residue should have less impact than K27.

Figure 3.17A and C demonstrate the apparent rates of the fast and slow association steps for the single point mutants. The plateau of the fast step for D74C was 600 s^{-1}, which was ~55% of the plateau value of wild type hiFABP, almost the same as that for the reduced form of the variant K27C/D74C. On the other hand, K27C had a ~10% smaller plateau value than wild type hiFABP, indicating a less important effect than the mutant K27C on ligand entry. The result suggested that the decreased oleic acid association rate of the reduced form of K27C/D74C should arise from the mutation in D74. A previous study has found that the D74A mutant exhibited a slower association rate but faster dissociation rate than the wild type protein (61). Moreover, a similar mutagenesis study found a decreased binding affinity caused by the mutation D74A of iFABP (62). The effect of D74C on ligand binding might be related to the negative charge of residue D74. To identify the role played by D74, reversed charged mutation could be generated to examine its effect on ligand association in the future.

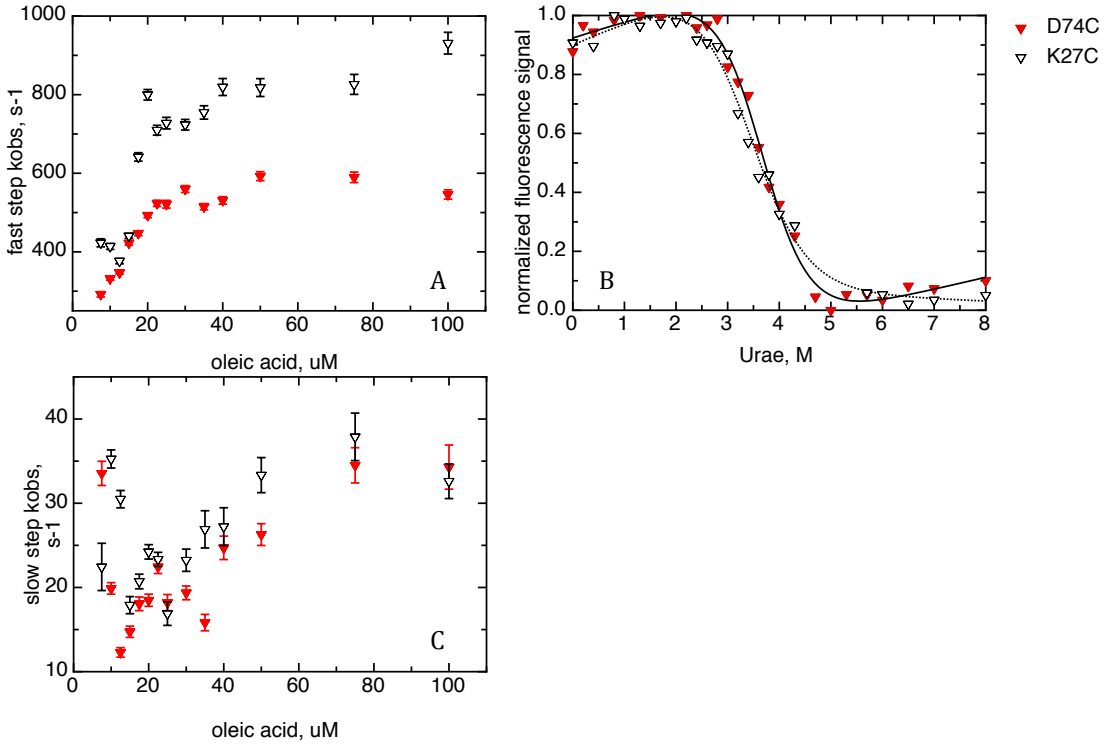

Figure 3.17. *The chemical stability and the apparent rates of the two single point mutants, K27C and D74C. The red triangle stands for the mutant D74C, while the empty triangle stands for the mutant K27C. Figure A and C exhibit the dependence of the apparent rates of the fast step and the slow step on the oleic acid concentration. The final protein concentration in the stopped-flow experiment was 3uM (D74C) or 5uM (K27C). Figure B shows the urea denaturation curve. The protein concentration in the denaturing experiment was 4 μM.*

	m-value (kJ/mol/M)	mid point (M)	ΔG^0 (kJ/mol)
wild type hiFABP	5.50±0.815	3.11±0.088	17.11±0.151
K27C/D74C with DTT treatment	4.75±0.523	3.32±0.070	15.76±0.112
K27C	4.68±0.603	3.37±0.097	15.77±0.132
D74C	5.35±0.510	3.66±0.054	19.58±0.096

Table 3.5. *The parameters extracted from the urea denaturation curves of the variants K27C and D74C. The experiment was conducted in room temperature. The pH of the buffer is 7.1. The protein concentration was 4uM.*

	k1 (s-1)	k-1/k1	k2 (uM-1s-1)	k-2 (s-1)	k3 (s-1)	k-3/k3	ΔF1	ΔF2	ΔF3
K27C	923.4±5.06	50	4250.4±59.62	43.6±1.19	27.5±0.51	0.01	0	0.45±0.004	0.47±0.004
D74C	603.3±2.53	50	5269.7±53.50	31.6±1.01	22.4±0.30	0.01	0	0.58±0.003	0.62±0.003

Table 3.6. *The parameters fitted by Dynafit for the two single mutants K27C and D74C. The unit of k1, k-2, k3 is s^{-1}, and the unit of k2 is $\mu M^{-1}s^{-1}$. k1/k-1 and k3/k-3 refer to the ratio of k1 to k-1 and k3 to k-3 respectively. The parameters, ΔF1, ΔF2 and ΔF3, refer to the fluorescence response of 1μM protein.*

3.2. Discussion

Our structure, dynamics, and kinetics studies on hiFABP mutant K27C/D74C clarified the mechanism underlying oleic acid incorporation into the binding cavity of human intestinal fatty acid binding protein (hiFABP). The intra-molecule disulfide bond between C27 and C74 in the helical portal region exerted an impact on the motion of the helical portal region, resulting in a significantly reduced ligand association rate. We draw the following conclusions: 1. the ligand binding is a three-step reaction process; 2. the ligand should enter through the second helix after the local unfolding, like a 'lid-opening' process; 3. The binding rate is limited by the local unfolding of the second helix with an exchange rate of $\sim 1.5\times10^{4}$ s^{-1} for the variant K27C/D74C with the disulfide bond.

To investigate the effect of the intra-molecule disulfide bond on the backbone flexibility, the amide proton exchange rates were measured. The mutant with the disulfide bond exhibited slower exchange rates in the second α helix and the turn E-F than the reduced form (Figure 3.4), suggesting the impaired flexibility. The higher stability of the second helix and turn E-F resulted in the decreased apparent rate of the ligand entry of the oxidized mutant, suggesting the important involvement of the second helix and turn E-F in the process of ligand entry.

Previous dynamics studies and MD simulations have indicated that the helical portal region underwent a conformational exchange before ligand binding (20). This conformational exchange was found to be the rate-limiting step for oleic acid to bind iFABP by D. Cistola (12). However, the description in the early studies was insufficient and inaccurate. In the current study, a rate-limiting step was also found in the process of oleic acid association by

the stopped-flow experiments (Step 1 in Model I), with a forward rate k_1 of ~1000 s^{-1} for wild type hiFABP. This rate was similar to that reported by D. Cistola. In the kinetics study of the iBABP by stopped-flow experiments, the k_1 was estimated to be ~1600 s^{-1} (57). Despite of the similar k_1 values, the value of the reversed rate, k_{-1}, of Step 1 should be much faster than that determined by Cistola (12). In the previous studies the value of k_{-1} was estimated to be ~10^2 s^{-1} based on stopped-flow data, which means the population of $FABP_{op}$ (the ligand accessible form) was more than 75%. If this was the case, the open form would be observable in HSQC spectrum, and the total exchange rate k_{ex} (k_1+k_{-1}) would be around 1000~2000 s^{-1}. However, both NMR and X-ray crystal structures are in the closed form, and the conformational exchange at a rate of ~1000 s^{-1} is a global process for the entire protein instead of the portal region or other local regions (26, 59). This contradiction indicated that the open form should exist in a minor and 'invisible' form and the conformational exchange should happen on a much faster timescale. In terms of Step 2 (Model I), the forward rate k_2 values for all the three variants were close to the diffusion control limit, implying a very small energy barrier. This result indicated that the state $FABP_{op}$ (Model I) should be an unstable 'open' state, which was also supported by results from the NMR relaxation dispersion data.

Relaxation dispersion is a powerful tool to study functionally relevant dynamics, like folding/unfolding, ligand binding and structure rearrangement (63, 64). The accessible range is on the millisecond – microsecond timescales. In the case of wild type hiFABP, unfortunately, the functionally relevant conformational exchange seems too fast to be studied by CPMG-based dispersion experiments. Nevertheless, the mutant K27C/D74C with the

intra-molecule disulfide bond possesses a much slower exchange rate, allowing characterization of the fast conformational exchange by CPMG relaxation dispersion. From the relaxation dispersion profiles, we have found that the portal region experienced two different conformational exchanges as shown in Scheme 2. The transition between the native state N and minor state I_2 occurred at a rate of ~14000 s^{-1}, and the population of the minor state was 1.45%. This transition was exclusive to the residues located in the portal region. The forward rate of this transition (from N to I_2) was consistent with the forward rate of Step 1 obtained in stopped-flow study, confirming that the transition between N and I_2 should be relevant to ligand binding. The ^1H chemical shift differences of state I_2 exhibited a correlation with the unfolded state for the residues in the second helix, suggesting the state I_2 might adopt a locally unfolded conformation in the second helix. The protection factors of the second helix also suggested that the second helix should experience a process of unfolding, otherwise the proton rates should not be even faster than the residues in unstructured region (Figure 3.15B). Therefore, we conclude that the process of local unfolding in the second helix should be the conformational exchange between the closed and the opened forms (Step 1), which allows ligand entry. Although the conclusion was drawn from the studies on the mutant, wild type hiFABP should adopt the same mechanism but the rate of the local unfolding must be much faster.

The rate of the last allosteric step (Step 3) was also slowed down by the intra-molecule disulfide bond, suggesting a critical role of the second α helix in the release of oleic acid. Previous studies hinted that oleic acid might be delivered to the membrane through the helices. The two helices have been found to determine the mechanism of the ligand delivery based on the

comparison of the releasing process between liver FABP and iFABP (65, 66). The chimeric protein with the helical domain of the iFABP and the β barrel of the liver FABP showed a collisional transfer mechanism similar to wild type iFABP (65). The collisional transfer was initialized with the collision between the two α helices and membrane, followed by the release of the ligand to the membrane (65). MD simulation studies have also indicated a collisional transfer mechanism through the helical portal region (29).

In our study, the trial to measure the oleic acid dissociation rate by mixing the ligand-bound protein with buffer failed. There was no observable decaying with the amplitude corresponding to the signal increase upon ligand binding (Figure 3.8). The early studies reported the apparent rate of ligand transfer previously around 1 s^{-1}, in which the oleic acid dissociation happened in the presence of the modeled membrane (38, 39, 61). The membrane-helices interaction may adjust the equilibrium of the last allosteric reaction (Step 3) to let the oleic acid be released to the membrane. The ESR study on brain FABP indicated that the C terminus of the second α helix should be the sensor for different membranes and become more flexible in the presence of the modeled membrane (67). The presence of the membrane may alter the dynamics of the second helix, starting the delivery of fatty acid.

To summarize, the studies on the mutant K27C/D74C elucidated the mechanism of ligand entry: the second helix experiences the process of local unfolding, and hiFABP transits to the ligand accessible state (or opened state), allowing the ligand to enter and then to bind to the binding pocket.

Chapter 4. Variant V26H/L30H with HxxxH motif

4.1. Result

4.1.1. Mutant V26H/L30H capable of binding metal ion

To further confirm the essential role of the second helix in ligand entry, another mutant was generated. The mutant V26H/L30H with two histidine residues in the second helix contained an HxxxH motif. Previous studies have shown the capability of the HxxxH motif in a helix to bind the metal ions like Ni^{2+}or Cu^{2+} with the assistance of NTA (27, 68). The two residues are highlighted in the Figure 4.1. The rationale of using this mutant was that the binding of metal ions to the helix should stabilize the second α helix due to the coordination of the metal ions. In this way we could inspect the role of the second α helix in ligand entry from a different angle.

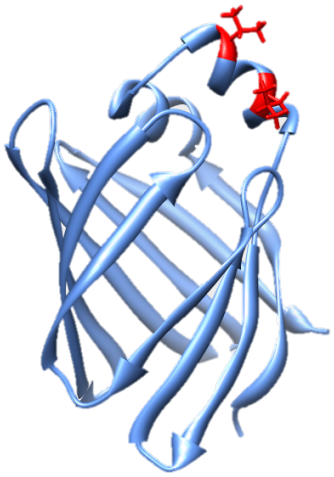

Figure 4.1. *The ribbon representation of the structure of wild type hiFABP (PDB ID: 3IFB). The residues mutated to Histidine are highlighted in red.*

To examine the capability of the mutant V26H/L30H to bind Ni^{2+} or Cu^{2+} conveniently, the cDNA of the mutant was inserted in a pET-M vector, without the purification tag 6×His. In this way, the capability of the protein to bind Ni-NTA affinity column should reflect the binding affinity of the protein with Ni-NTA. Figure 4.2 displays the SDS-PAGE of the mutant purified via Ni-NTA

affinity chromatography. The elution 1~4 contained imidazole at concentrations varying from 50mM to 300mM, and the concentrations of imidazole in Wash 1 and 2 were 5mM and 20mM, respectively. As shown in Figure 4.2, most of the impurities were eluted in Wash 1, and the purity of the elution was estimated to be higher than 90%. Most of the target protein was eluted in the elution containing 100mM imidazole. This result indicated that the binding affinity of the mutant to Ni-NTA was comparable to the fusion protein with a 6×His tag. Knowing the potential of the mutant to bind with the Ni-NTA, we proceeded to the measurement of the binding affinity accurately.

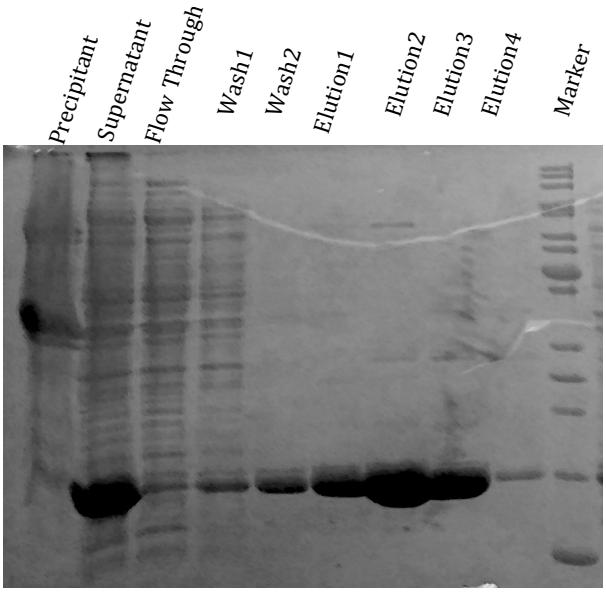

Figure 4.2. *The SDS-PAGE analysis of the mutant V26H/L30H after the Ni-NTA chromatography purification.*

4.1.2. Metal ion binding with the mutant V26H/L30H

The binding affinity of the mutant to Cu-NTA was measured by ITC first. The result is shown in Figure 4.3. The one-site binding model was used for fitting. The dissociation constant was 40uM at pH 7.1. This result suggested a specific binding of the mutant with Cu-NTA. However, the binding affinity was weaker than that previously reported for other proteins (27). To further confirm the binding of the metal ion to the mutant, ^{15}N-HSQC spectra were recorded

in the presence and absence of Ni-NTA. The reason for not using Cu^{2+} was that Cu^{2+} would significantly reduce the NMR signals for residues close to the binding site due to paramagnetic effect.

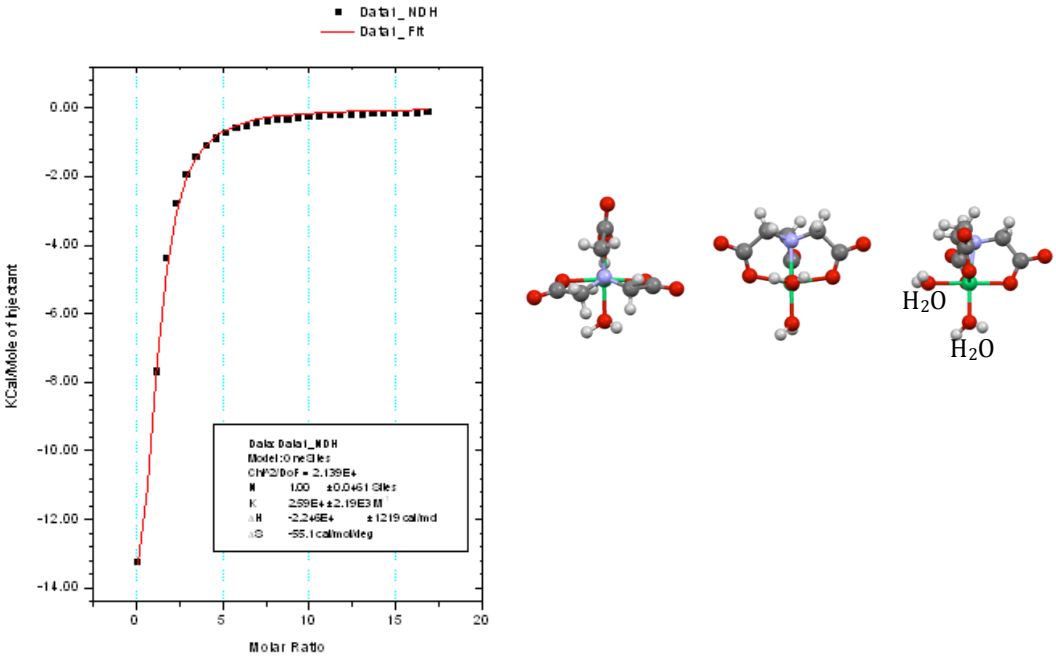

Figure 4.3. *The binding affinity between the variant V26H/L30H and Cu-NTA measured by ITC. The experiment was conducted in 25 ^{O}C. The pH was 7.0, in Tris-HCl buffer (20mM Tris-HCl, 20mM NaCl). The right figure shows three views of the structure of [Ni(NTA)(H2O)2]$^{-}$. The green atom is Ni^{2+}, coordinated with NTA.*

The assignments of the resonance peaks in the ^{15}N-HSQC spectrum were done with the assistance of a ^{15}N-NOESY spectrum and the assignments of wild type hiFABP. Except for the residues near the second helix, most of the rest residues were not affected in chemical shifts by mutation. The comparison of the Ni-NTA free form of V26H/L30H and wild type hiFABP is shown in Figure 4.4A. Besides the change in chemical shifts, the mutation caused the reduction of peak intensities of the residues in the second α helix, implying that the dynamics of the helix was affected by the mutation.

After adding Ni-NTA, the residues near the binding site exhibited obvious change in the chemical shifts of the corresponding peaks. Figure 4.4B shows the HSQC spectra of the Ni^{2+}-free and Ni^{2+}-bound forms of the variant. 20 resonances exhibited significant change in chemical shifts, all of which clustered in and around the second α helix, confirming the binding of Ni-NTA to the HxxxH motif in the second helix. Based on the assignments, the peaks exhibiting significant changes in chemical shifts and/or intensities were identified: Y14, D15, K16, E19-H26, H30-D34, F55, R56, G75 and T76, most of which were in the helical portal region. The residues in the second helix became invisible in the HSQC spectrum in the presence of Ni-NTA, which might be due to the chemical exchange between the Ni-NTA bound and free forms. The disappearance of these peaks impeded the further analysis to figure out the backbone flexibility and the 'lid opening' process by NMR.

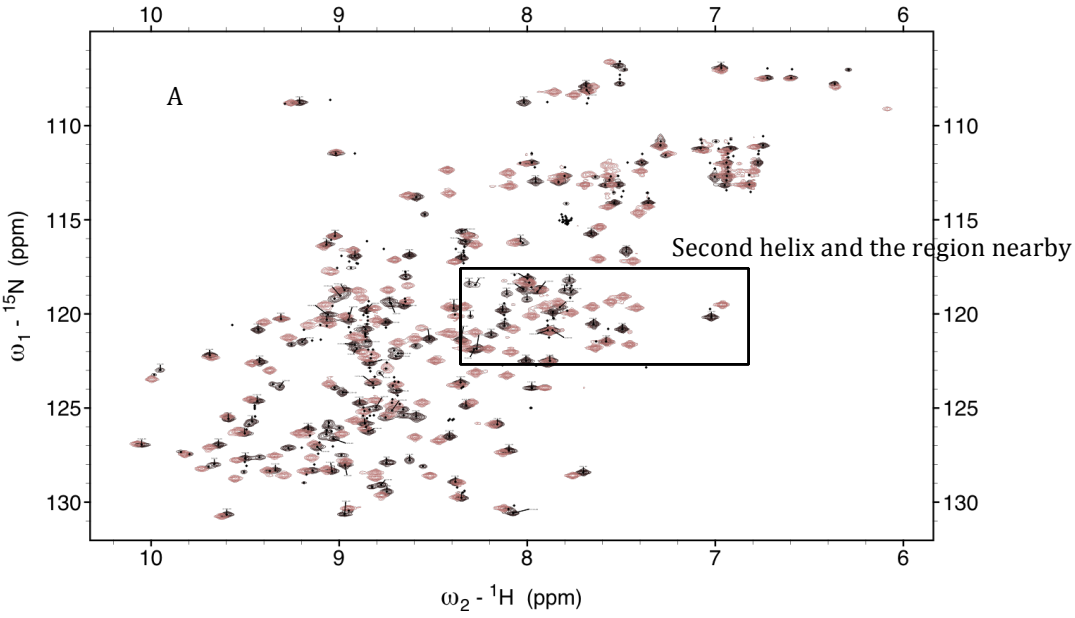

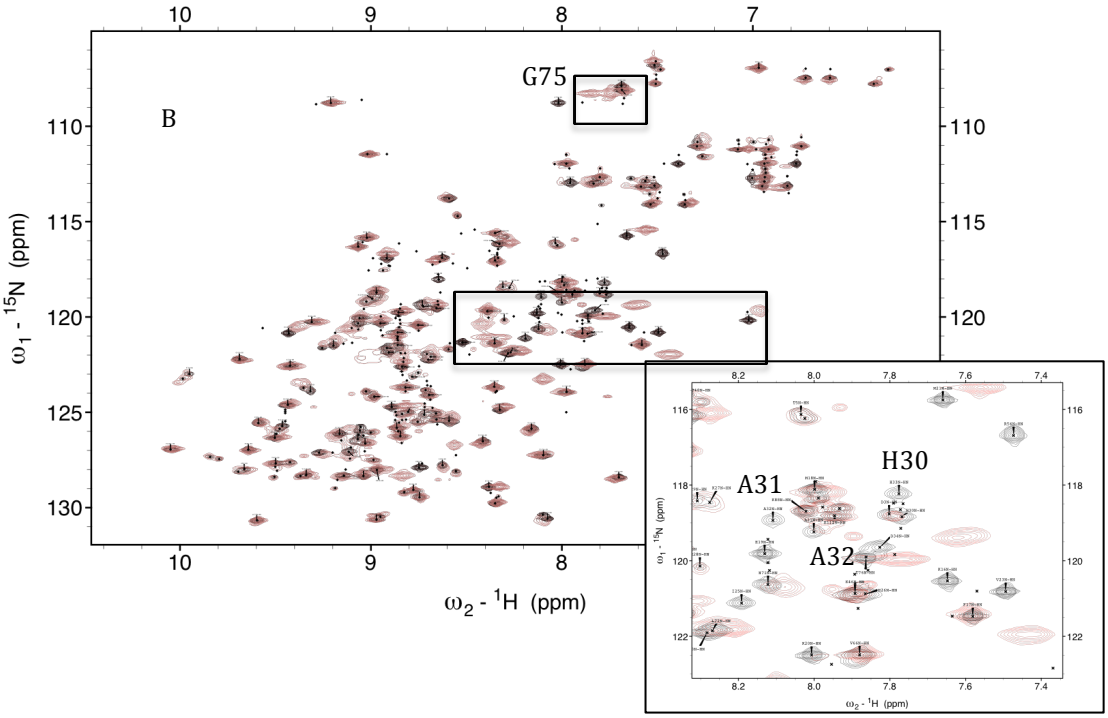

Figure 4.4. *The ^{15}N-HSQC spectra of the Ni-NTA bound- and free forms of the variant as well as wild type hiFABP.* ***A.*** *The comparison of the ^{15}N-HSQC spectra of the wild type hiFABP (red) and the free form (black) of the mutant V26H/L30H.* ***B.*** *The comparison of the ^{15}N-HSQC spectra of the Ni-binding form (red) and the free form (black) of the mutant V26H/L30H. The protein concentration used in recording the HSQC spectrum was 0.5mM, in the sodium phosphate buffer, pH 7.1. For the Ni-NTA bound form (red), the ratio between the Ni-NTA and the protein was 5:1.*

4.1.3. The impact of the mutation on the back portal

When viewing the HSQC spectra, surprisingly, we found some residues showed two splitting peaks, as illustrated in Figure 4.5A, suggesting that two forms undergo slow conformational exchanges. These residues are mapped in the structure (Figure 4.5B). As shown in the figure, they are distributed in the back portal region, opposite to the helical portal region. The splitting peaks were also observed in the Ni-NTA bound form. The slow conformational exchange seemed to be caused by the mutation in V26 and L30, but this conformational exchange did not affect the oleic acid association significantly as shown by the stopped-flow result (Figure 4.10). Early studies have reported the involvement of the back portal in the release of water inside the cavity to make room for ligand binding (16, 17). Another MD simulation

study suggested the capability of this back portal to bind lipid mini-micelle (69). Our observation implied a complicated relationship between the second α helix and the back portal region, which remained to be studied.

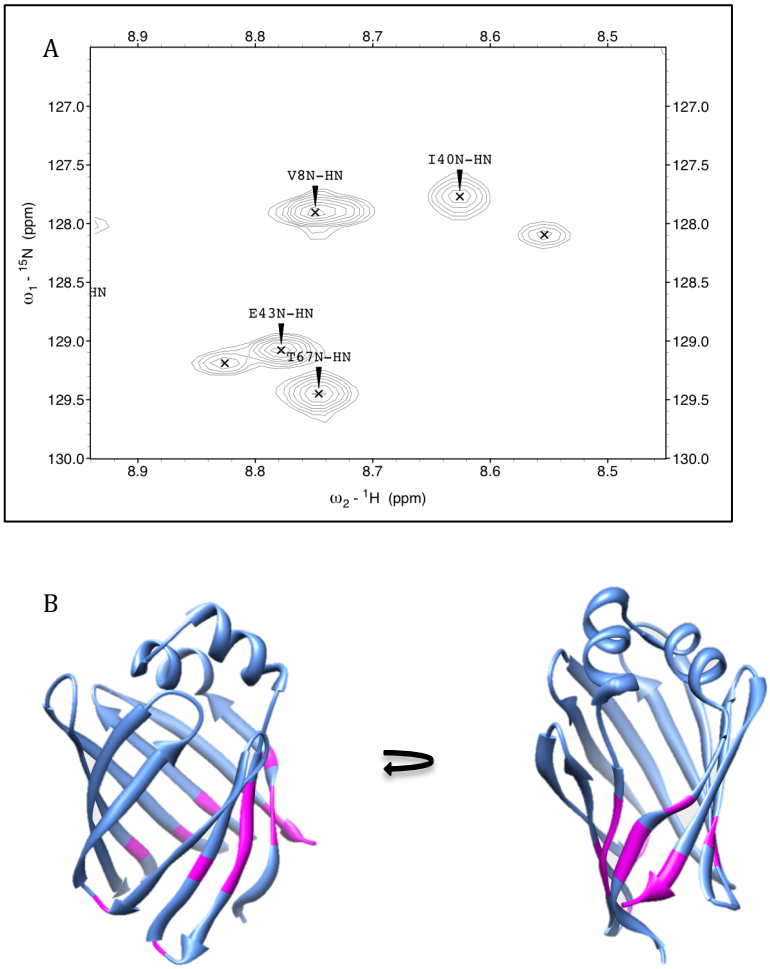

Figure 4.5. *The residues of the mutant V26H/L30H showing two forms in the HSQC spectra.* ***A****. The resonance peaks of E43 and I40 have splitting peaks in the HSQC spectra.* ***B.*** *The residues showing two splitting peaks in the HSQC spectra are mapped in the structure, highlighted in purple.*

4.1.4. Backbone flexibility and global stability

Amide hydrogen exchange rates were measured for the Ni-NTA bound and free forms of mutant V26H/L30H. The Ni-NTA free form was less stable than wild type hiFABP. The C terminus of the second helix (H30-D34), the turns B-C, C-D, E-F and F-G became more dynamic (Figure 4.6). The N

terminus of the second helix (K27-K29) became more stable due to the mutation of V26 and L30, while the C terminal region of the second helix became more flexible (Figure 4.7A). The impairment of the stability might be due to that the mutation to histidine made the helix structure less favored. Histidine has a much lower helix propensity value (0.36) than the Leu (0.92) (70), so the mutation L30H possibly makes the second helix unstable, especially for the C terminus of the second helix.

The invisibility of some residues after Ni-NTA binding, including most of the second helix, made it difficult to measure the amide proton exchange rates of these residues. Nevertheless, the amide hydrogen exchange rates still revealed the change in the dynamics of turn E-F, implying the different flexibility of the portal region. The amide hydrogen exchange profiles of G75 and L72 are shown in Figure 4.7B. These two residues are located in the turn E-F. The other residues in this turn were invisible in HSQC spectrum. The amide hydrogen exchange rates of G75 and L72 became slower after Ni-NTA binding, indicating the increased stability to some extent. It was reasonable to postulate that the Ni-NTA binding should stabilize the second helix, affecting the flexibility of the turn E-F indirectly. Additionally, it should be noticed that residues T67, I108, I109 and G110 became more flexible after the Ni-NTA binding. I108, I109 and G110 are located in the turn H-I, the back portal mentioned in 4.1.3, suggesting a relation between the back portal and the second α helix.

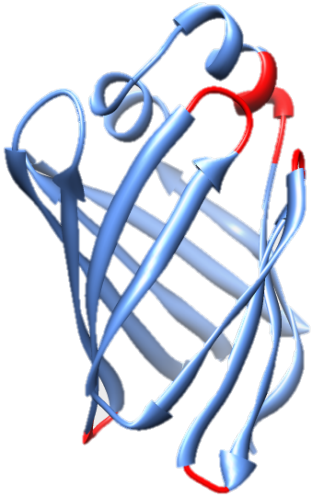

Figure 4.6. *The ribbon representation of the NMR structure of hiFABP (PDB ID:3IFB). The residues showing the faster proton exchange rates than the wild type hiFABP without the Ni-NTA binding are highlighted in red.*

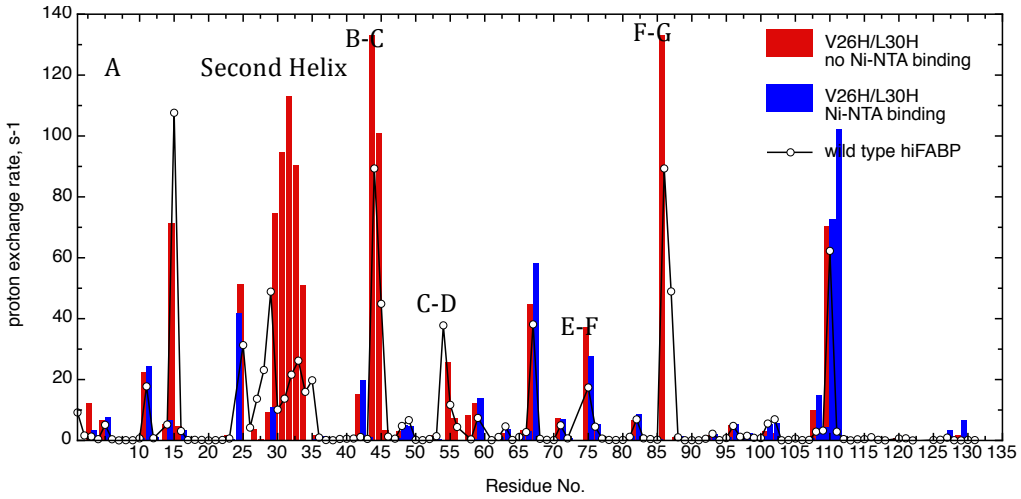

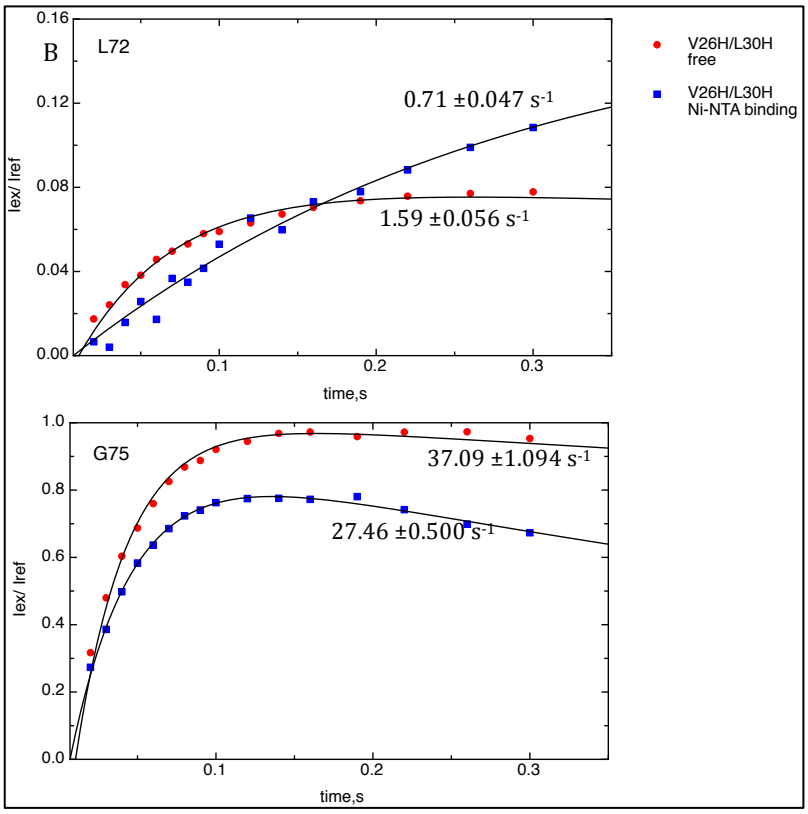

Figure 4.7. *Amide proton exchange rates of the variant V26H/L30H and wild type hiFABP.* ***A.*** *The proton exchange rates of the free form V26H/L30H, the Ni-NTA bound form of V26H/L30H and the wild type hiFABP. There were some residues whose resonance peaks disappeared in the presence of the Ni-NTA binding. Therefore, the proton exchange rates of these residues were missing in the figure.* ***B.*** *The proton exchange profile of the residue L72 and G75. The exchange rate is shown beside the curve. The data of the mutant without Ni-NTA binding is plotted in red. The data of the mutant with Ni-NTA binding is plotted in blue.*

Although it was difficult to investigate the flexibility of the residues in the second helix, we compared the global stabilities of the Ni-NTA bound form and the free form of the mutant V26H/L30H through urea denaturation experiment. As shown in Figure 4.8, the denaturation curves of the two forms exhibited a difference in global stability between them. By fitting the curves, it was found that the Ni-NTA binding made the mutant V26H/L30H more stable. The mutant without the Ni-NTA binding was the least stable among the three groups, consistent with the result of the amide proton exchange rates. The parameters are listed in Table 4.1. The mid-point (Cm) of the denaturation curve of the Ni-NTA bound form was higher than that of the free form even

considering the standard deviation, indicating a increase in the stability. The m-value of the mutant V26H/L30H after the Ni-NTA binding was also increased, suggesting the lager dASA. The value of ΔG^0 of Ni-NTA bound mutant was higher than the free form significantly. This result indicated that Ni-NTA binding to the HxxxH motif stabilized the variant V26H/L30H.

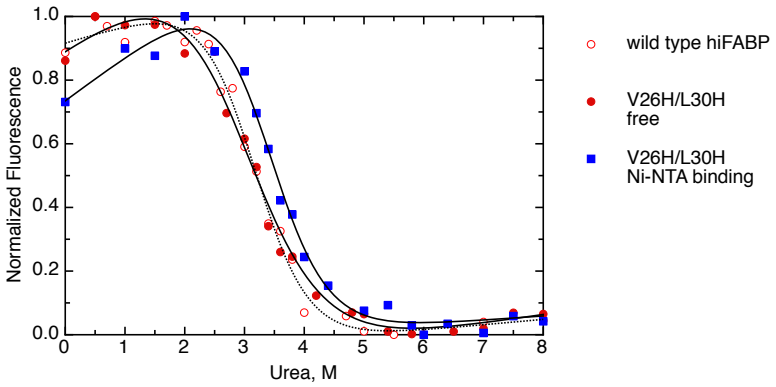

Figure 4.8. *The urea denaturation curves of the variant V26H/L30H. The protein was denatured with urea in the concentration varied between 0~8M, in room temperature, pH 7.1. The protein concentration was 4uM.*

	m-value (kJ/mol/M)	mid point (M)	ΔG^0 (kJ/mol)
wild type hiFABP	5.50±0.815	3.11±0.088	17.11±0.151
V26H/L30H+Ni-NTA	5.16±0.511	3.36±0.067	17.34±0.101
free V26H/L30H	4.54±0.474	2.99±0.097	13.57±0.109

Table 4.1. *The parameters extracted from the urea denaturation curves. The experiment was conducted in room temperature. The pH of the buffer is 7.1. The protein concentration was 4 μM.*

4.1.5. Stopped-flow experiment to measure oleic acid association rate

After knowing the increase in the stability after Ni-NTA binding, we proceeded to the kinetic studies on the oleic acid association. Similar to wild type hiFABP and the mutant K27C/D74C, the intrinsic fluorescence signal increased upon oleic acid binding. The stopped-flow traces were fitted to a double exponential function to extract the two apparent rates (Figure 4.9).

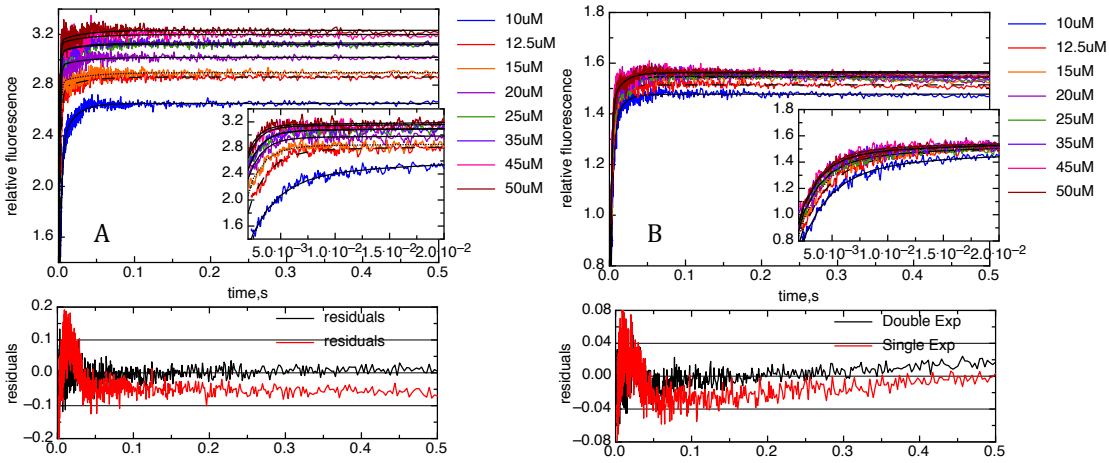

Figure 4.9. *The stopped-flow traces of oleic acid binding to the mutant V26H/L30H without the Ni-NTA binding(A) and with the Ni-NTA binding (B) in 19 °C. The final protein concentration was 3uM, in 50mM pyrophosphate buffer, pH 9.4. The final concentration of the oleic acid was between 7.5~150uM. Not all of the traces of the reactions with different oleic acid concentrations were included. The oleic acid concentrations are listed in the legend. The inset graphs show the fitted curves and the stopped-flow traces. The graphs below the stopped-flow traces show the comparison between the residuals of the fitting with the single exponential function and the one with the double exponential function.*

The stopped-flow traces and the fitting residuals are displayed in Figure 4.9. Similar to the mutant K27C/D74C and wild type hiFABP, a single exponential function was not enough to fit the traces well. The stopped-flow traces were fitted to a double exponential function to extract the two apparent rates. This inadequacy of the single exponential function indicated that there should be two steps contributing to the increase of the fluorescence. Through least square fitting to the double exponential function, one fast apparent rate and one slow apparent rate were obtained for each stopped-flow trace. The fast apparent rate had a dependence on the oleic acid concentration, while the slow apparent rate had no obvious dependence on the oleic acid concentration. The two apparent rates of the Ni-NTA bound form and the free form of V26H/L30H are shown in Figure 4.10. As shown in the figure, the Ni-NTA free form of the mutant had a similar behavior to wild type hiFABP for both of the two apparent rates. In terms of the apparent rate of the fast step, the free form mutant had slightly slower apparent rates than wild type hiFABP.

The plateau of the free form mutant was also ~1000 s^{-1}. In the presence of Ni-NTA binding, the apparent rate of the fast step was reduced significantly. In Figure 4.10A, the plateau of the Ni-NTA bound form of the mutant was ~550 s^{-1}. The rate limit of the oleic acid association was decreased by 45% after Ni-NTA binding to the second helix. According to the reaction model (Model I) proposed in Chapter 3, the rate limit equals to the forward rate of the first conformational exchange step (Step 1). It is reasonable to conclude that Ni-NTA binding stabilizes the second α helix, reducing the rate of the 'lid opening', resulting in the decreased oleic acid association rate.

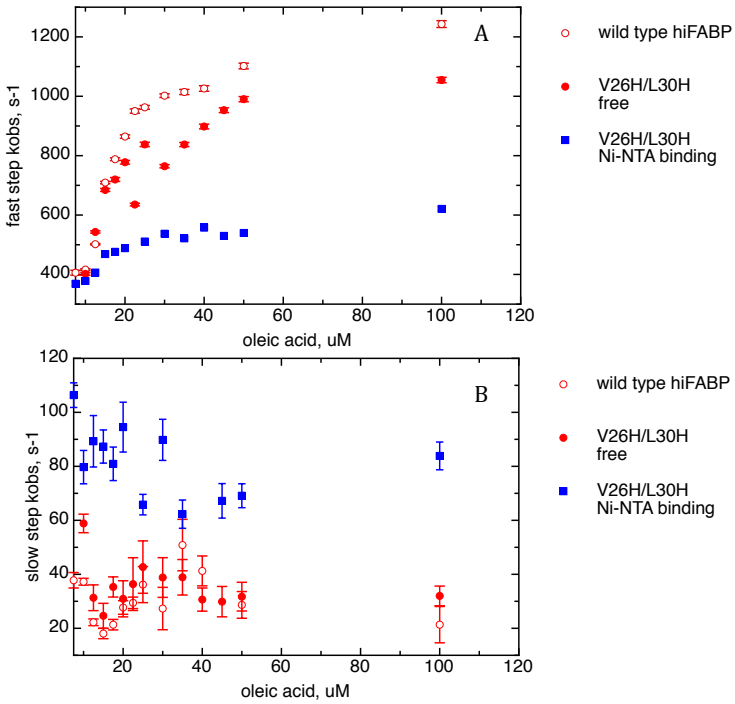

Figure 4.10. *The apparent rates of the mutant V26H/L30H.* ***A****. The apparent rate of the fast step.* ***B****. The apparent rate of the slow step. The experiments were done in 19 ^{O}C, pH 9.4. The protein concentration used for stopped-flow experiment is 4uM.*

With regard to the slow step (Step 3), the last allosteric step, Ni-NTA binding surprisingly increased the apparent rate significantly. As shown in Figure 4.10B, the apparent rate of the Ni-NTA bound form was ~80 s^{-1}, which was two times of wild type hiFABP and the free form of the mutant. This observation suggestd that for the Ni-NTA bound form of the mutant, the

energy barrier of the last allosteric step should be smaller, which might be related to the difference in the stabilities between the holo forms of the Ni-NTA bound and the Ni-NTA free mutant. Based on this postulation, urea denaturation experiments of oleic acid bound proteins (holo form) were performed. As shown in Figure 4.11 and Table 4.2, the holo Ni-NTA bound variant exhibited the highest stability against urea denaturation. This increase in the stability of holo form might lead to the change of the equilibrium and the apparent rate of the last step (Step 3 in Model I). This result suggested that the Ni-NTA bound form might behave differently in the ligand delivery process, which required further studies on the process of ligand delivery to membrane.

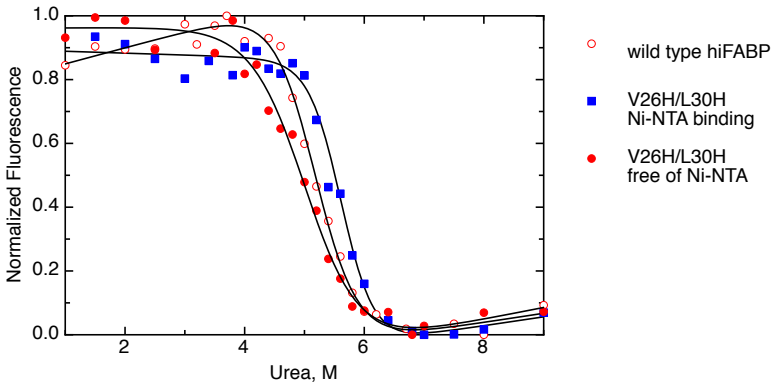

Figure 4.11. *Urea denaturation experiments of the holo form of the vaiant V26H/L30H. The Ni-NTA bound form of the mutant, the free form mutant and wild type hiFABP were saturated with the oleic acid. The holo protein was denatured with the urea in the varied concentration. The experiments were conducted in the room temperature, pH7.1.*

	m-value (kJ/mol/M)	mid point (M)	ΔG^0 (kJ/mol)
wild type hiFABP	6.89±0.578	5.17±0.039	35.62±0.084
V26H/L30H+Ni-NTA	8.95±0.996	5.62±0.039	50.30±0.112
free V26H/L30H	5.41±0.744	5.03±0.081	27.21±0.138

Table 4.2. *The parameters extracted from the urea denaturation curves. The experiment was conducted in room temperature. The pH of the buffer is 7.1. The protein concentration was 4uM.*

4.1.6. Fitting by Dynafit using Model I

The fitting by Dynafit was a global analysis on the stopped-flow traces of different oleic acid concentrations. The reaction model used for fitting was the

same as the fitting of the variant K27C/D74C as mentioned in Chapter 3 (Model I). The results obtained from analyzing the stopped-flow traces by Dynafit were similar to those by the least square fitting. The fitting residuals are displayed in Figure 4.12. The parameters obtained are listed in Table 4.3. The forward rate (k_1) of the first allosteric step was ~1000 s^{-1} for the free form and wild type hiFABP. The k_1 of the Ni-NTA bound form of V26H/L30H was ~550 s^{-1}. During the analysis by Dynafit, the ratio k_{-1}/k_1 was fixed. For the Ni-NTA bound form of the mutant, the ratio k_{-1}/k_1 should not be higher than 40, otherwise the fitting would fail, or the forward rate k_2 would be faster than the diffusion control limit. For the free form of the mutant, the ration k_{-1}/k_1 should not be higher than 30. However, for wild type hiFABP, the ratio k_{-1}/k_1 could be fixed as 50. The ratio reflected the populations of the minor open form ($FABP_{op}$), related with the stabilities of the closed and the opened forms in the first allosteric step (Step 1). The different ratios indicated that the Ni-NTA bound form should be more stable than the Ni-NTA free form in the close state, but less stable than wild type hiFABP. In addition, it was required to raise the ratio k_{-3}/k_3 of the Ni-NTA free form to 0.1 in order to fit the traces well. This result should be related to the lower stability of the holo Ni-NTA free form as demonstrated in the urea denaturation experiment (Figure 4.11).

	k1 (s^{-1})	k-1/k1	k2 ($uM^{-1}s^{-1}$)	k-2 (s^{-1})	k3 (s^{-1})	k-3/k3	Δ F1	Δ F2	Δ F3
wt hiFABP	1055.6±6.3	50	4576.8±71.9	37.5±1.3	25.8±0.83	0.01	0	0.63±0.006	0.64±0.006
Ni free	1078.3±7.87	30	3994.2±56.88	1.0±1.69	33.8±1.33	0.1	0	1.07±0.013	1.10±0.013
Ni binding	547.8±2.94	40	4058.1±69.73	84.1±2.87	74.0±1.57	0.01	0	0.62±0.004	0.65±0.004

Table 4.3. *The parameters fitted by Dynafit of the variant V26H/L30H. The unit of k_1, k_{-2}, k_3 is s^{-1}, and the unit of k_2 is $\mu M^{-1}s^{-1}$. k_1/k_{-1} and k_3/k_{-3} refer to the ratio of k_1 to k_{-1} and k_3 to k_{-3} respectively. The parameters, Δ F1, Δ F2 and Δ F3, refer to the fluorescence response of 1 μM protein.*

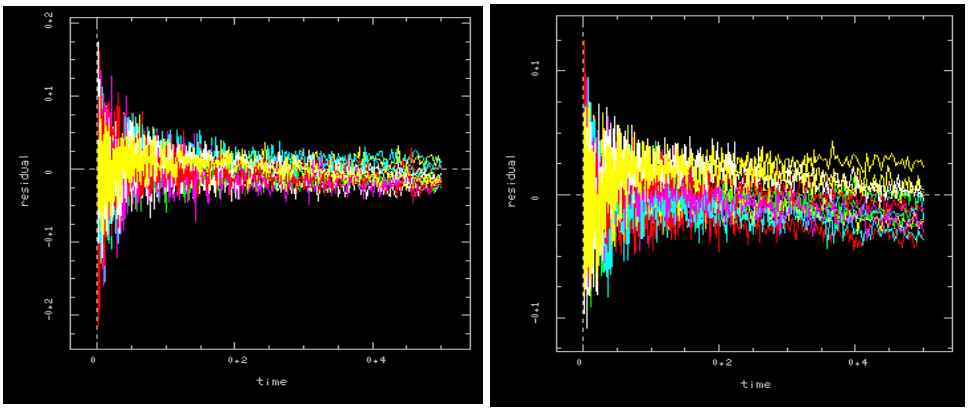

Figure 4.12. *The fitting residuals of the Ni-NTA free form variant (left) and the Ni-NTA bound form variant (right).*

The conclusion drawn from the V26H/L30H mutant observation was consistent with what we obtained from the mutant K27C/D74C, reinforcing that the second helix should be the site for ligand entry.

4.2. Discussion

In this study, the mutant V26H/L30H was proved to be able to bind metal ions Cu^{2+} and Ni^{2+} by ITC and ^{15}N-HSQC spectra. Ni-NTA binding to the second helix increased the protein stability against urea denaturation. In spite of the lack of NMR peaks of some residues in the second helix, it was still found that the amide hydrogen exchange rates of the turn E-F was slowed down after the Ni-NTA binding, indicating the reduced flexibility of the turn E-F to some extent. As a result, the rate of the oleic acid association was slowed down by 45%. These results support the conclusion obtained from the studies on the mutant K27C/D74C.

In the ^{15}N-HSQC spectrum of the mutant without Ni-NTA, the decreased peak intensities of the residues in the second helix indicated that the second helix was less stable than wild type hiFABP. The amide hydrogen exchange rates of the Ni-NTA free form also revealed that the mutation in V26 and L30

made the second helix more flexible (Figure 4.7A). In addition, the turns E-F, F-G, C-D and B-C also became more dynamic, which are mapped in Figure 4.6. This observation indicated a close relation between the second α helix and the turn C-D and E-F. Early studies reported that the side chains of the turn C-D interacted with the C terminal of the second helix, which might affect the orientation and stability of the second helix (24, 71). The interaction between the turn C-D and the C terminal half of the helix should be dominant by hydrogen bonding and hydrophobic interaction, involving the residues L30, A32, F55, A54, S53 and S52 (24). The increased flexibility of the C terminal half of the second helix might disturb the interaction between the turn C-D and the second helix, making the turn C-D become more dynamic.

The ^{15}N-HSQC spectrum of the mutant V26H/L30H exhibited that the back portal in the bottom had two conformations exchanging slowly (Figure 4.5), highlighting the intrinsic role of the back portal. Previous studies indicated that this region might be related to the release of the internal water (16, 17). MD simulation studies on a liver FABP suggested that the back portal might be the site for ligand dissociation (14). Although this pathway of ligand release should be unique to liver FABP, it still suggested that the back portal should play a special role (14). Another MD simulation study reported the interesting role of the back portal in lipid digestion, indicating the capability of the back portal to bind with lipid mini-micelle, while the free monomeric lipid entered through the helical portal (69). In this way, the back portal and the helical portal together made FABP a highly efficient carrier for lipid, considering the high concentration of lipid in daily diet. In our studies, the conformation exchange of the back portal existed in both the Ni-NTA bound and free forms of the mutant V26H/L30H, implying that it should be caused by

the mutation and irrelevant to Ni-NTA binding. This conformational exchange in the back portal had no impact on oleic acid association according to the stopped-flow experiment. These results suggested that the back portal at the bottom might function in compensation for the helical portal region. But it is still illusive whether the back portal is involved in ligand release or ligand admitting.

The urea denaturation experiments together with the proton exchange rates indicated that the second helix should become stable in the presence of Ni-NTA binding. However, this stabilizing effect was not grounded, because the resonance peaks of the residues in the second helix became invisible in HSQC spectra after Ni-NTA binding, making the measurement of proton exchange rates and relaxation rates impossible. Nevertheless, we still observed the decrease in the oleic acid association rate of the Ni-NTA bound variant, implying Ni-NTA binding inhibited the process of oleic acid entry, which should be due to the impairment on the mobility of the second helix. The stopped-flow result was consistent with the conclusion drawn from the double cysteine variant K27C/D74C: the second helix experiences the process of local unfolding, followed by ligand entry.

The stopped-flow experiments also revealed that the last allosteric step was accelerated by Ni-NTA binding (Figure 4.10B and Table 4.3). This observation should be related to the higher stability of the holo form of the Ni-NTA bound mutant, as shown by the urea denaturation experiment. The second helix might be involved in the conformational exchange between $FABP_{op}L$ and $FABP_{cl}L$ (Step 3). This might explain why Ni-NTA binding to the second helix stabilized $FABP_{cl}L$. As a result, the equilibrium and the rate of Step 3 were altered. However, how Ni-NTA binding affected Step 3 remained

unanswered. To address this question, this mutant would be optimized in the future. A different mutant should be generated, in which the second helix would be stabilized by residue substitution, and the further relaxation study may clarify the relation between the second helix and the back portal as well as how the second helix is involved in Step 3.

In summary, the studies on the mutant V26H/L30H verified the crucial role of the second helix in ligand entry. Stabilizing the second helix by Ni-NTA binding slowed down the rate of ligand association. This result reinforced the conclusion that local unfolding of the second helix mediated the process of ligand entry. Moreover, the studies on the mutant V26H/L30H indicated a relation between the second helix and the back portal (Figure 4.5), which required more efforts to elucidate.

Chapter 5. The variant V60C/Y70C and the gap D-E

5.1. Result

5.1.1. Intra-molecule disulfide bond between the gap D-E

The gap between strands D and E is located just below the helical portal region. The width between these two strands is relatively large, and no hydrogen bonds are found between these two β strands. The gap D-E possesses many hydrophobic residues and has been considered as the hydrophobic core of hiFABP, thus playing a crucial role in maintaining the β barrel structure (17, 21). Early studies suggested the gap D-E might be an alternative pathway for fatty acid entry and release, other than the helical portal (19, 29). Based on the protection factors shown in Figure 3.15B, strands D and E had the fastest proton exchange rates among all the β strands, suggesting possible relation between the flexibility of the helical portal region and the two strands. Although it is confirmed that the helical portal should be the site for ligand entry as mentioned in the last two chapters, we are interested in finding out the role of the gap D-E in protein folding, stability and ligand interaction.

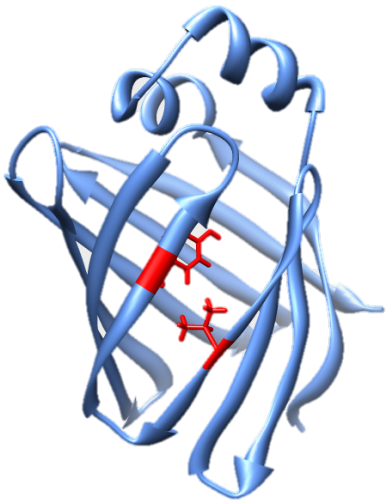

Figure 5.1. *The ribbon representation of the wild type hiFABP (PDB ID:3IFB). The residues V60 and Y70 are mutated to Cysteine, highlighted in red.*

To investigate the role of the gap D-E, an intra-molecule disulfide bond was introduced to this region, pulling the two strands closer and making the β barrel shrink. A double point mutant V60C/Y70C was generated for this purpose (Figure 5.1). The ^{15}N-HSQC spectrum of this protein suggested that the mutant could not form the disulfide bond completely. Different from the mutant K27C/D74C, only 60 % of the protein could form the intra-molecule disulfide bond. Non-reduced SDS-PAGE analysis and gel filtration confirmed that no dimer or oligomer existed. In order to separate the reduced and oxidized forms, thiol activated beads (GE Health) was utilized. Proteins were applied to the beads, those with free thiol groups were linked to the beads by forming disulfide bonds with the beads, while those with the intra-molecule disulfide bond (without free thiol groups) were in the flow-through. In this way, we successfully obtained the pure form with the intended intra-molecule disulfide bond. A comparison of ^{15}N-HSQC spectra between the samples with and without the DTT treatment confirmed the presence of the disulfide bond (Figure 5.2A). The NMR resonance assignments of the two forms of V60C/Y70C were obtained based on the assignments of wild type iFABP and the ^{15}N-HSQC and ^{15}N-NOESY data of the mutant. Residues exhibiting significant changes in chemical shifts clustered to strands C, D, E and F. Interestingly the residues in the second helix also showed significant changes. In comparison to the reduced form, the ^{15}N-NOESY spectrum of V60C/Y70C with the disulfide bond did not show any additional NOE peaks between the residues in strand D and E, which were expected if these two strands formed the anti-parallel β sheet. The ^{15}N-NOESY slices of V61 and N71 are shown for example in Figure 5.2B. The residues in the other β strands showed similar NOE patterns between the reduced and oxidized

forms. The NOESY slices of T48 and E77 are shown in Figure 5.2C as example. This result indicated that the intra-molecule disulfide bond did not make the two strands into a proper β sheet. Instead the intra-molecule disulfide bond might alter the orientations of strands D and E. For residues in the other β strands, the similar NOE patterns suggested a similar antiparallel structure. The different orientations of strands D and E as well as the structure of the mutant can be further investigated by ^{13}C, ^{15}N-edited NOESY in the future.

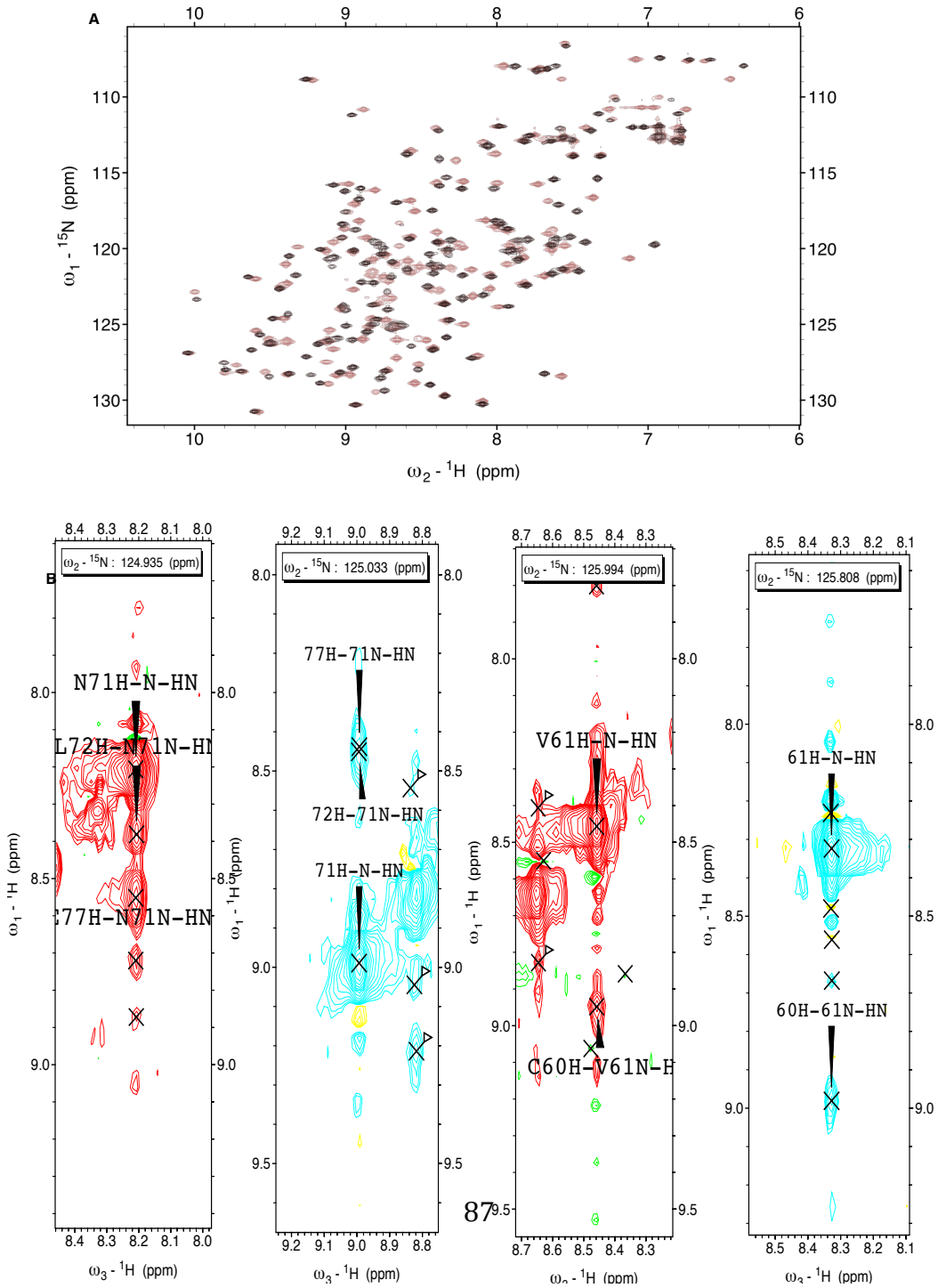

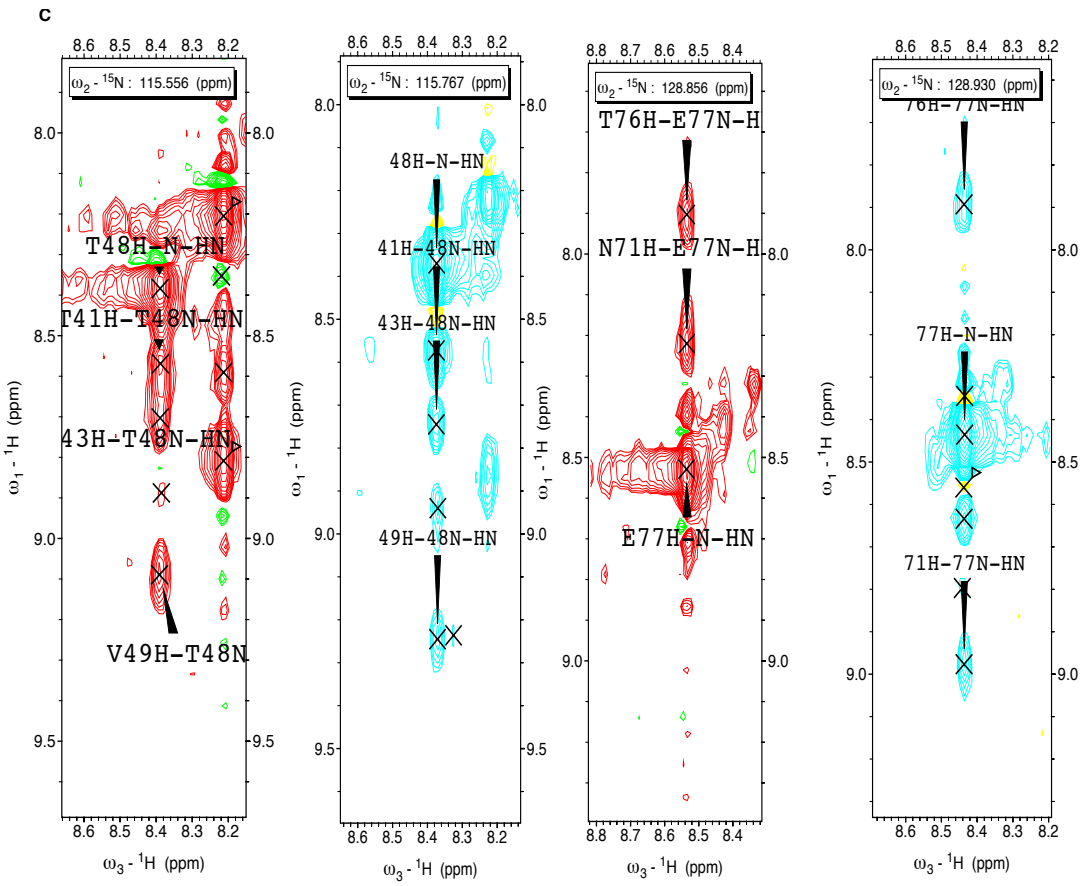

Figure 5.2. *The 15N-HSQC spectra of the two forms of variant V60C/Y70C and the 15N-edited NOESY slices of several residues close to the mutation points.* ***A.*** *The comparison between the ^{15}N-HSQC spectra of the mutant V60C/Y70C with (black) and without (red) DTT treatment.* ***B.*** *The NOESY slices of residues V61 and N71 of the reduced form and the non-reduced form.* ***C.*** *The NOESY slices of residues T48 and E77 of the reduced form and the non-reduced form.*

5.1.2. The effect of the intra-molecule disulfide bond on global and local stability

An intra-molecule disulfide bond usually has an impact not only on the structure but also on the flexibility of the protein. To further compare the stabilities of the two forms of the mutant V60C/Y70C, urea denaturation and amide hydrogen exchange experiments were conducted.

The result of urea denaturation is demonstrated in Figure 5.3. The parameters from the denaturation data are listed in Table 5.1. Comparing with wild type hiFABP, the reduced form exhibited a slightly decreased stability. The mid-point (Cm) of the reduced mutant was 2.94 M, that with the disulfide

bond was 2.67 M. Both forms of the mutant exhibited a higher m-value than wild type hiFABP, indicating the larger dASA possibly due to the substitutions of V60 and Y70. Based on the denaturation parameters, the intra-molecule disulfide bond decreased the protein stability, which might be due to the distortion of strands D and E.

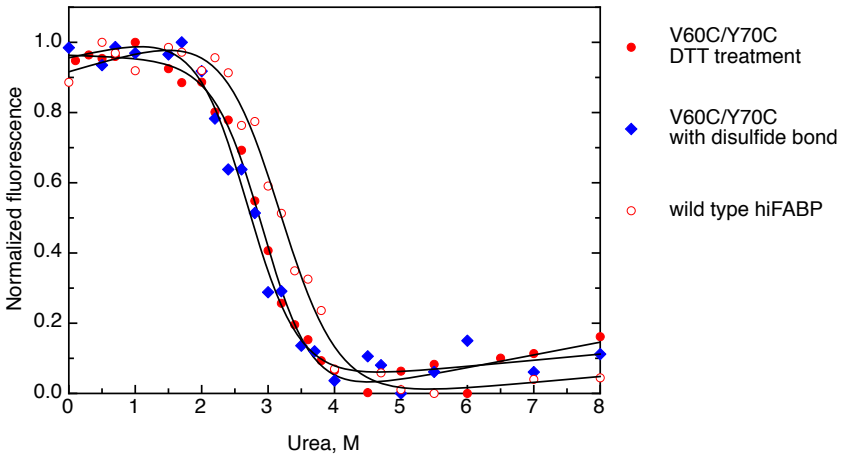

Figure 5.3. *The urea denaturation curves of the mutant V60C/Y70C in the presence and the absence of the disulfide bond as well as the wild type hiFABP. The protein was denatured with increasing urea concentration from 0 to 8M in room temperature, pH 7.1. The protein concentration was 4uM.*

	m-value(kJ/mol/M)	mid-point (M)	ΔG^0 (kJ/mol)
wild type hiFABP	5.50±0.815	3.11±0.088	17.11±0.151
V60C/Y70C with disulfide bond	6.16±0.985	2.67±0.095	16.44±0.164
V60C/Y70C with DTT treatment	6.53±0.674	2.94±0.053	19.20±0.105

Table 5.1. *The parameters extracted from the urea denaturation curves of the variant V60C/Y70C and wild type hiFABP. The experiment was conducted in room temperature. The pH of the buffer is 7.1. The protein concentration was 4uM.*

The exchange of amide protons with solvent protons is a process limited by the transition between the 'closed' form and the 'open' form of protein (56). So the exchange rates reflect the backbone flexibility. The comparison of the amide proton exchange rates is shown in Figure 5.4. The reduced form showed a similar pattern to wild type hiFABP, but some residues had faster proton exchange rates. Residues of the second helix, D15 (in the first helix)

and the turns B-C, C-D, D-E, F-G and H-I in the reduced mutant exhibited slightly faster exchange rates than wild type hiFABP (Figure 5.4).

The mutant with the intra-molecule disulfide bond also displayed a similar pattern to wild type hiFABP. Residues close to the disulfide bond exhibited decreased proton exchange rates, like C60-E63, N71 and L72, as shown in the bottom of Figure 5.4. However, the exchange rates of residues in the second α helix and turns B-C, D-E and F-G were faster than those in the reduced form and wild type hiFABP, suggesting a higher flexibility in these regions. This observation was consistent with the decrease of the stability against urea denaturation upon the disulfide bond formation. The change in the structure of the β barrel may disrupt the interaction between the second α helix and the β turns C-D and E-F. It indicated that the interaction between the second α helix and turns C-D and E-F should be important for the stability of the second helix.

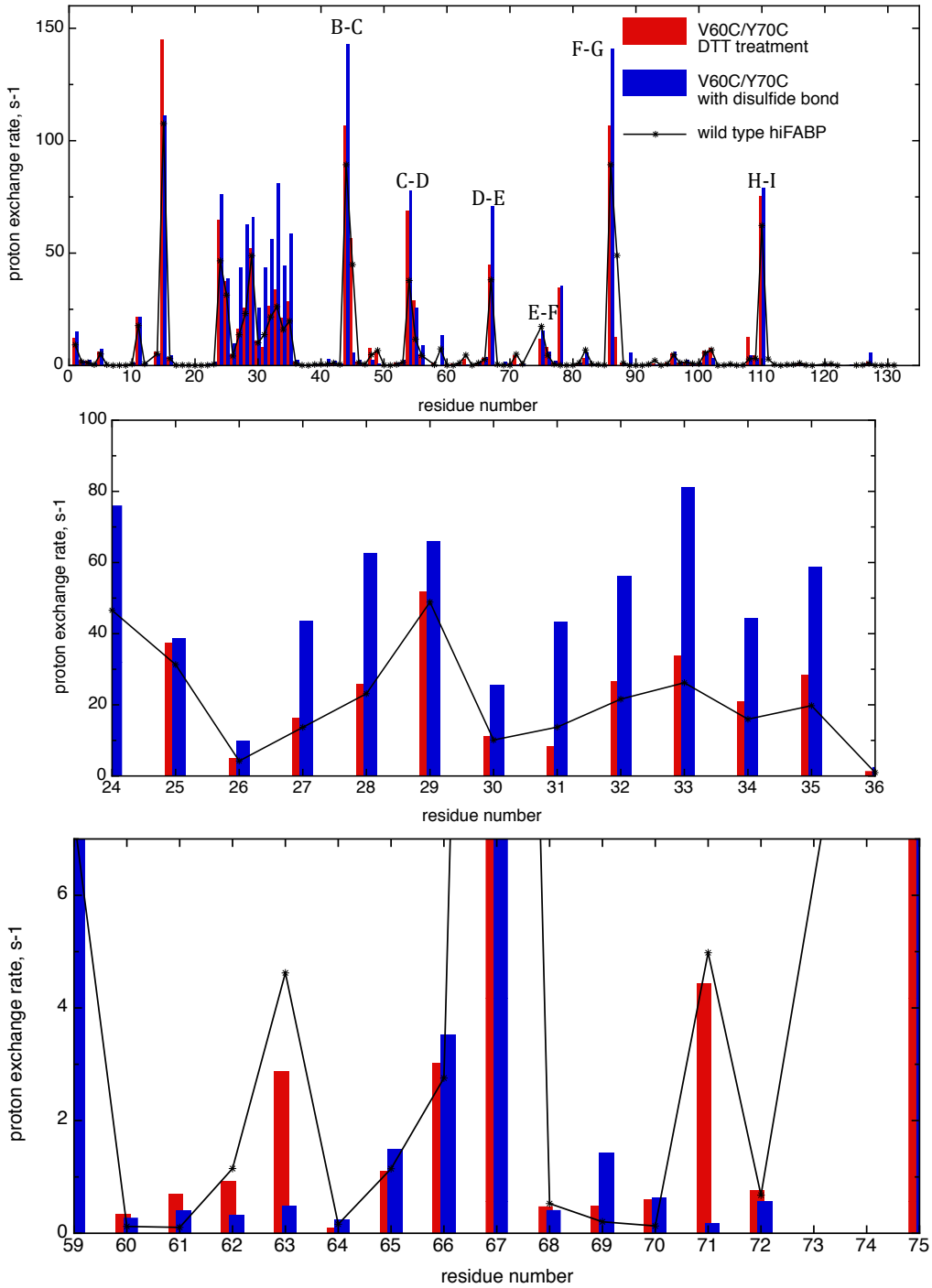

Figure 5.4. *The proton exchange rates of the mutant V60C/Y70C in the presence (blue bar) and the absence (red bar) of the disulfide bond as well as the wild type hiFABP (black star). The exchange rates of all the residues are shown in the top figure except for several residues without resonance peaks in HSQC spectra. The middle figure contains the exchange rates of residues in the second helix. The bottom figure contains the exchange rates of residues close to the two Cysteines C60 and C70. The experiment was conducted in 30 °C. The pH was 7.1, in phosphate buffer (20mM sodium phosphate, 20mM NaCl).*

5.1.3. ANS binding to mutant V60C/Y70C

To further investigate the relationship between the dynamics and ligand binding of hiFABP, 1-Anilinonaphthalene-8-Sulfonic Acid (ANS, an analog to the native ligand) was utilized to study the effect of the disulfide bond on ligand binding. This organic molecule enters into FABP and binds to the cavity inside in a similar way to oleic acid (26, 72, 73). During ANS titration to the two forms of the mutant, most of the residues showed similar chemical shift walking except for several residues. The most obvious difference in the chemical shift walking was observed in residues L36, N69 and E63 (Figure 5.5). Residues L36 and N69 became invisible when the ratio between ANS to the protein was beyond 0.2:1 (the first titration point) for the mutant with the disulfide bond. Residue E63 became invisible at first, and then it appeared in the last titration point again. In the reduced mutant these residues showed progressive changes in chemical shift and intensity. The difference in chemical shift perturbation implied that the mutant with disulfide bond might experience a slower exchange between ANS-free and ANS-bound forms.

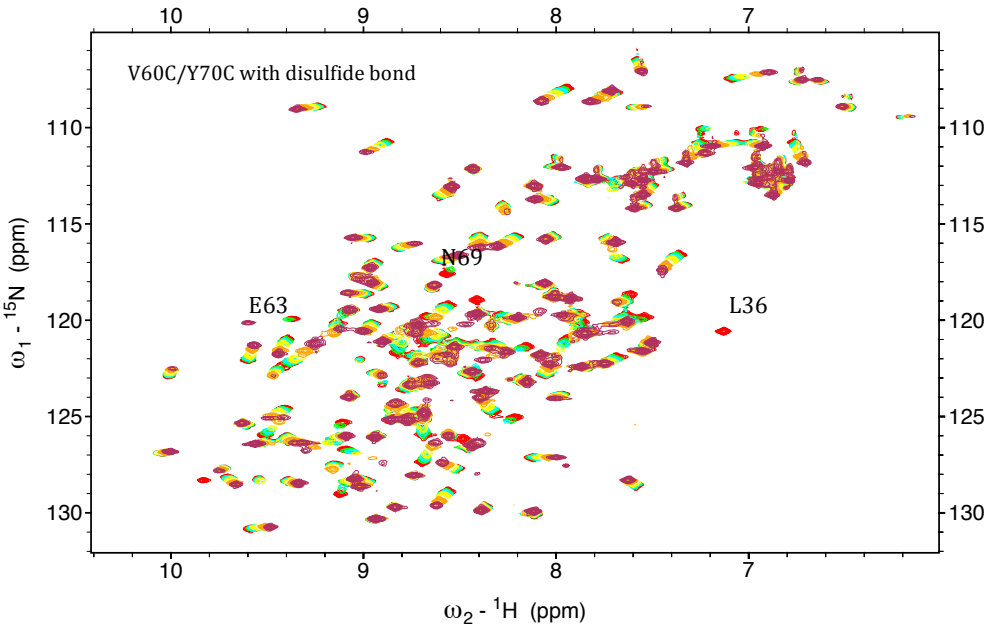

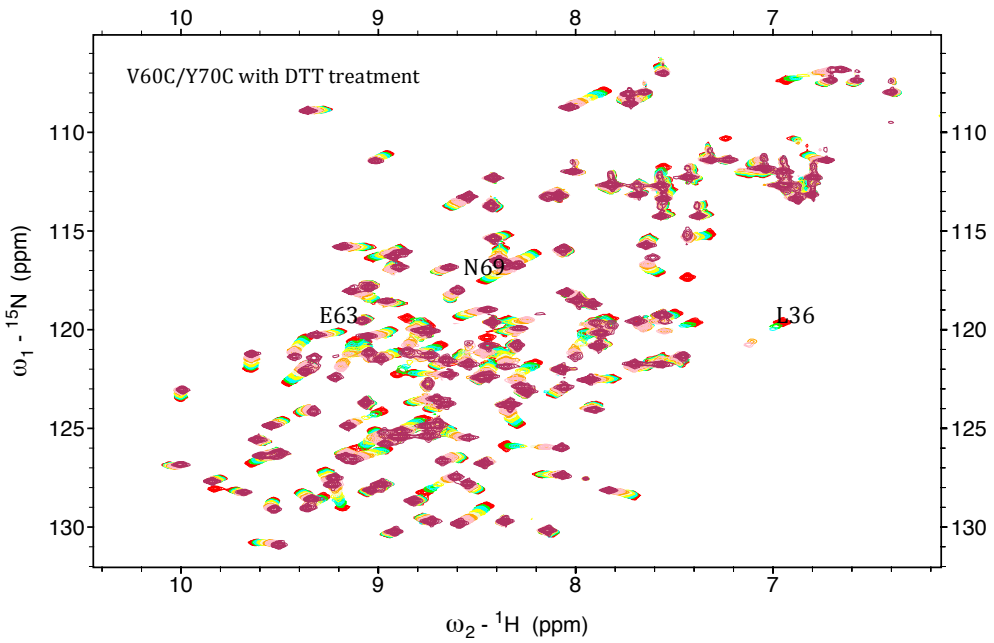

Figure 5.5. *ANS titrations of the two forms of the mutant V60C/Y70C with ANS. The mutant V60C/Y70C was titrated with ANS under room temperature, pH 7.1. The protein concentration was 0.4 mM for both forms of the mutant.*

The binding affinities of the reduced and oxidized mutant were further determined by ANS titration detected by fluorescence spectrometer. In this experiment, ANS concentration was 1 μM and titrated with the protein. By fitting the titration curve, shown in Figure 5.6, the dissociation constant was determined.

First of all, the fluorescence enhancement of the ANS decreased by ~50% upon binding to the mutant with the disulfide bond than to the reduced mutant. The enhancement coefficient of the reduced form upon ANS binding was 247.23±1.74 μM^{-1}, which was significantly higher than the form with the disulfide bond (130.14±3.01 μM^{-1}), indicating some difference in the structure and/or the polarity of the binding pocket. In terms of the binding affinity, there was no significant difference between the two forms (11.54±0.41 μM and 11.69±1.36 μM), but both of them had a weaker binding affinity than wild type hiFABP (6.19±0.26 μM). It indicated that residues V60 and Y70 should be critical in the interaction with the ligand.

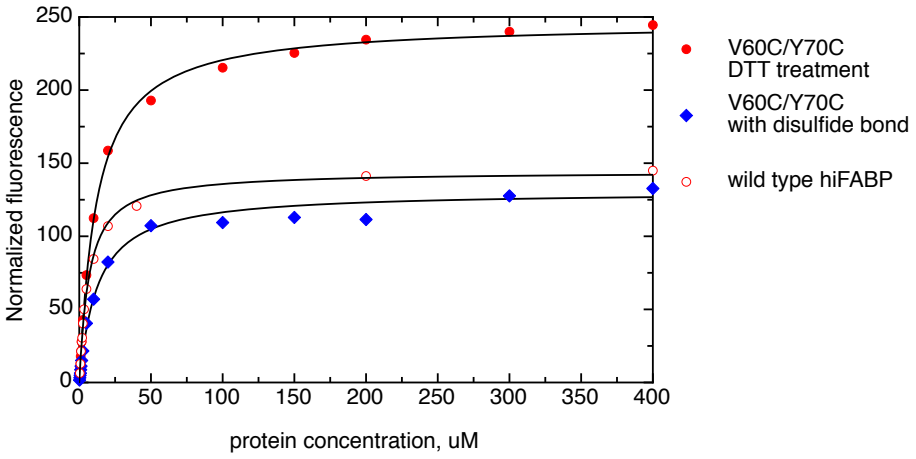

Figure 5.6. *The titration of ANS with the reduced and oxidized mutant hiFABP V60C/Y70C as well as wild type hiFABP. The concentration of ANS was 1 μM, reversely titrated with the protein. The K_D of the reduced form of the mutant (red dots) was determined to be 11.54±0.41 μM. The enhancement coefficient was 247.23±1.74 μM^{-1}. The K_D of the mutant with disulfide bond (blue dots) was determined to be 11.69±1.36 μM. The enhancement coefficient was 130.14±3.01 μM^{-1}. The K_D of wild type hiFABP was determined to be 6.19±0.26 μM. The enhancement coefficient was 145.26±1.60 μM^{-1}.*

5.1.4. Oleic acid association rates of mutant V60C/Y70C

To further investigate the effect of the intra-molecule disulfide bond on the rate of ligand binding, stopped-flow experiment was utilized to measure the reaction rates. The native ligand of FABP, oleic acid, was used for the stopped-flow experiment, of which the traces are shown in Figure 5.7. The stopped-flow traces exhibited that the intrinsic fluorescence was quenched with increased oleic acid concentration, which was exclusively observed in the variant V60C/Y70C upon ligand binding. Figure 5.8 displays this concentration-dependent quenching for the two forms of the variant V60C/Y70C. The traces could be fitted to a double exponential function, similar to those of the mutant K27C/D74C. By fitting the traces, we found that the quenching occurred in the slow step (Step 3 in Model I), of which the amplitude was negative. For the quenching, the absolute value of the amplitude increased with increasing oleic acid concentration. This quenching made accurate measurements of the rate constants difficult, especially when

the oleic acid concentration was high due to the fast reaction rates and the small total amplitude.

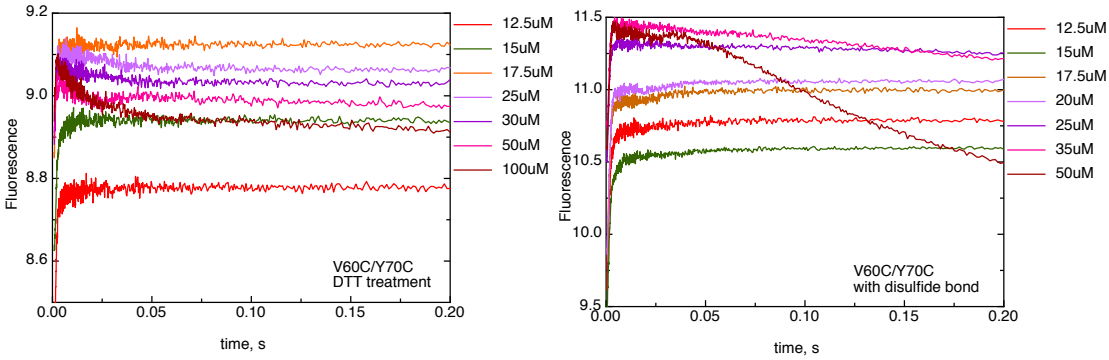

Figure 5.7. *Stopped-flow traces of the mutant V60C/Y70C mixing with oleic acid. The experiment was conducted under 19 °C, in 50mM pyrophosphate buffer, pH 9.4. The final concentration of the oleic acid was between 10~100 μM. Not all of the traces of the reactions with different oleic acid concentrations were included. The final protein concentration was 1uM.*

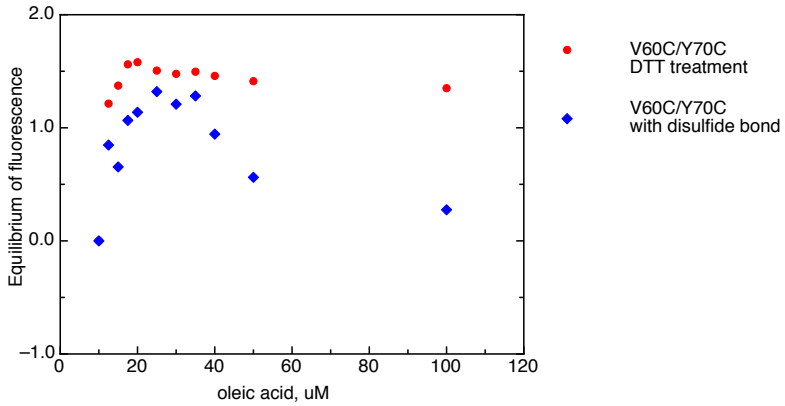

Figure 5.8. *Concentration-dependent quenching of V60C/Y70C upon ligand binding. During the stopped-flow experiments, the protein was mixed with oleic acid in varied concentration (10-100 μM) to measure the rate of oleic acid association. For each oleic acid concentration, the fluorescence signal arrived the equilibrium after some time. Each equilibrium value was subtracted by the one of the trace of 10 μM oleic acid to get the relative equilibrium value (Y-axis). The relative values were plotted against oleic acid concentration.*

For the traces of low oleic acid concentrations, accurate fitting was still feasible. When oleic acid concentration was below 25uM, the apparent rates exhibited no significant difference between the reduced and the oxidized mutant for the fast step (Step 2, Model I), as shown in Figure 5.9A. Compared with wild type hiFABP, both forms exhibited slightly faster reaction rates, which may be due to the higher flexibility of the second helix and the turns (Figure 5.4).

In terms of the traces at higher oleic acid concentrations, the reaction rates could be estimated only by fitting the data before 0.02 s. The rate limit of the form with the disulfide bond should be ~1200 s^{-1}, and the rate limit of the reduced form should be faster (~1400 s^{-1}). The amide proton exchange rates suggested that the form with the disulfide bond had higher flexibility in the second helix (Figure 5.4). However, the form with the disulfide bond in the gap region did not exhibit a faster oleic acid association rate than the reduced form of V60C/Y70C. The reason for the slower association rate might lie in the distortion in strands D and E caused by the disulfide bond, which would affect the interaction between the second helix and turns C-D and E-F. Moreover, it should be noticed that the proton exchange rate only reflects the backbone flexibility, but not the rate of the conformational exchange relevant to ligand entry (Step 1 in Model I). The latter one happens in a much faster timescale than proton exchange does. As a result, the rate of the conformational exchange between the closed and opened forms was not necessarily faster for the oxidized mutant than the reduced mutant.

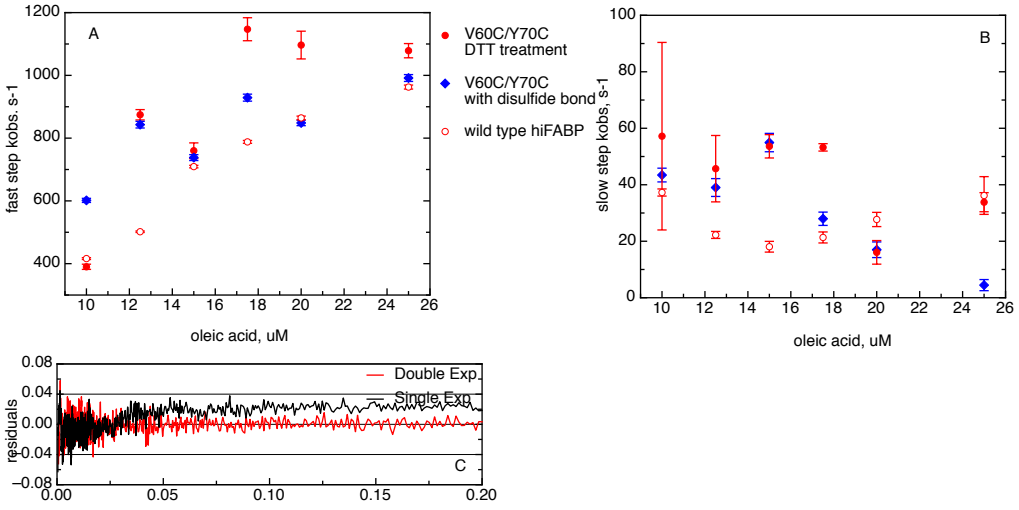

Figure 5.9. *The reaction rates and the residuals extracted from the stopped-flow experiment of the mutant V60C/Y70C.* ***A.*** *The rates of the fast step of the two forms of variant V60C/Y70C and wild type hiFABP.* ***B.*** *The rates of the slow step of the two forms of variant V60C/Y70C and wild type hiFABP.* ***C.*** *The residuals of fitting to the*

double and single exponential functions. The protein concentration was 1 μM, in pyrophosphate buffer, pH9.4. The temperature was 19 ^{O}C.

5.1.5. Single point mutants V60C and Y70C

To further investigate the importance of residues V60 and Y70, we generated two single point mutants, V60C and Y70C. The denaturation curves are shown in Figure 5.10. Mutant V60C was more stable than mutant Y70C. The parameters of urea denaturation are listed in Table 5.2. The mid-point of V60C was higher than Y70C while the m-value of V60C was smaller. The mutation Y70C increased dASA and decreased protein stability, while V60C behaved in a reverse way. Under the combined effect of the mutations at both V60 and Y70, the double point mutant showed a higher dASA and lower mid-point than wild type hiFABP. This result indicated that residue Y70 should be more important for protein stability.

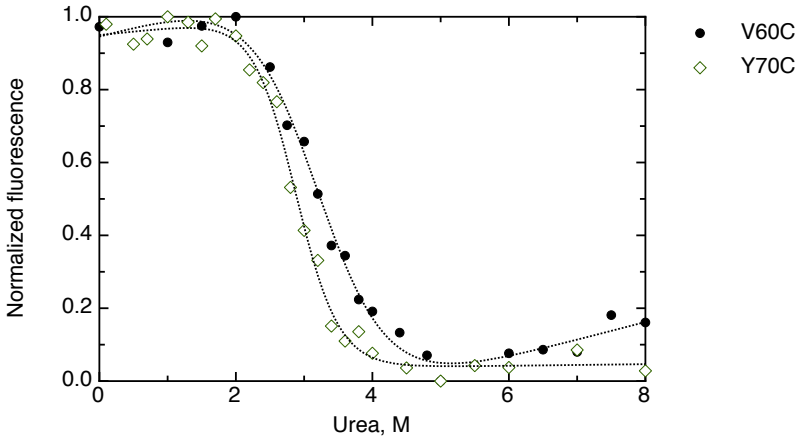

Figure 5.10. *Urea denaturation curves of mutants V60C and Y70C. The protein was denatured with various concentration of urea (0~8M), under room temperature, pH 7.1. The protein concentration was 4uM.*

	m-value	mid point (M)	ΔG^0 (kJ/M)
wild type hiFABP	5.50±0.815	3.11±0.088	17.11±0.151
V60C/Y70C with DTT treatment	6.53±0.674	2.94±0.053	19.20±0.105
V60C	4.75±0.558	3.20±0.093	15.20±0.121
Y70C	7.71±0.929	2.87±0.051	22.13±0.122

Table 5.2. *The parameters extracted from urea denaturation curves of the single point mutants. The experiment was conducted under room temperature. The pH of the buffer is 7.1. The protein concentration was 4uM.*

To further study the effect of the single point mutation on the kinetics of ligand entry, stopped-flow experiments were conducted. The stopped-flow traces of mutant Y70C reacting with oleic acid are shown in Figure 5.11A. Mutant Y70C exhibited concentration-dependent quenching of fluorescence signal, but the amplitude of quenching was much smaller (Figure 5.11B) than the double cysteine mutant. The threshold of the quenching for Y70C was around 22.5 μM, as displayed in Figure 5.11C. The reduced form of variant V60C/Y70C exhibited a similar threshold around 20 μM. Mutant V60C did not show any quenching upon ligand binding. So the quenching should be mainly caused by the mutation in Y70.

Fitting the data before 0.02s, we found that apparent rates for Y70C were slower than those for the reduced double point mutant. The maximum rate of oleic acid association was ~1000 s^{-1}, similar to wild type hiFABP. According to Model I we proposed in Chapter 3, the fast step should be corresponding to ligand binding to $FABP_{op}$ (Step 2), which limited by Step 1 ($FABP_{cl} \Leftrightarrow FABP_{op}$), and the slow step should be the allosteric reaction after ligand binding (Step 3). The fact that the fast step was not quenched implied that Y70 might have less involvement in step 1 and step 2, but critical in step 3.

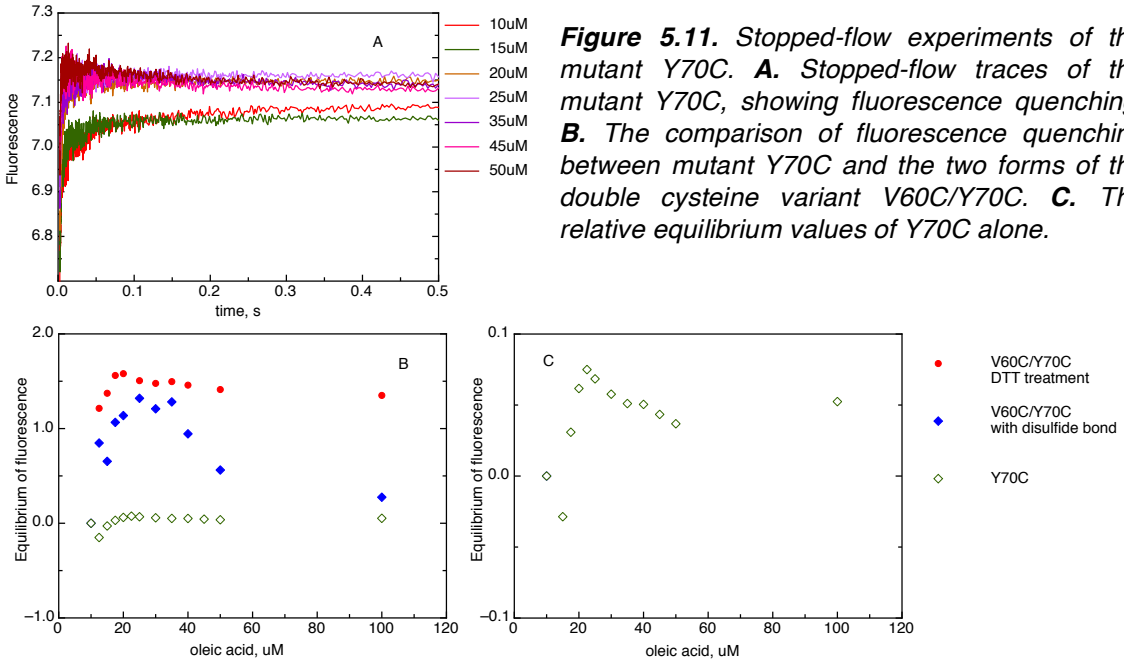

Figure 5.11. *Stopped-flow experiments of the mutant Y70C.* ***A.*** *Stopped-flow traces of the mutant Y70C, showing fluorescence quenching.* ***B.*** *The comparison of fluorescence quenching between mutant Y70C and the two forms of the double cysteine variant V60C/Y70C.* ***C.*** *The relative equilibrium values of Y70C alone.*

For the mutant V60C, no quenching was observed. Its stopped-flow traces were similar to those for wild type hiFABP. Figure 5.12A and B are the plots of the apparent rates of the fast step and the slow step, respectively. By comparing with wild type hiFABP, the rate limit of the fast step was 20% slower than wild type hiFABP (Figure 5.12A), while the rate of the slow step exhibited no significant difference (Figure 5.12B). The mutant V60C unexpectedly slowed down the rate-limiting step (Step 1 in Model I). According to the conclusion in Chapter 3, Step 1 in Model I is corresponding to local unfolding of the second helix. The above observation on V60C indicated that the mutation V60C might limit the motion of the second helix to some extent.

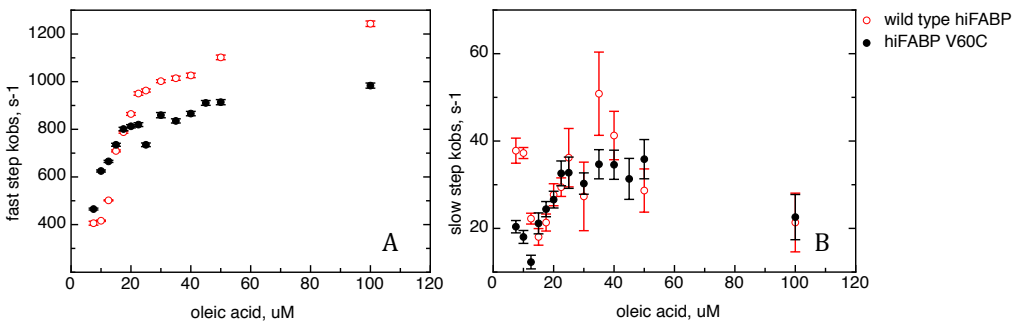

Figure 5.12. *The apparent rates of the fast step (A) and the slow step (B) for mutant V60C and wild type hiFABP.*

5.2. Discussion

The gap D-E plays a critical role in protein folding and stability (74). The wide gap between strands D and E might be the result of a favored folding pathway (71). During folding, the folding intermediate adopts an open β sheet first, followed by a more compact β sheet follows but without hydrogen bonds in gap D-E (30). In this study, an intra-molecule disulfide bond was introduced between residues C60 and C70 in the mutant V60C/Y70C. The closer distance between the two residues failed to make strands D and E into a proper anti-parallel β sheet, as suggested by the ^{15}N-NOESY spectra. The lack of NOEs between the residues of the two strands indicated that the two strands might be distorted, rather than forming β sheet. It may be unfavoured during protein folding for strands D and E to form β sheet.

The amide proton exchange rates revealed that once the intra-molecule disulfide bond formed, the second α helix as well as turns B-C, D-E, E-F and F-G became more dynamic. This increased flexibility may be due to the distortion of strands D and E by the disulfide bond. It is reasonable to postulate that the interaction between the second helix and turns C-D and E-F may be interrupted as a result of the distortion in strands D and E, which could also account for the increased flexibility of the second helix.

The reduced form of the variant exhibited lower stability and faster oleic acid association rate than wild type hiFABP, and fluorescence quenching was observed for the reduced mutant. The studies on the single point mutant Y70C identified the cause of the different fluorescence property, implying a

special role of Y70 in the interaction with the ligand. According to the structure of hiFABP, residue Y70 is located in the ligand-binding pocket (61, 75). The Trp fluorescence is sensitive to the polarity of the surrounding environment (76). The mutation of Y70 possibly altered the chemical environment of the oleic acid binding pocket. Hence the Trp fluorescence was quenched in a ligand dependent way.

The reduced form of variant V60C/Y70C exhibited a severer fluorescence quenching upon ligand binding than the single point mutant Y70C did, implying that V60 should also be involved in ligand binding. The stopped-flow experiments on mutant V60C revealed a slower apparent rate of ligand-binding step (Step 2 in Model I) and a smaller rate limit (forward rate of Step 1), suggesting possible relationship between residue V60 and the process of ligand entry.

Although the current study cannot clarify the function of the gap D-E, these results highlight its significance in ligand entry and binding. To figure out the role played by gap D-E, further dynamics and kinetics studies in the processes of protein folding, ligand association and interaction with membrane are required in the future.

Chapter 6. Conclusion and Future Work

Based on dynamics, structure and kinetics studies on the mutant K27C/D74C, the conclusion on the mechanism underlying ligand entry adopted by this hiFABP is obtained: the second helix undergoes a process of local unfolding, allowing ligand entry through this unfolded helix. Although the mutation K27C/D74C has a strong effect on ligand association, the structure of the mutant is very similar to wild type hiFABP. The intra-molecule disulfide bond slows down the motion of the helical portal region, resulting in a significantly slower oleic acid association rate. This observation confirms the essential role of the helical portal region in during ligand entry. At the same time, the slower motion makes it possible to characterize the functionally relevant dynamics by NMR relaxation dispersion. The relaxation dispersion analysis on the disulfide bond mutant K27C/D74C reveals an extra conformational exchange between the native state and a minor "invisible" state at a rate of ~14000 s^{-1}, which is exclusive to the second helix and the residues nearby. The minor state adopts a local unfolded conformation in which the second helix is mainly unfolded. The forward rate of the local unfolding process is consistent with the rate-limit of oleic acid association obtained from the stopped-flow experiment, further confirming that ligand entry occurs after the local unfolding of the second α helix. This mechanism has never been detected and described before. In the future, this variant will be used to study the process of ligand delivery to modeled membrane, to investigate whether and how fatty acid is delivered to membrane through the helical portal region.

The studies on the mutant V26H/L30H further support the conclusion drawn from the mutant K27C/D74C. The binding of Ni-NTA to the HxxxH motif in the second helix stabilizes the second helix, thus slows down the rate of oleic acid association. It is found that the mutation of V26 and L30 in the second helix leads to a slow conformational exchange in the back portal, as illustrated in ^{15}N-HSQC spectra, suggesting possible relationship between the second helix and the back portal. Such relation requires further validation in the future.

Another mutant V60C/Y70C carries an intra-molecule disulfide bond in the gap region. The disulfide bond makes strands D and E distorted, resulting in the disruption of the interaction between the second α helix and turns C-D and E-F. Oleic acid association becomes slightly slower in the presence of the disulfide bond possibly due to the improper structure. In addition, the mutation Y70C seems to alter the fluorescence property upon ligand binding, suggesting the essential role of Y70 in the interaction with ligand. These observations highlight the significance of the gap D-E in protein stability and ligand binding.

The functionally relevant conformational exchange is not exclusive to hiFABP. Similar observation regarding the ligand accessibility and the transition between the ‘opened’ and the ‘close’ forms of human aromatase has been reported (77). Another study on the translocator protein (TSPO) has illustrated the presence of multiple conformations of the binding site in the absence of ligand and the stabilizing effect of ligand binding (78). This type of protein dynamics is pivotal in various biological activities, such as formation of F-actin, ATPase cycle and ligand entry of β-lactoglobulin (79-81). The

conclusion and the method used in this study may shed light on the relationship between protein dynamics and ligand-protein interactions.

Reference

1. Furuhashi M & Hotamisligil GS (2008) Fatty acid-binding proteins: role in metabolic diseases and potential as drug targets. *Nat Rev Drug Discov* 7(6):489-503.
2. Glatz JFC & Storch J (2001) Unravelling the significance of cellular fatty acid-binding proteins. *Curr Opin Lipidol* 12(3):267-274.
3. Ragona L*, et al.* (2014) The role of dynamics in modulating ligand exchange in intracellular lipid binding proteins. *Biochim Biophys Acta* 1844(7):1268-1278.
4. Hotamisligil GS & Bernlohr DA (2015) Metabolic functions of FABPs--mechanisms and therapeutic implications. *Nat Rev Endocrinol* 11(10):592-605.
5. Ek BA, Cistola DP, Hamilton JA, Kaduce TL, & Spector AA (1997) Fatty acid binding proteins reduce 15-lipoxygenase induced oxygenation of linoleic acid and arachidonic acid. *Biochim Biophys Acta* 1346(1):75-85.
6. Nakamura MT, Yudell BE, & Loor JJ (2014) Regulation of energy metabolism by long-chain fatty acids. *Prog Lipid Res* 53:124-144.
7. Boiteux G*, et al.* (2009) A-FABP, a candidate progression marker of human transitional cell carcinoma of the bladder, is differentially regulated by PPAR in urothelial cancer cells. *Int J Cancer* 124(8):1820-1828.
8. Velkov T (2009) Thermodynamics of Lipophilic Drug Binding to Intestinal Fatty Acid Binding Protein and Permeation across Membranes. *Mol Pharm.* 6(2):557-570.
9. Baier LJ*, et al.* (1995) An amino acid substitution in the human intestinal fatty acid binding protein is associated with increased fatty acid binding, increased fat oxidation, and insulin resistance. *J Clin Invest.* 95(3):1281-1287.
10. Weiss EP*, et al.* (2007) FABP2 Ala54Thr genotype is associated with glucoregulatory function and lipid oxidation after a high-fat meal in sedentary nondiabetic men and women. *Am J Clin Nutr* 85:102-108.
11. Sacchettini JC, Gordonl JI, & Banaszak LJ (1989) Crystal Structure of Rat Intestinal Fatty-Acid-Binding Protein Refinement and Analysis of the Escherichia coli-derived Protein with Bound Palmitate. *J Mol Biol* 208 (2):327-339.
12. Cistola DP, Kim K, Hans Rogl H, & Frieden C (1996) Fatty Acid Interactions with a Helix-less Variant of Intestinal Fatty Acid-Binding Protein. *Biochemistry* 35 (23):7559-7565.
13. Friedman R, Nachliel E, & Gutman M (2005) Molecular Dynamics Simulations of the Adipocyte Lipid Binding Protein Reveal a Novel Entry Site for the Ligand. *Biochemistry* 44(11)(44):4275-4283.
14. Long D, Mu Y, & Yang D (2009) Molecular dynamics simulation of ligand dissociation from liver fatty acid binding protein. *PLoS One* 4(6):e6081.
15. Friedman R, Nachliel E, & Gutman M (2006) Fatty acid binding proteins: same structure but different binding mechanisms? Molecular dynamics simulations of intestinal fatty acid binding protein. *Biophys J* 90(5):1535-1545.

16. Bakowies D & van Gunsteren WF (2002) Simulations of apo and holo-fatty acid binding protein: structure and dynamics of protein, ligand and internal water. *J Mol Biol* 315(4):713-736.
17. Matsuoka D, Sugiyama S, Murata M, & Matsuoka S (2015) Molecular dynamics simulations of heart-type fatty acid binding protein in apo and holo forms, and hydration structure analyses in the binding cavity. *J Phys Chem B* 119(1):114-127.
18. Tsfadia Y*, et al.* (2007) Molecular dynamics simulations of palmitate entry into the hydrophobic pocket of the fatty acid binding protein. *FEBS Lett* 581(6):1243-1247.
19. Mesgarzadeh A, Pfeiffer S, Engelke J, Lassen D, & Rüterjans H (1998) Bound water in apo and holo bovine heart fatty-acid-binding protein determined by heteronuclear NMR spectroscopy. *Eur. J. Biochem* 251:781-786.
20. Hodsdon ME & Cistola DP (1997) Ligand Binding Alters the Backbone Mobility of Intestinal Fatty Acid-Binding Protein as Monitored by 15N NMR Relaxation and 1H Exchange. *Biochemistry* 36(8):2278-2290.
21. Budyak IL, Zhuravleva A, & Gierasch LM (2013) The Role of Aromatic-Aromatic Interactions in Strand-Strand Stabilization of beta-Sheets. *J Mol Biol* 425(18):3522-3535.
22. Rea AM, Thurston V, & Searle MS (2009) Mechanism of ligand-induced folding of a natively unfolded helixless variant of rabbit I-BABP. *Biochemistry* 48(31):7556-7564.
23. Xu Z, Bernlohr DA, & Banaszak LJ (1993) The adipocyte lipid-binding protein at 1.6-A resolution. Crystal structures of the apoprotein and with bound saturated and unsaturated fatty acids. *J Biol Chem* 268(11):7874-7884.
24. Hodsdon ME & Cistola DP (1997) Discrete Backbone Disorder in the Nuclear Magnetic Resonance Structure of Apo Intestinal Fatty Acid-Binding Protein: Implications for the Mechanism of Ligand Entry. *Biochemistry* 36(6):1450-1460.
25. Sjoelund V & Kaltashov IA (2007) Transporter-to-Trap Conversion: a Disulfide Bond Formation in Cellular Retinoic Acid Binding Protein I Mutant Triggered by Retinoic Acid Binding Irreversibly Locks the Ligand Inside the Protein. *Biochemistry* 46(46):13382-13390.
26. Long D & Yang D (2010) Millisecond timescale dynamics of human liver fatty acid binding protein: testing of its relevance to the ligand entry process. *Biophys J* 98(12):3054-3061.
27. Liu Z, Gong Z, Guo DC, Zhang WP, & Tang C (2014) Subtle dynamics of holo glutamine binding protein revealed with a rigid paramagnetic probe. *Biochemistry* 53(9):1403-1409.
28. Pettersen EF*, et al.* (2004) UCSF Chimera--a visualization system for exploratory research and analysis. *J Comput Chem* 25 (13):1605-1612.
29. Mihajlovic M & Lazaridis T (2007) Modeling fatty acid delivery from intestinal fatty acid binding protein to a membrane. *Protein Sci* 16(9):2042-2055.
30. Xu Z, Bernlohr DA, & Banaszak LJ (1992) Crystal Structure of Recombinant Murine Adipocyte Lipid-Binding Protein. *Biochemistry* 31(13):3484-3492.
31. Curto LM, Angelani CR, & Delfino JM (2015) Intervening in the beta-barrel structure of lipid binding proteins: consequences on folding,

ligand-binding and aggregation propensity. *Prostaglandins, Leukotrienes Essent. Fatty Acids* 93:37-43.
32. Yeh S, Ropson IJ, & Rousseau DL (2001) Hierarchical Folding of Intestinal Fatty Acid Binding Protein. *Biochemistry* 40:4205-4210.
33. Chattopadhyay K, Saffarian S, Elson EL, & Frieden C (2002) Measurement of microsecond dynamic motion in the intestinal fatty acid binding protein by using fluorescence correlation spectroscopy. *Proc Natl Acad Sci U S A* 99(22):14171-14176.
34. Chattopadhyay K, Saffarian S, Elson EL, & Frieden C (2005) Measuring unfolding of proteins in the presence of denaturant using fluorescence correlation spectroscopy. *Biophys J* 88(2):1413-1422.
35. Ropson IJ, Yowler BC, Dalessio PM, Banaszak L, & Thompson J (2000) Properties and Crystal Structure of a β-Barrel Folding Mutant. *Biophys J* 78:1551-1560.
36. Franchini GR, Curto LM, Caramelo JJ, & Delfino JM (2009) Dissection of a beta-barrel motif leads to a functional dimer: the case of the intestinal fatty acid binding protein. *Protein Sci* 18(12):2592-2602.
37. Porfido JL*, et al.* (2012) Direct interaction between EgFABP1, a fatty acid binding protein from Echinococcus granulosus, and phospholipid membranes. *PLoS Negl Trop Dis* 6(11):e1893.
38. Co´rsico B, Liou HL, & Storch J (2004) The alpha-Helical Domain of Liver Fatty Acid Binding Protein Is Responsible for the Diffusion-Mediated Transfer of Fatty Acids to Phospholipid Membranes. *Biochemistry* 43 (12):3600-3607.
39. Falomir-Lockhart LJ, Laborde L, Kahn PC, Storch J, & Corsico B (2006) Protein-membrane interaction and fatty acid transfer from intestinal fatty acid-binding protein to membranes. Support for a multistep process. *J Biol Chem* 281(20):13979-13989.
40. de Geronimo E*, et al.* (2014) IFABP portal region insertion during membrane interaction depends on phospholipid composition. *Biochim Biophys Acta* 1841(1):141-150.
41. Herr FM, Aronson J, & Storch J (1996) Role of Portal Region Lysine Residues in Electrostatic Interactions between Heart
Fatty Acid Binding Protein and Phospholipid Membranes. *Biochemistry* 35(4):1296-1303.
42. Lipsitz RS & Tjandra N (2003) 15N chemical shift anisotropy in protein structure refinement and comparison with NH residual dipolar couplings. *J Magn Reson* 164(1):171-176.
43. Salnikov E, Bertani P, Raap J, & Bechinger B (2009) Analysis of the amide (15)N chemical shift tensor of the C(alpha) tetrasubstituted constituent of membrane-active peptaibols, the alpha-aminoisobutyric acid residue, compared to those of di- and tri-substituted proteinogenic amino acid residues. *J Biomol NMR* 45(4):373-387.
44. Zhang F, Lücke C, Baier LJ, Sacchettini JC, & Hamilton JA (2003) Solution Structure of Human Intestinal Fatty Acid Binding Protein with a Naturally-Occurring Single Amino Acid Substitution (A54T) that Is Associated with Altered Lipid Metabolism. *Biochemistry* 42(24):7339-7347.
45. Storch J & McDermott L (2009) Structural and functional analysis of fatty acid-binding proteins. *J Lipid Res* 50 Suppl:S126-131.

46. Cham BE & Knowles BR (1976) A solvent system for delipidationof plasma or serum without protein precipitation. *J Lipid Res* 17 (2):176-181.
47. Kuzmič P (1996) Program DYNAFIT for the Analysis of Enzyme Kinetic Data: Application to HIV Proteinase. *Anal Biochem* 237:260-273.
48. Fan JS, Lim J, Yu B, & Yang D (2011) Measurement of amide hydrogen exchange rates with the use of radiation damping. *J Biomol NMR* 51(1-2):151-162.
49. Richa T & Sivaraman T (2012) CIntX: A Software Tool for Calculating the Intrinsic Exchange Rates of Labile Protons in Proteins. *J. Pharm. Sci. & Res.* 4(6):1852-1858.
50. Dalessio PM & Ropson IJ (1998) pH Dependence of the Folding of Intestinal Fatty Acid Binding Protein. *Arch Biochem Biophys* 359 (2):199-208.
51. Scholtz JM, Grimsley GR, & Pace CN (2009) Chapter 23 Solvent Denaturation of Proteins and Interpretations of the m Value. 466:549-565.
52. Korzhnev DM*, et al.* (2004) Low-populated folding intermediates of Fyn SH3 characterized by relaxation dispersion NMR. *Nature* 430(6999):586-589.
53. Delaglio F*, et al.* (1995) NMRPipe: a multidimensional spectral processing system based on UNIX pipes. *J Biomol NMR* 6(3):277-293.
54. Xu Y, Zheng Y, Fan JS, & Yang D (2006) A new strategy for structure determination of large proteins in solution without deuteration. *Nat Methods* 3(11):931-937.
55. Englander SW & NR K (1983) Hydrogen exchange and structural dynamics of proteins and nucleic acids. *Q Rev Biophys* 16 (4):521-655.
56. Hvidt A & Nielsen S (1966) Hydrogen exchange in proteins. *Adv Protein Chem* 21:287-386.
57. Toke O, Monsey JD, & Cistola DP (2007) Kinetic Mechanism of Ligand Binding in Human Ileal Bile Acid Binding Protein as Determined by Stopped-Flow Fluorescence Analysis. *Biochemistry* 46 (18):5427-5436.
58. Bozza WP, Liang Q, Gong P, & Zhuang Z (2012) Transient kinetic analysis of USP2-catalyzed deubiquitination reveals a conformational rearrangement in the K48-linked diubiquitin substrate. *Biochemistry* 51(50):10075-10086.
59. Horvath G, Kiraly P, Tarkanyi G, & Toke O (2012) Internal motions and exchange processes in human ileal bile acid binding protein as studied by backbone (15)N nuclear magnetic resonance spectroscopy. *Biochemistry* 51(9):1848-1861.
60. Ogura K, Okamura H, Katahira M, Katoh E, & Inagaki F (2012) Conformational dynamics of yeast calmodulin in the Ca(2+)-bound state probed using NMR relaxation dispersion. *FEBS Lett* 586(16):2548-2554.
61. Richieri GV, Low PJ, Ogata RT, & Kleinfeld AM (1999) Binding Kinetics of Engineered Mutants Provide Insight about the Pathway for Entering and Exiting the Intestinal Fatty Acid Binding Protein. *Biochemistry* 38 (18):5888-5895.

62. Richieri GV, Low PJ, Ogata RT, & Kleinfeld AM (1998) Thermodynamics of Fatty Acid Binding to Engineered Mutants of the Adipocyte and Intestinal Fatty Acid-binding Proteins. *J Biol Chem* 273(13):7397-7405.
63. Korzhnev DM, Kloiber K, & Kay LE (2004) Multiple-Quantum Relaxation Dispersion NMR Spectroscopy Probing Millisecond Time-Scale Dynamics in Proteins: Theory and Application. *J. Am. Chem. Soc.* 126(23):7320-7329.
64. Otten R, Villali J, Kern D, & Mulder FAA (2010) Probing Microsecond Time Scale Dynamics in Proteins by Methyl 1H Carr-Purcell-Meiboom-Gill Relaxation Dispersion NMR Measurements. Application to Activation of the Signaling Protein NtrCr. *J. Am. Chem. Soc* 132:17004-17014.
65. Franchini GR, Storch J, & Corsico B (2008) The integrity of the alpha-helical domain of intestinal fatty acid binding protein is essential for the collision-mediated transfer of fatty acids to phospholipid membranes. *Biochim Biophys Acta* 1781(4):192-199.
66. Sawicki LR*, et al.* (2014) Characterization of fatty acid binding and transfer from Delta98Delta, a functional all-beta abridged form of IFABP. *Biochim Biophys Acta* 1841(12):1733-1740.
67. Dyszy F, Pinto APA, Araújo APU, & Costa-Filho AJ (2013) Probing the Interaction of Brain Fatty Acid Binding Protein (B-FABP) with Model Membranes. *PLoS ONE* 8(3):e60198.
68. Arnold FH & Haymore BL (1991) Engineered Metal-Binding Proteins: Purification to Protein Folding. *Science* 252:1796-1797.
69. Levin LB, Nachliel E, Gutman M, & Tsfadia Y (2009) Molecular dynamics study of the interaction between fatty acid binding proteins with palmitate mini-micelles. *Mol Cell Biochem* 326(1-2):29-33.
70. Chakrabartty A, Kortemme T, & Baldwin RL (1994) Helix propensities of the amino acids measured in alanine-based peptides without helix-stabilizing side-chain interactions. *Protein Sci* 3:843-852.
71. Zhang F, Lücke C, Baier LJ, Sacchettini JC, & Hamilton JA (1997) Solution structure of human intestinal fatty acid binding protein: Implications for ligand entry and exit. *J Biomol NMR* 9(1997):213-228.
72. Ory JJ & Banaszak LJ (1999) Studies of the Ligand Binding Reaction of Adipocyte Lipid Binding Protein Using the Fluorescent Probe 1,8 Anilinonaphthalene-8-Sulfonate. *Biophys J* 77:1107-1116.
73. Kirk WR, Kurian E, & Prendergast FG (1996) Characterization of the sources of protein-ligand affinity: 1-sulfonato-8-(1')anilinonaphthalene binding to intestinal fatty acid binding protein. *Biophys J* 70(1):69-83.
74. Hodsdon ME & Frieden C (2001) Intestinal Fatty Acid Binding Protein: The Folding Mechanism As Determined by NMR Studies. *Biochemistry* 40:732-742.
75. Sanson B*, et al.* (2014) Crystallographic study of FABP5 as an intracellular endocannabinoid transporter. *Acta Crystallogr D Biol Crystallogr* 70(Pt 2):290-298.
76. Ghisaidoobe AB & Chung SJ (2014) Intrinsic tryptophan fluorescence in the detection and analysis of proteins: a focus on Forster resonance energy transfer techniques. *Int J Mol Sci* 15(12):22518-22538.
77. Di Nardo G*, et al.* (2013) Dynamics and flexibility of human aromatase probed by FTIR and time resolved fluorescence spectroscopy. *PLoS One* 8(12):e82118.

78. Jaremko L, Jaremko M, Giller K, Becker S, & Zweckstetter M (2015) Conformational Flexibility in the Transmembrane Protein TSPO. *Chemistry* 21(46):16555-16563.
79. Shvetsov A*, et al.* (2006) Conformational Dynamics of Loop 262-274 in G- and F-actin. *Biochemistry* 45:6541-6549.
80. Bello M & Garcia-Hernandez E (2014) Ligand entry into the calyx of beta-lactoglobulin. *Biopolymers* 101(7):744-757.
81. Muretta JM*, et al.* (2013) Loop L5 assumes three distinct orientations during the ATPase cycle of the mitotic kinesin Eg5: a transient and time-resolved fluorescence study. *J Biol Chem* 288(48):34839-34849.